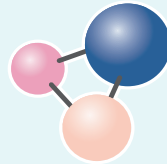


ИЗВЕСТИЯ ВУЗОВ



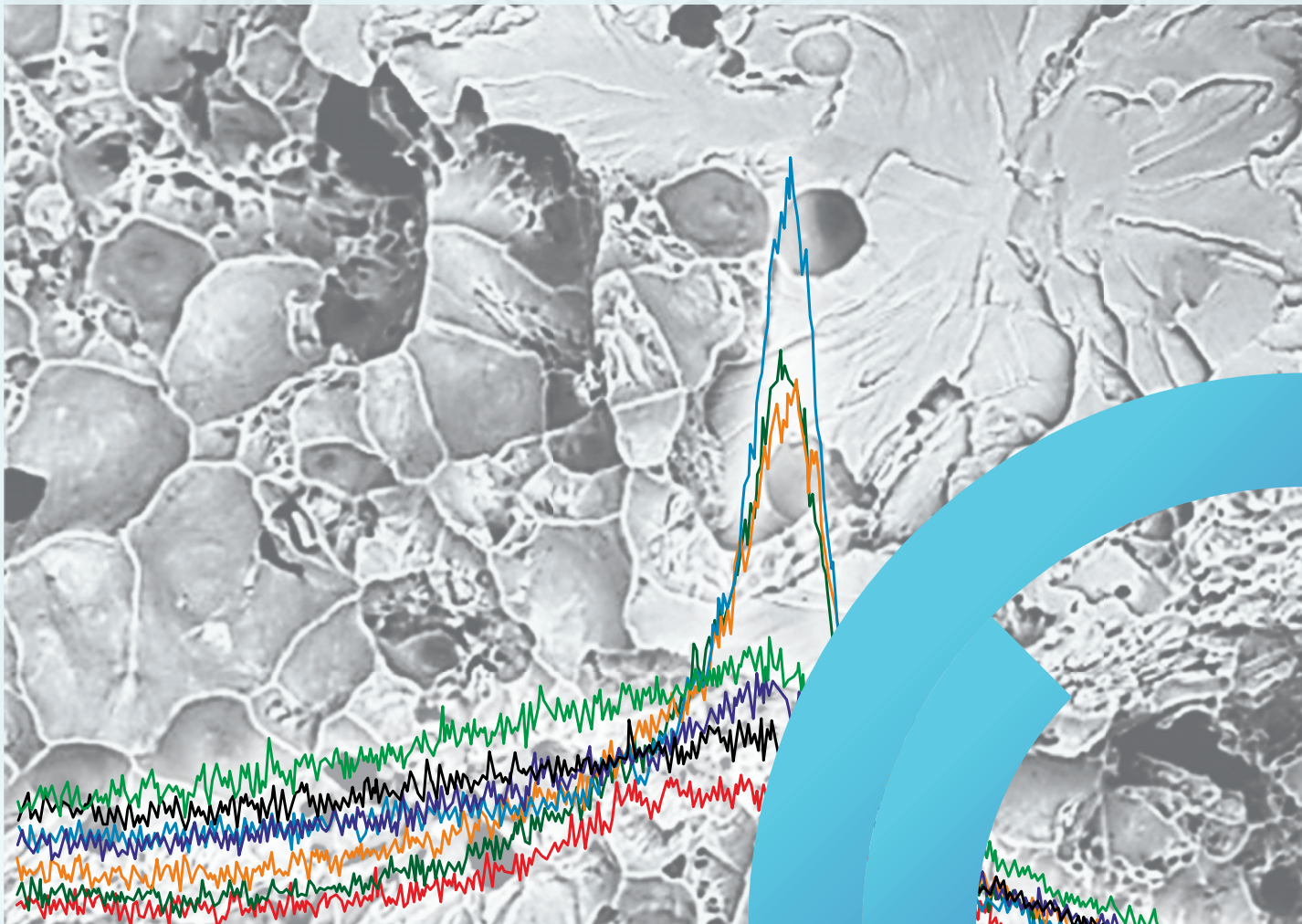
# ПОРОШКОВАЯ МЕТАЛЛУРГИЯ И ФУНКЦИОНАЛЬНЫЕ ПОКРЫТИЯ

**POWDER METALLURGY  
AND FUNCTIONAL COATINGS**

**2025**

Том 19 № 3  
Vol. 19 No. 3

[powder.misis.ru](http://powder.misis.ru)



ISSN 1997-308X  
eISSN 2412-8767

# POWDER METALLURGY AND FUNCTIONAL COATINGS

Scientific and Technical Journal  
Founded in 2007  
Six issues per year

2025

Том 19 № 3  
Vol. 19 No. 3

# ИЗВЕСТИЯ ВУЗОВ ПОРОШКОВАЯ МЕТАЛЛУРГИЯ И ФУНКЦИОНАЛЬНЫЕ ПОКРЫТИЯ

Научно-технический журнал  
Основан в 2007 г.  
Выходит 6 раз в год

# POWDER METALLURGY AND FUNCTIONAL COATINGS

SCIENTIFIC AND TECHNICAL JOURNAL  
FOUNDED IN 2007  
SIX ISSUES PER YEAR

<http://powder.misis.ru>

ISSN 1997-308X  
eISSN 2412-8767



Founder: National University of Science  
and Technology "MISIS"

Address: 1 Bld, 4 Leninskiy Prosp., Moscow 119049, Russian Federation  
<http://www.misis.ru>

Editor-in-Chief

Evgeny A. Levashov

Dr. Sci. (Eng.), Corr. Mem. of the RAS, Prof., NUST MISIS, Moscow, Russian Federation

Journal is included into the List of peer-reviewed scientific publications recommended by the Highest Attestation Commission of the Ministry of Education and Science of the Russian Federation for publishing the results of doctoral and candidate dissertations. Abstracting/Indexing: Scopus, Russian Science Citation Index (RSCI), Ulrich's Periodicals Directory, VINITI Database (Abstract Journal).

## Editorial Board

**M. I. Alymov** – Dr. Sci. (Eng.), Corresponding Member of the RAS, Merzhanov Institute of Structural Macrokinetics and Materials Sciences of the RAS, Chernogolovka, Russia  
**A. P. Amosov** – Prof., Dr. Sci. (Phys.-Math.), Samara State Technical University, Samara, Russia  
**I. V. Blinkov** – Prof., Dr. Sci. (Eng.), NUST MISIS, Moscow, Russia  
**M. V. Chukin** – Prof., Dr. Sci. (Eng.), Magnitogorsk State Technical University, Magnitogorsk, Russia  
**H. Danninger** – Prof., Dr. Sci., Vienna University of Technology, Vienna, Austria  
**B. Derin** – Assoc. Prof., Dr. Sci. (Phil.), Istanbul Technical University, Maslak, Istanbul, Turkey  
**V. Yu. Dorofeyev** – Prof., Dr. Sci. (Eng.), South-Russian State Polytechnical University (NPI), Novocherkassk, Russia  
**Yu. Estrin** – Prof., Dr. Sci. (Nat.), Monash University, Clayton, Australia  
**A. Ph. Ilyushchanka** – Prof., Dr. Sci. (Eng.), Acad. of the NAS of Belarus, State Research and Production Powder Metallurgy Association, Minsk, Belarus  
**Yu. R. Kolobov** – Prof., Dr. Sci. (Phys.-Math.), Federal Research Center of Problems of Chemical Physics and Medicinal Chemistry of the RAS, Chernogolovka, Russia  
**V. S. Komlev** – Prof., Dr. Sci. (Eng.), Corresponding Member of the RAS, Institute of Metallurgy of the RAS, Moscow, Russia  
**I. Konyashin** – Prof., Dr. Sci. (Econ.), Element Six GmbH, Burghaun, Germany  
**Yu. M. Korolyov** – Prof., Dr. Sci. (Eng.), Scientific and Technical Association "Powder Metallurgy", Moscow, Russia  
**D. Yu. Kovalev** – Dr. Sci. (Phys.-Math.), Merzhanov Institute of Structural Macrokinetics and Materials Sciences of the RAS, Chernogolovka, Russia  
**S. A. Kulinich** – Assoc. Prof., PhD (Chem.), Tokai University, Hiratsuka, Kanagawa, Japan  
**S. V. Kuzmin** – Prof., Dr. Sci. (Eng.), Corresponding Member of the RAS, Volgograd State Technical University, Volgograd, Russia  
**V. P. Kuznetsov** – Prof., Dr. Sci. (Eng.), Ural Federal University, Ekaterinburg, Russia  
**Yu. V. Levinsky** – Prof., Dr. Sci. (Eng.) Merzhanov Institute of Structural Macrokinetics and Materials Sciences of the RAS, Chernogolovka, Russia  
**A. E. Ligachyov** – Prof., Dr. Sci. (Phys.-Math.), Prokhorov General Physics Institute of the RAS, Moscow, Russia  
**V. Yu. Lopatin** – Cand. Sci., NUST MISIS, Moscow, Russia  
**A. A. Lozovan** – Prof., Dr. Sci. (Eng.), Moscow Aviation Institute (NRU), Moscow, Russia

**V. I. Lysak** – Prof., Dr. Sci. (Eng.), Acad. of the RAS, Volgograd State Technical University, Volgograd, Russia  
**A. V. Makarov** – Dr. Sci. (Eng.), Acad. of the RAS, M.N. Mikheev Institute of Metal Physics of the Ural Branch of the RAS, Ural Federal University, Ekaterinburg, Russia  
**L. L. Mishnaevsky** – Dr. Habil. (Eng.), Technical University of Denmark, Roskilde, Denmark  
**A. S. Mukasyan** – Prof., Dr. Sci. (Phys.-Math.), University of Notre Dame, Notre Dame, USA  
**S. A. Oglezneva** – Prof., Dr. Sci. (Eng.), Perm National Research Polytechnical University, Perm, Russia  
**R. Orrù** – Prof., Dr. Sci. (Eng.), University of Cagliari, Cagliari, Italy  
**I. B. Pantelev** – Prof., Dr. Sci. (Eng.), St. Petersburg State Technological Institute (Technical University), St. Petersburg, Russia  
**F. Peizhong** – Prof., Dr. Sci., China University of Mining and Technology, Xuzhou, P.R. China  
**C. Pengwan** – Prof., Dr. Sci., Beijing Institute of Technology, Beijing, P.R. China  
**M. I. Petrzhik** – Dr. Sci. (Eng.), NUST MISIS, Moscow, Russia  
**Yu. S. Pogozhev** – Assoc. Prof., Cand. Sci. (Eng.), NUST MISIS, Moscow, Russia  
**V. V. Polyakov** – Prof., Dr. Sci. (Phys.-Math.), Altai State University, Barnaul, Russia  
**A. A. Popovich** – Prof., Dr. Sci. (Eng.), Corresp. Member of the RAS, St. Petersburg State Polytechnical University (National Research University), St. Petersburg, Russia  
**S. E. Porozova** – Dr. Sci. (Eng.), Perm National Research Polytechnical University, Perm, Russia  
**A. A. Rempel** – Prof., Dr. Sci. (Phys.-Math.), Acad. of the RAS, Institute of Metallurgy of the Ural Branch of the RAS, Ekaterinburg, Russia  
**F. Rustichelli** – Prof., Dr. Sci. (Phys.), University of Marches, Ancona, Italy  
**S. D. Shlyapin** – Prof., Dr. Sci. (Eng.), Moscow Aviation Institute (NRU), Moscow, Russia  
**D. V. Shtansky** – Prof., Dr. Sci. (Phys.-Math.), NUST MISIS, Moscow, Russia  
**A. N. Timofeev** – Dr. Sci. (Eng.), JSC "Komposite", Korolev, Russia  
**P. A. Vityaz'** – Prof., Dr. Sci. (Eng.), Acad. of the NAS of Belarus, Minsk, Belarus  
**A. A. Zaitsev** – Assoc. Prof., Cand. Sci. (Eng.), NUST MISIS, Moscow, Russia  
**Zheng YongTing** – Prof., Dr. Sci., Harbin Institute of Technology, Harbin, P.R. China  
**F. Zhengyi** – Prof., Dr. Sci., Wuhan University of Technology, Wuhan, P.R. China

## Editorial Staff

Address: NUST MISIS,  
1 Bld, 4 Leninskiy Prosp., Moscow 119049, Russian Federation

Phone: +7 (495) 638-45-35. E-mail: [izv.vuz@misis.ru](mailto:izv.vuz@misis.ru)

Certificate of registration No. FS77-27955 (12.04.2007)

Re-registration PI No. FS77-79230 (25.09.2020)



PM & FC © NUST MISIS, Moscow, 2025



Articles are available under Creative Commons  
Attribution Non-Commercial No Derivatives

Leading Editor: A.A. Kudinova

Executive Editor: O.V. Sosnina

Layout Designer: V.V. Rasenets

Signed print 21.06.2025. Format 60x90 1/8  
Offset paper No. 1. Digital printing. Quires 9.25

Order 22437. Free price

Printed in the printing house of the MISIS Publish House  
1 Bld, 4 Leninskiy Prosp., Moscow 119049, Russian Federation  
Phone/fax: +7 (499) 236-76-17

# ИЗВЕСТИЯ ВУЗОВ ПОРОШКОВАЯ МЕТАЛЛУРГИЯ И ФУНКЦИОНАЛЬНЫЕ ПОКРЫТИЯ

ISSN 1997-308X  
eISSN 2412-8767



ФГАОУ ВО Национальный исследовательский  
технологический университет «МИСИС»

Адрес: 119049, Москва, Ленинский пр-т, 4, стр. 1

<https://www.misis.ru>

**Главный редактор**

**Евгений Александрович Левашов**

д.т.н., чл.-корр. РАН, профессор, НИТУ МИСИС, г. Москва

**НАУЧНО-ТЕХНИЧЕСКИЙ ЖУРНАЛ**

ОСНОВАН В 2007 Г.

ВЫХОДИТ 6 РАЗ В ГОД

<http://powder.misis.ru>

Журнал включен в Перечень рецензируемых научных изданий, рекомендованных ВАК Минобрнауки РФ  
для публикации результатов диссертаций на соискание ученых степеней.

Журнал включен в базы данных: Scopus, Russian Science Citation Index (RSCI), Ulrich's Periodicals Directory, РИНЦ, БД/РЖ ВИНТИ.

## Редакционная коллегия

- М. И. Алымов – д.т.н., чл.-корр. РАН, проф., ИСМАН, г. Черноголовка  
А. П. Амосов – д.ф.-м.н., проф., СамГТУ, г. Самара  
И. В. Блинков – д.т.н., проф., НИТУ МИСИС, г. Москва  
П. А. Витязь – д.т.н., акад. НАНБ, проф., НАН Беларуси, г. Минск  
В. Ю. Дорофеев – д.т.н., проф., ЮРГПУ (НПИ), г. Новочеркасск  
А. А. Зайцев – к.т.н., доц., НИТУ МИСИС, г. Москва  
А. Ф. Ильющенко – д.т.н., акад. НАН Беларуси, проф.,  
ГНПО ПМ НАН Беларуси, г. Минск  
Д. Ю. Ковалев – д.ф.-м.н., ИСМАН, г. Черноголовка  
Ю. Р. Колобов – д.ф.-м.н., проф., ФИЦ ПХФ и МХ РАН, г. Черноголовка  
В. С. Комлев – д.т.н., чл.-корр. РАН, проф., ИМЕТ РАН, г. Москва  
Ю. М. Королев – д.т.н., проф., НТА «Порошковая металлургия»,  
г. Москва  
В. П. Кузнецов – д.т.н., проф., УрФУ, г. Екатеринбург  
С. В. Кузьмин – д.т.н., чл.-корр. РАН, проф., ВолГТУ, г. Волгоград  
Ю. В. Левинский – д.т.н., проф., ИСМАН, г. Черноголовка  
А. Е. Лигачев – д.ф.-м.н., проф., ИОФ РАН, г. Москва  
А. А. Лозован – д.т.н., проф., МАИ (НИУ), г. Москва  
В. Ю. Лопатин – к.т.н., доц., НИТУ МИСИС, г. Москва  
В. И. Лысак – д.т.н., акад. РАН, проф., ВолГТУ, г. Волгоград  
А. В. Макаров – д.т.н., акад. РАН, ИФМ УрО РАН, УрФУ,  
г. Екатеринбург  
С. А. Оглезнева – д.т.н., проф., ПНИПУ, г. Пермь  
И. Б. Пантелеев – д.т.н., проф., СПбГТИ (ТУ), г. Санкт-Петербург  
М. И. Петржик – д.т.н., проф., НИТУ МИСИС, г. Москва  
Ю. С. Погожев – к.т.н., доц., НИТУ МИСИС, г. Москва  
В. В. Поляков – д.ф.-м.н., проф., АлтГУ, г. Барнаул  
А. А. Попович – д.т.н., чл.-корр. РАЕН, проф., СПбГПУ,  
г. Санкт-Петербург  
С. Е. Порозова – д.т.н., проф., ПНИПУ, г. Пермь  
А. А. Ремпель – д.ф.-м.н., акад. РАН, проф., ИМЕТ УрО РАН,  
г. Екатеринбург  
А. Н. Тимофеев – д.т.н., АО «Композит», г. Королев  
М. В. Чукин – д.т.н., проф., МГТУ, г. Магнитогорск  
С. Д. Шляпин – д.т.н., проф., МАИ (НИУ), г. Москва  
Д. В. Штанский – д.ф.-м.н., проф., НИТУ МИСИС, г. Москва  
H. Danningер – Dr. Sci., Prof., Vienna University of Technology,  
Vienna, Austria  
B. Derin – Dr. Sci. (Phil.), Assoc. Prof., Istanbul Technical University,  
Maslak, Istanbul, Turkey  
Yu. Estrin – Dr. Sci. (Nat.), Prof., Monash University, Clayton, Australia  
I. Konyashin – Dr. Sci. (Econ.), Prof., Element Six GmbH, Burghaun,  
Germany  
S. A. Kulinich – PhD (Chem.), Associate Prof., Tokai University, Hiratsuka,  
Kanagawa, Japan  
L. L. Mishnaevsky – Dr. Habil. (Eng.), Technical University of Denmark,  
Roskilde, Denmark  
A. S. Mukasyan – Dr. Sci. (Phys.-Math.), Prof., University of Notre Dame,  
Notre Dame, USA  
R. Orrù – Dr. Sci. (Eng.), Prof., University of Cagliari, Cagliari, Italy  
F. Peizhong – Dr. Sci., Prof., China University of Mining and Technology,  
Xuzhou, P.R. China  
C. Pengwan – Dr. Sci., Prof., Beijing Institute of Technology,  
Beijing, P.R. China  
F. Rustichelli – Dr. Sci. (Phys.), Prof., University of Marches, Ancona, Italy  
Zheng YongTing – Dr. Sci., Prof., Harbin Institute of Technology, Harbin,  
P.R. China  
F. Zhengyi – Dr. Sci., Prof., Wuhan University of Technology, Wuhan,  
P.R. China

## Редакция журнала

Адрес: 119049, Москва,  
Ленинский пр-т, 4, стр. 1. НИТУ МИСИС

Тел.: +7 (495) 638-45-35. Эл. почта: [izv.vuz@misis.ru](mailto:izv.vuz@misis.ru)

Свидетельство о регистрации № ФС77-27955 от 12.04.2007 г.  
Перерегистрация 25.09.2020 г. ПИ № ФС77-79230



© НИТУ МИСИС, Москва, 2025



Статьи доступны под лицензией Creative Commons  
Attribution Non-Commercial No Derivatives

Ведущий редактор: А.А. Кудинова  
Выпускающий редактор: О.В. Соснина  
Дизайн и верстка: В.В. Расенец

Подписано в печать 21.06.2025. Формат 60×90 1/8  
Бум. офсетная № 1. Печать цифровая. Усл. печ. л. 9,25  
Заказ 22437. Цена свободная  
Отпечатано в типографии Издательского Дома МИСИС  
119049, г. Москва, Ленинский пр-т, 4, стр. 1  
Тел./факс: +7 (499) 236-76-17

Contents



Содержание

Production Processes  
and Properties of Powders

**Vassilyeva Yu.Z., Povalyaev P.V.,  
Kuznetsova A.A., Pak A.Ya.**  
Obtaining ceramics from boron carbide  
with chromium-based additives ( $\text{Cr}_3\text{C}_2$ ,  $\text{CrB}_2$ ) ..... 5

Theory and Processes of Formation  
and Sintering of Powder Materials

**Parkhomenko A.V., Amosov A.P., Pastukhov A.M.**  
Development of a polyoxymethylene-based feedstock  
for metal injection molding using 09Cr16Ni4Nb  
stainless steel powder ..... 15

Self-Propagating  
High-Temperature Synthesis

**Uvarova I.A., Amosov A.P.,  
Titova Yu.V., Novikov V.A.**  
Self-propagating high-temperature synthesis  
of a highly dispersed  $\text{Si}_3\text{N}_4$ -SiC ceramic powders  
composition using sodium azide and  
polytetrafluoroethylene ..... 25

Refractory, Ceramic,  
and Composite Materials

**Kuzmenko E.D., Matrenin S.V., Nassyrbayev A.R.**  
Effect of magnesium oxide on the microstructure  
and mechanical properties of yttria-stabilized  
zirconia-based ceramics ..... 39

Nanostructured Materials  
and Functional Coatings

**Zamulaeva E.I., Loginov P.A.,  
Kiryukhantsev-Korneev Ph.V., Shvindina N.V.,  
Petrzhik M.I., Levashov E.A.**  
Structure and properties of two-layer coatings  
in the  $\text{HfSi}_2$ - $\text{HfB}_2$ - $\text{MoSi}_2$  system produced  
by electrospark deposition and magnetron sputtering ..... 48

**Kiryukhantsev-Korneev Ph.V., Chertova A.D.,  
Pogozhev Yu.S., Levashov E.A.**  
Structure and properties of anti-friction  
Ti-Cr-Ni-Cu-Sn-P-C-N coatings  
deposited by magnetron sputtering of composite  
SHS targets ..... 60

Процессы получения  
и свойства порошков

**Васильева Ю.З., Поваляев П.В.,  
Кузнецова А.А., Пак А.Я.**  
Получение керамики из карбида бора  
с добавками на основе хрома ( $\text{Cr}_3\text{C}_2$ ,  $\text{CrB}_2$ ) ..... 5

Теория и процессы формования  
и спекания порошковых материалов

**Пархоменко А.В., Амосов А.П., Пастухов А.М.**  
Разработка гранулята на полиформальдегидном  
связующем на основе порошка нержавеющей стали  
09X16H4B для МИМ-технологии ..... 15

Самораспространяющийся  
высокотемпературный синтез

**Уварова И.А., Амосов А.П.,  
Титова Ю.В., Новиков В.А.**  
Самораспространяющийся высокотемпературный  
синтез высокодисперсной композиции керамических  
порошков  $\text{Si}_3\text{N}_4$ -SiC с применением азиды натрия  
и политетрафторэтилена ..... 25

Тугоплавкие, керамические  
и композиционные материалы

**Кузьменко Е.Д., Матренин С.В., Насырбаев А.Р.**  
Влияние оксида магния на микроструктуру  
и механические свойства керамики на основе  
диоксида циркония, стабилизированного  
оксидом иттрия ..... 39

Наноструктурированные материалы  
и функциональные покрытия

**Замулаева Е.И., Логинов П.А.,  
Кирюханцев-Корнеев Ф.В., Швындина Н.В.,  
Петржик М.И., Левашов Е.А.**  
Структура и свойства двухслойных покрытий в системе  
 $\text{HfSi}_2$ - $\text{HfB}_2$ - $\text{MoSi}_2$ , полученных методами  
электроискрового и магнетронного напыления ..... 48

**Кирюханцев-Корнеев Ф.В., Чертова А.Д.,  
Погожев Ю.С., Левашов Е.А.**  
Структура и свойства антифрикционных  
покрытий в системе Ti-Cr-Ni-Cu-Sn-P-C-N,  
полученных методом магнетронного распыления  
композиционных СВС-мишеней ..... 60



UDC 621.762

<https://doi.org/10.17073/1997-308X-2025-3-5-14>Research article  
Научная статья

## Obtaining ceramics from boron carbide with chromium-based additives ( $\text{Cr}_3\text{C}_2$ , $\text{CrB}_2$ )

Yu. Z. Vassilyeva , P. V. Povalyaev, A. A. Kuznetsova, A. Ya. PakNational Research Tomsk Polytechnic University  
30 Lenin Prosp., Tomsk 634050, Russia yzv1@tpu.ru

**Abstract.** This study presents the results of spark plasma sintering of powders within the boron–carbon–chromium system, focusing on boron carbide ( $\text{B}_4\text{C}$ ), chromium carbide ( $\text{Cr}_3\text{C}_2$ ), and chromium diboride ( $\text{CrB}_2$ ). The powders were synthesized using the original vacuum-free direct current arc reactor, where the starting powder mixture was exposed to an arc discharge for 60 s under a direct current of 200 A. Bulk samples based on  $\text{B}_4\text{C}$  and  $\text{CrB}_2$  were sintered under identical conditions, with a temperature of 1800 °C and a pressure of 60 MPa, while the sintering of  $\text{Cr}_3\text{C}_2$ -based ceramics was conducted at 1300 °C and 30 MPa. In some cases, sintering additives – 25 wt. %  $\text{Cr}_3\text{C}_2$  and 20 wt. %  $\text{CrB}_2$  – were introduced during the sintering of  $\text{B}_4\text{C}$ -based bulk samples. The phase composition of the sintered samples was analyzed using X-ray diffraction (XRD), while the microstructure and elemental composition were examined via scanning electron microscopy (SEM). The hardness of the sintered ceramics was measured using a Vickers indenter under a load of 1 kg, revealing hardness values of  $22.7 \pm 1.8$  GPa for  $\text{B}_4\text{C}$ ,  $12.6 \pm 0.3$  GPa for  $\text{CrB}_2$ , and  $11.4 \pm 0.1$  GPa for  $\text{Cr}_3\text{C}_2$ . The introduction of 25 wt. %  $\text{Cr}_3\text{C}_2$  as a sintering additive in  $\text{B}_4\text{C}$ -based ceramics reduced the hardness to  $17.7 \pm 5.6$  GPa; however, it significantly improved the fracture toughness, increasing it from  $2.5 \pm 0.2$  to  $3.3 \pm 0.3$   $\text{MPa} \cdot \text{m}^{1/2}$ . Conversely, the addition of 20 wt. %  $\text{CrB}_2$  during  $\text{B}_4\text{C}$  sintering led to an increase in the bulk sample's hardness from  $22.7 \pm 1.8$  GPa to  $26.8 \pm 1.3$  GPa.

**Keywords:** composite ceramics,  $\text{B}_4\text{C}$ ,  $\text{CrB}_2$ ,  $\text{Cr}_3\text{C}_2$ , vacuum-free arc discharge method, spark plasma synthesis, hardness

**Acknowledgements:** This work was supported by the Ministry of Science and Higher Education of the Russian Federation (Project No. FSWW-2023-0011).

**For citation:** Vassilyeva Yu.Z., Povalyaev P.V., Kuznetsova A.A., Pak A.Ya. Obtaining ceramics from boron carbide with chromium-based additives ( $\text{Cr}_3\text{C}_2$ ,  $\text{CrB}_2$ ). *Powder Metallurgy and Functional Coatings*. 2025;19(3):5–14.  
<https://doi.org/10.17073/1997-308X-2025-3-5-14>

## Получение керамики из карбида бора с добавками на основе хрома ( $\text{Cr}_3\text{C}_2$ , $\text{CrB}_2$ )

Ю. З. Васильева , П. В. Поваляев, А. А. Кузнецова, А. Я. ПакНациональный исследовательский Томский политехнический университет  
Россия, 634050, г. Томск, пр-т Ленина, 30 yzv1@tpu.ru

**Аннотация.** Представлены результаты исследования процесса искрового плазменного спекания порошков системы «бор–углерод–хром», а именно карбидов бора и хрома, а также диборида хрома. Синтез порошков ( $\text{B}_4\text{C}$ ,  $\text{CrB}_2$  и  $\text{Cr}_3\text{C}_2$ ) для спекания осуществлялся с использованием оригинального безвакуумного электродугового реактора постоянного тока при длительности обработки исходной смеси порошков воздействием дугового разряда 60 с и силе тока, установленной на источнике постоянного тока, 200 А. Спекание объемных образцов на основе карбида бора ( $\text{B}_4\text{C}$ ) и диборида хрома ( $\text{CrB}_2$ ) проводилось при одинаковых параметрах – температуре  $t = 1800$  °C и давлении  $P = 60$  МПа, а спекание керамического

образца на основе карбида хрома ( $\text{Cr}_3\text{C}_2$ ) – при  $t = 1300\text{ }^\circ\text{C}$  и  $P = 30\text{ МПа}$ . Также в процессе спекания объемных образцов на основе карбида бора в ряде случаев применялись спекающие добавки – 25 мас. %  $\text{Cr}_3\text{C}_2$  и 20 мас. %  $\text{CrB}_2$ . Посредством рентгеновской дифрактометрии был изучен фазовый состав спеченных образцов. Микроструктуру и элементный состав полученных образцов определяли с помощью растровой электронной микроскопии. Твердость спеченной керамики оценивали с использованием твердомера с наконечником Виккерса при малой нагрузке в 1 кг – установлено, что твердость образца  $\text{B}_4\text{C}$  составляет  $22,7 \pm 1,8\text{ ГПа}$ ,  $\text{CrB}_2$  –  $12,6 \pm 0,3\text{ ГПа}$ ,  $\text{Cr}_3\text{C}_2$  –  $11,4 \pm 0,1\text{ ГПа}$ . Введение спекающей добавки в виде 25 мас. %  $\text{Cr}_3\text{C}_2$  при получении керамики на основе  $\text{B}_4\text{C}$  привело к снижению твердости до  $17,7 \pm 5,6\text{ ГПа}$ , однако наблюдалось повышение трещиностойкости полученного образца с  $2,5 \pm 0,2$  до  $3,3 \pm 0,3\text{ МПа}\cdot\text{м}^{1/2}$ . Добавка 20 мас. %  $\text{CrB}_2$  при спекании  $\text{B}_4\text{C}$  позволила увеличить твердость объемного образца с  $22,7 \pm 1,8$  до  $26,8 \pm 1,3\text{ ГПа}$ .

**Ключевые слова:** композиционная керамика,  $\text{B}_4\text{C}$ ,  $\text{CrB}_2$ ,  $\text{Cr}_3\text{C}_2$ , безвакуумный электродуговой метод, искровое плазменное спекание, твердость

**Благодарности:** Работа выполнена при финансовой поддержке Министерства науки и высшего образования Российской Федерации (проект № FSWW-2023-0011).

**Для цитирования:** Васильева Ю.З., Поваляев П.В., Кузнецова А.А., Пак А.Я. Получение керамики из карбида бора с добавками на основе хрома ( $\text{Cr}_3\text{C}_2$ ,  $\text{CrB}_2$ ). *Известия вузов. Порошковая металлургия и функциональные покрытия*. 2025;19(3):5–14. <https://doi.org/10.17073/1997-308X-2025-3-5-14>

## Introduction

Boron carbide ( $\text{B}_4\text{C}$ ) is one of the most promising superhard materials in its class, widely recognized for its unique properties, including a high melting point ( $\sim 2450\text{ }^\circ\text{C}$  according to the boron carbide phase diagram) and excellent thermal stability [1].  $\text{B}_4\text{C}$ -based ceramics exhibit outstanding hardness ( $\sim 29\text{ GPa}$ ) combined with a relatively low density ( $2.52\text{ g/cm}^3$ ) [2]. These properties make boron carbide highly suitable for a range of applications, such as the production of refractory materials, abrasive products, neutron radiation absorbers [1], coatings for cutting tools [3], and ballistic protection systems [4].

The performance of  $\text{B}_4\text{C}$ -based ceramics can be enhanced through the introduction of sintering additives. Numerous studies have explored how various additives influence the mechanical properties of boron carbide ceramics. Research findings [5–8] indicate that the addition of carbides and borides of silicon and chromium can significantly improve these properties. For example, study [6] demonstrated that adding  $\text{Cr}_3\text{C}_2$  as a sintering additive to  $\text{B}_4\text{C}$  significantly increases the densification while achieving a high relative density (up to 95 %) and flexural strength (up to 440 MPa). Previously published studies [5; 9] have shown that the introduction of chromium diboride as a sintering additive can enhance the mechanical properties of boron carbide ceramics. In [5], the addition of 20 mol. %  $\text{CrB}_2$  as a sintering additive increased the fracture toughness of the sintered ceramic to  $3.5\text{ МПа}\cdot\text{м}^{1/2}$ , with a flexural strength of 630 MPa. Similarly, study [9] reported that a  $\text{B}_4\text{C}$ –10mol.% $\text{CrB}_2$  composite exhibited a fracture toughness of  $5.25\text{ МПа}\cdot\text{м}^{1/2}$  (compared to  $4.33\text{ МПа}\cdot\text{м}^{1/2}$  without additives) and a microhardness of 37.1 GPa (compared to 35.5 GPa without additives).

The primary methods for producing boron carbide include carbothermal reduction of boron oxide [2; 10], self-propagating high-temperature synthesis [11; 12], mechanical activation followed by heat treatment [13], among others. Among advanced synthesis methods, the arc discharge technique stands out due to its ability to achieve extremely high temperatures over a wide range, with rapid heating rates [14]. In the authors' previous studies, the feasibility of synthesizing boron carbide using a vacuum-free arc discharge method with a horizontal discharge circuit was demonstrated. This approach eliminates the need for creating an inert atmosphere in the reaction zone or ensuring airtight conditions in the reaction chamber, as the vacuum-free arc reactor can operate in ambient air. This significantly simplifies the reactor design and reduces the overall processing cycle time [15].

The objective of this study is to investigate the synthesis of boron carbide, chromium diboride, and chromium carbide powders using the vacuum-free arc discharge method, followed by the sintering of the obtained powders. A key focus of this work is the evaluation of the mechanical properties of the resulting ceramic samples and the assessment of how sintering additives, specifically  $\text{CrB}_2$  and  $\text{Cr}_3\text{C}_2$  compounds, influence the mechanical performance of  $\text{B}_4\text{C}$ -based ceramic composites.

## Research materials and methods

The synthesis of powders ( $\text{B}_4\text{C}$ ,  $\text{Cr}_3\text{C}_2$ ,  $\text{CrB}_2$ ) for sintering was performed using a vacuum-free arc discharge method in a custom-designed reactor with a modified discharge circuit configuration. The schematic diagram of the reactor, along with a detailed description of the synthesis process and material characteristics, can be found in studies [16–18]. The reac-

tor is equipped with a direct current (DC) power source capable of regulating the current within a range of 20 to 220 A. The negative terminal of the power source was connected to an aluminum plate with openings designed to hold graphite crucibles, while the positive terminal was connected to a vertically positioned steel sleeve mounted above the aluminum plate. Starting powders were placed inside the cavity of the graphite crucible and sealed with a graphite lid. The arc discharge was initiated by establishing contact between the electrode and the crucible lid, after which the discharge was maintained for a predetermined duration before being terminated. The operating parameters of the arc reactor used during the synthesis of the powder materials are summarized in Table 1.

The ceramic samples were sintered using the spark plasma sintering (SPS) method with a GT Advanced Technologies SPS 10-4 system. During the fabrication process, the powder materials were simultaneously pressed and sintered under vacuum conditions. Five bulk cylindrical samples, each with a diameter of 12.7 mm and a height of 3 mm, were sintered under conditions selected based on literature data, as detailed in Table 2. The sintered samples included tablets made from boron carbide powders, as well as boron carbide with the addition of chromium carbide and chromium diboride. Before sintering each bulk sample, the starting powders or powder mixtures for each composition were milled in a tungsten carbide ball mill for 5 min.

The phase composition of the synthesized and sintered products was analyzed using X-ray diffraction (XRD) on a Shimadzu XRD 7000 diffractometer with  $\text{CuK}_{\alpha 1}$  radiation ( $\lambda = 1.54060 \text{ \AA}$ ). The microstructure and morphology of the synthesized and sintered materials were examined using a Tescan Vega 3 SBU scanning electron microscope (SEM) equipped with an Oxford X-Max 50 energy-dispersive X-ray spectroscopy (EDS) system featuring an Si/Li crystal detector. Transmission electron microscopy (TEM) was performed using a JEOL JEM 2100F microscope equipped with an EX-24063JGT EDS detector to analyze finer structural details.

The density of the sintered ceramic samples was measured using the hydrostatic weighing method

with a specialized attachment for HR-250AZ analytical balances (A&D Company) in distilled water. The hardness of the sintered ceramics was evaluated using a Pruftechnik KB-30S microhardness tester with a Vickers indenter under a load of 1 kg. The fracture toughness of the bulk samples was determined using the indentation method, by measuring the lengths of cracks emanating from the corners of the Vickers indentation marks, as observed in SEM images. These cracks were generated under the same 1 kg load applied with the Pruftechnik KB-30S microhardness tester.

## Research results and discussion

The X-ray diffraction analysis (Fig. 1) of the synthesized powder confirms the formation of boron carbide ( $\text{B}_4\text{C}$ ) (JCPDS No. 35-798, space group  $R\bar{3}m$ , rhombohedral crystal system) as a result of exposure to the thermal field generated by an arc discharge initiated in air under normal atmospheric pressure, with a current of 200 A and an exposure time of 60 s applied to the boron–carbon mixture. Notably, traces of unreacted elemental boron were detected in the XRD pattern, indicated by a broad halo within the angular range of  $2\theta = 10\div 20^\circ$ . In addition, a diffraction peak at  $2\theta \approx 26.1^\circ$ , corresponding to the graphite phase, was identified in the sample.

Fig. 1 also shows the XRD patterns of the synthesized chromium carbide and chromium diboride powders. According to the diffraction data, the chromium carbide powder consists of a crystalline  $\text{Cr}_3\text{C}_2$  phase (JCPDS No. 35-0804, orthorhombic structure), while the chromium diboride powder corresponds to the  $\text{CrB}_2$  phase (JCPDS No. 34-369, hexagonal structure).

The morphology of the synthesized boron carbide powder was examined using scanning electron microscopy (SEM). A representative SEM image is shown in Fig. 2.

The newly formed boron carbide particles appear as agglomerates with a broad size distribution ranging from  $\sim 100$  to  $\sim 500 \mu\text{m}$ , with the most frequent particle size falling within the  $100\text{--}150 \mu\text{m}$  range (Fig. 2, *a*, inset). According to elemental analysis, typical particles contain boron (78.93 at. %) and carbon (21.07 at. %),

Table 1. Parameters of synthesis of powder materials

Таблица 1. Параметры синтеза порошковых материалов

Material	Atomic ratio	Current, A	Arc discharge duration, s	Energy input, kWh
$\text{B}_4\text{C}$ [16]	4.00:1.00	200	60	0.061
$\text{Cr}_3\text{C}_2$ [17]	3.00:2.45			0.067
$\text{CrB}_2$ [18]	1.00:2.55			0.064

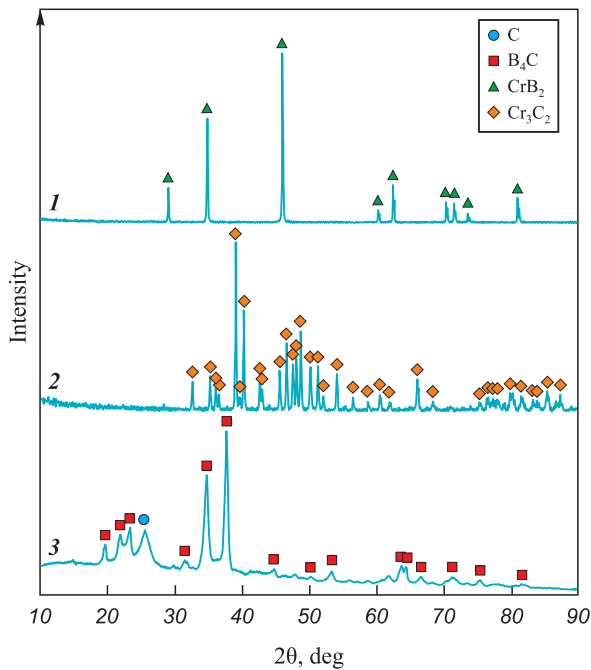


**Fig. 1.** Typical X-ray diffraction patterns of the synthesized  $\text{CrB}_2$ ,  $\text{Cr}_3\text{C}_2$  and  $\text{B}_4\text{C}$  powders  
1 – chromium diboride, 2 – chromium carbide, 3 – boron carbide

**Рис. 1.** Типичные картины рентгеновской дифракции синтезированных порошков  $\text{CrB}_2$ ,  $\text{Cr}_3\text{C}_2$  и  $\text{B}_4\text{C}$   
1 – диборид хрома, 2 – карбид хрома, 3 – карбид бора

with an atomic ratio consistent with the stoichiometry of boron carbide ( $\text{B}_4\text{C}$ ), as previously confirmed by XRD analysis. A small amount of impurities (not exceeding 2.0 at. %) was also detected in the samples.

Fig. 3 shows the results of transmission electron microscopy of the nanoscale fraction of the synthesized boron carbide ( $\text{B}_4\text{C}$ ) powder. As can be seen, the newly formed particles exhibit faceted features and a size distribution ranging from 200 to 700 nm, with most particles falling within the 400–500 nm range.

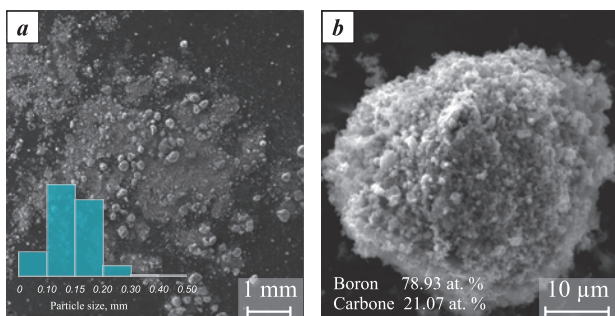


**Fig. 2.** Typical scanning electron microscopy images of the boron carbide sample in secondary electron mode (a) and backscattered electron mode (b)

**Рис. 2.** Типичный снимок растровой электронной микроскопии образца карбида бора в режимах вторичных (a) и обратно-рассеянных (b) электронов

The electron diffraction pattern (Fig. 3, c) reveals interplanar spacings of 3.80, 1.89, 1.71, 1.62, 1.40, 1.32, 1.31, 1.26, and 1.21 Å, which, within the permissible measurement error, correspond to the reference interplanar spacings of the  $\text{B}_4\text{C}$  phase (JCPDS No. 35-798, PDF-4+). Additionally, interplanar spacings of 2.34 and 2.09 Å were identified, corresponding within the measurement error to the reference values for the  $\text{B}_{13}\text{C}_2$  phase (JCPDS No. 71-108, PDF-4+). The identified  $\text{B}_{13}\text{C}_2$  phase represents a structural variant of boron carbide ( $\text{B}_4\text{C}$ ) and is a hyperstoichiometric phase relative to  $\text{B}_4\text{C}$ . Its formation is likely due to the development of localized regions with non-uniform distribution of the starting powders in the reaction zone [19].

Ceramic samples based on boron carbide ( $\text{B}_4\text{C}$ ), chromium carbide ( $\text{Cr}_3\text{C}_2$ ), and chromium diboride ( $\text{CrB}_2$ ) were subsequently fabricated using the spark plasma sintering (SPS) method. Based on previous studies [5–8], it has been established that the introduction of sintering additives in the form of chromium carbide and chromium diboride enhances the mechanical properties of the final ceramic products. According to the results of study [5], adding 20 wt. %  $\text{CrB}_2$  during the sintering of  $\text{B}_4\text{C}$ -based ceramic samples leads to composites with the highest fracture toughness and hardness. In contrast, the addition of 25 wt. %  $\text{Cr}_3\text{C}_2$  results in samples with the highest density [6], which

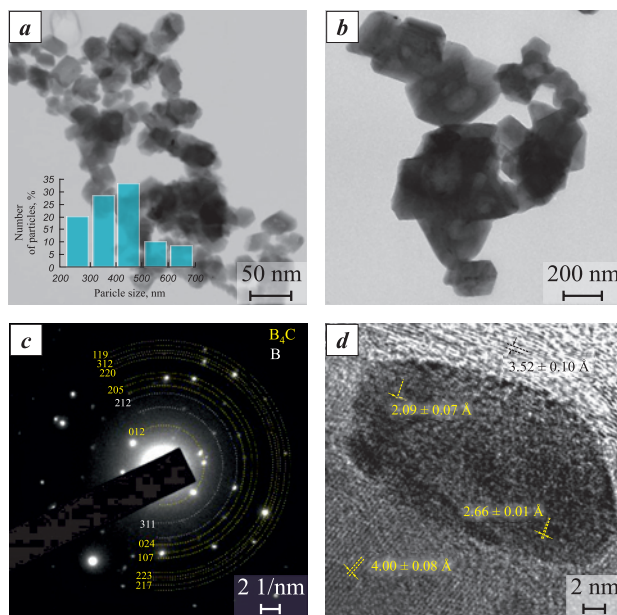


**Fig. 3.** Typical transmission electron microscopy results  
a – dark-field image, b – bright-field image,  
c – electron diffraction pattern, d – HRTEM image

**Рис. 3.** Типичные результаты просвечивающей электронной микроскопии  
a – темнопольный снимок, b – светлопольный снимок,  
c – электронная дифракция,  
d – снимок в режиме прямого разрешения

also contributes to improved mechanical properties of the bulk material. Therefore, to enhance the mechanical properties of the ceramics, samples were prepared from powders with the following additives:  $B_4C + 20 \text{ wt. \% CrB}_2$  and  $B_4C + 25 \text{ wt. \% Cr}_3C_2$ . To evaluate the effect of sintering additives on the properties of bulk ceramics, the characteristics of samples made from pure powders were compared with those of sintered samples containing additives. Chromium carbide and chromium diboride powders synthesized via the vacuum-free arc discharge method were used as sintering additives.

Fig. 4 presents scanning electron microscopy images of the sintered ceramic samples based on  $B_4C$ ,  $CrB_2$ , and  $Cr_3C_2$ . According to the XRD patterns, no phase transitions were detected after sintering, and the phase composition remained nearly identical to that of the powders synthesized by the vacuum-free arc discharge method.

The surface of the bulk boron carbide ( $B_4C$ ) sample (Fig. 4, *a-c*) exhibits distinct structural features, particularly regions with multiple clustered carbon particle (agglomerates) reaching up to up to  $\sim 17 \mu\text{m}$  in size. Additionally, changes in the phase composition

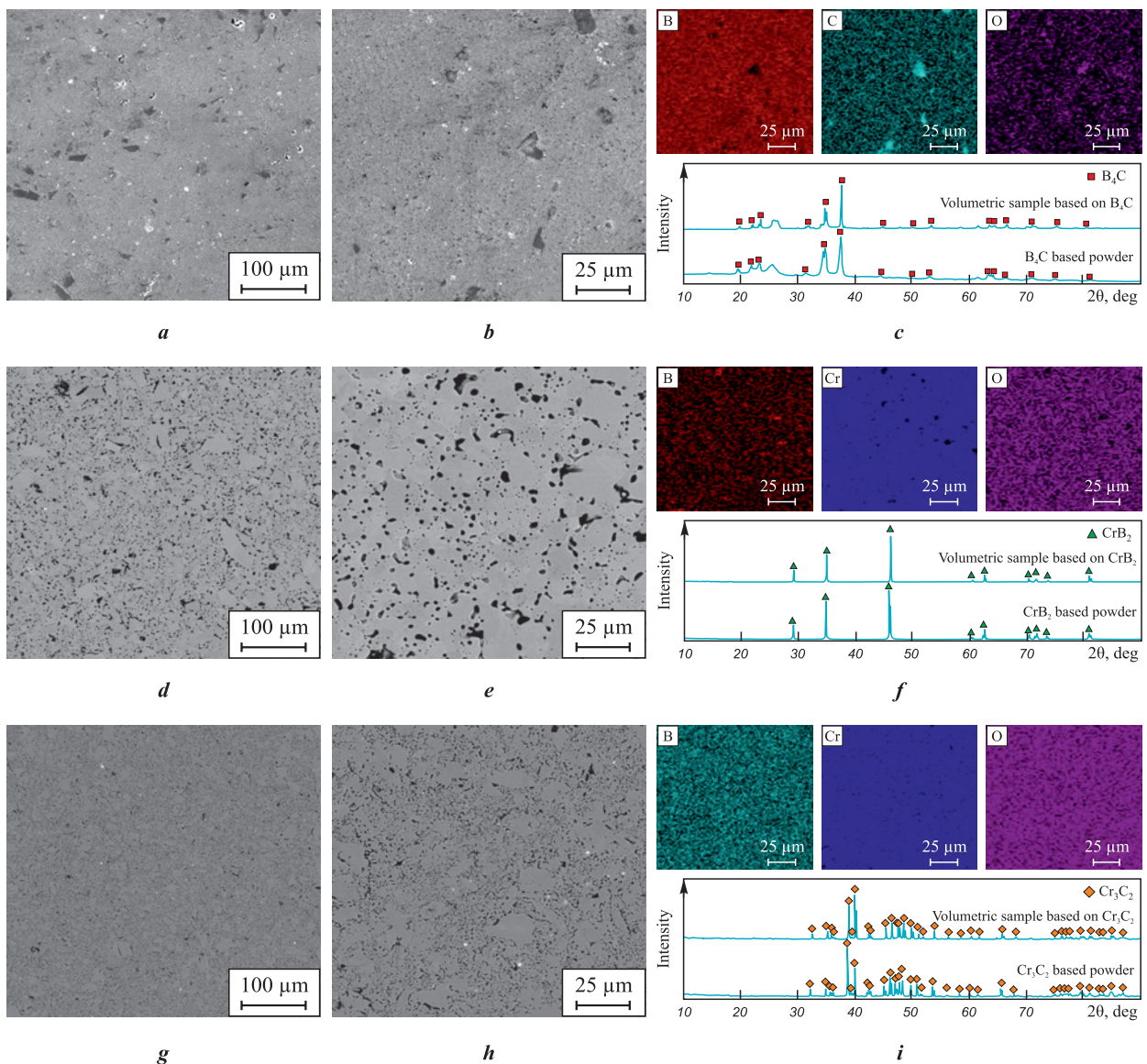


Fig. 4. Typical SEM images in backscattered electron mode with elemental distribution maps and XRD patterns of the ceramic samples  
*a-c* –  $B_4C$ ; *d-f* –  $CrB_2$ ; *g-i* –  $Cr_3C_2$

Рис. 4. Типичные РЭМ-снимки в режиме обратно-рассеянных электронов с картами распределения химических элементов и РФА керамического образца  
*a-c* –  $B_4C$ ; *d-f* –  $CrB_2$ ; *g-i* –  $Cr_3C_2$

of the bulk sample were observed compared to the starting powder. According to the X-ray diffraction analysis (Fig. 4, *c*), the diffraction halo within the angular range of  $2\theta = 10\div 20^\circ$ , corresponding to amorphous boron particles, becomes less pronounced after sintering. This change in phase composition can be attributed to the reaction between amorphous boron and carbon particles during the sintering process, leading to the formation of boron carbide ( $B_4C$ ) and the agglomeration of free carbon (Fig. 4, *c*, carbon distribution map).

Elemental analysis (Fig. 4, *c*) shows that the boron carbide sample contains boron (64.90 at. %) and carbon (29.03 at. %), with an atomic ratio consistent with the  $B_4C$  stoichiometry previously determined by XRD. In addition, trace amounts of oxide impurities (no more than 2.0 at. %) were identified in the sample. Elemental distribution maps also reveal the presence of oxide compounds on the sample surface (Fig. 4, *c*), which likely originate from the starting powders, such as boron oxide ( $B_2O_3$ ) particles present in the raw boron powder. However, the identification of these compounds via XRD is challenging due to their low concentration relative to the total sample volume.

SEM images of the chromium diboride ( $CrB_2$ ) ceramic (Fig. 4, *d-f*) reveal light and dark globular

regions on the sample surface at low magnifications, associated with the distribution of the primary components. Boron particle clusters up to  $\sim 10\ \mu m$  in size were also identified on the  $CrB_2$  sample surface. Elemental analysis (Fig. 4, *f*) indicates that the sample contains boron (69.80 at. %) and chromium (28.46 at. %) in an atomic ratio corresponding to the stoichiometry of  $CrB_2$ . A small amount of oxide compounds (not exceeding 2.0 at. %) was also detected on the sample surface.

The surface of the pure chromium carbide ( $Cr_3C_2$ ) ceramic sample (Fig. 4, *g-i*) also shows dark regions in the SEM images, corresponding to carbon particle agglomerates with sizes up to  $5\ \mu m$ . Elemental analysis confirms a uniform distribution of chromium and carbon, with average contents of 48.54 at. % (C) and 48.52 at. % (Cr). A small amount of oxide compounds (not exceeding 3.0 at. %) was also identified.

Fig. 5 presents SEM images and XRD results of the sintered boron carbide-based ceramic samples with additives (20 wt. %  $CrB_2$  and 25 wt. %  $Cr_3C_2$ ).

According to the X-ray diffraction analysis (Fig. 5, *a*), the sample sintered from boron carbide powder with the addition of 25 wt. % chromium

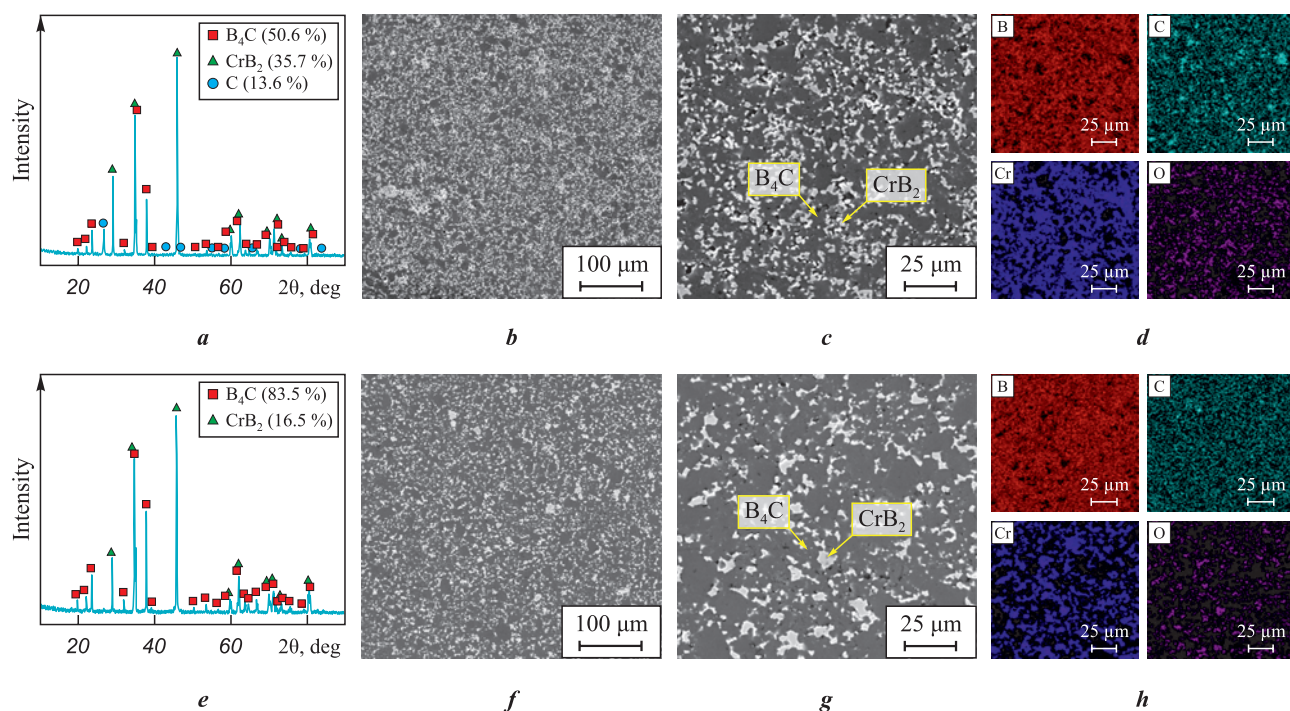


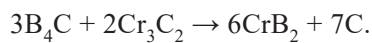
Fig. 5. Typical X-ray diffraction patterns and backscattered electron SEM images with elemental distribution maps of composite materials

*a-d* –  $B_4C + 25\ \text{wt. \% } Cr_3C_2$ ; *e-h* –  $B_4C + 20\ \text{wt. \% } CrB_2$

Рис. 5. Типичные картины рентгеновской дифракции и РЭМ-снимки в режиме обратно-рассеянных электронов с картами распределения химических элементов композиционных материалов

*a-d* –  $B_4C + 25\ \text{мас. \% } Cr_3C_2$ ; *e-h* –  $B_4C + 20\ \text{мас. \% } CrB_2$

carbide contains  $\text{CrB}_2$  (JCPDS No. 89-3533),  $\text{B}_4\text{C}$  (JCPDS No. 35-798), and C (JCPDS No. 75-3078) phases. The formation of chromium diboride during the sintering of the  $\text{B}_4\text{C} + 25 \text{ wt. } \% \text{Cr}_3\text{C}_2$  composite is attributed to the diffusion of boron atoms from the boron carbide phase into the chromium carbide phase at high temperatures. This process results in the formation of  $\text{CrB}_2$  and the release of free carbon from  $\text{B}_4\text{C}$  and  $\text{Cr}_3\text{C}_2$  compounds. The free carbon can either react with boron atoms to form additional boron carbide phases or accumulate in localized carbon-rich regions, as indicated by the carbon distribution map (Fig. 5, c). The formation of chromium diboride ( $\text{CrB}_2$ ) in this system follows the chemical reaction [20]:



The sample surface (Fig. 5, b, c) displays both light and dark regions. The light regions correspond to the  $\text{CrB}_2$  phase, while the darker areas are associated with boron carbide. Additionally, pores up to  $10 \mu\text{m}$  in size were observed.

Elemental analysis (Fig. 5, d) shows that the light regions represent the chromium diboride phase with traces of carbon. These areas contain carbon (20.57 at. %), boron (68.47 at. %), and chromium (10.96 at. %), confirming the presence of  $\text{CrB}_2$ . A small amount of oxide compounds (up to 1.10 at. %) was also

detected. According to the elemental analysis results, the dark regions correspond to the boron carbide phase, with elemental analysis revealing boron (72.11 at. %), carbon (24.5 at. %), and chromium (2.96 at. %), which is consistent with the  $\text{B}_4\text{C}$  phase composition. Minor impurities (up to 1.0 at. %) were also present in the sample.

Fig. 5, e–h shows the XRD results and SEM images of the sintered ceramic sample made from boron carbide powder with the addition of 20 wt. % chromium diboride, captured in secondary electron mode. The diffraction peaks observed in the XRD pattern (Fig. 5, e) correspond to the characteristic peaks of the crystalline phases  $\text{CrB}_2$  (JCPDS No. 89-3533) and  $\text{B}_4\text{C}$  (JCPDS No. 35-798).

The surface of the  $\text{B}_4\text{C} + 20 \text{ wt. } \% \text{CrB}_2$  sample (Fig. 5, f, g) features both light and dark regions, along with pores up to  $5 \mu\text{m}$  in size. The sample also displays distinct structural features, including carbon particle clusters measuring up to  $4 \mu\text{m}$ .

Elemental analysis (Fig. 5, h) reveals that the light regions contain boron (68.3 at. %), chromium (17.21 at. %), and carbon (12.99 at. %), indicating the presence of chromium diboride grains (Fig. 5, e). Oxygen was also detected in these regions, with a concentration of up to 1.5 at. %. In contrast, the dark regions contain boron (75.66 at. %), carbon (22.30 at. %), and chromium (1.66 at. %), suggesting these areas cor-

Table 2. Sintering parameters and characteristics of ceramic samples

Таблица 2. Параметры спекания и характеристики керамических образцов

Sintering method	Phase composition	Theoretical/measured density, $\text{g}/\text{cm}^3$	Relative density, %	Hardness, GPa	Sintering parameters				Reference
					$t$ , °C	$P$ , MPa	$\Delta t/\Delta \tau$ , °C/min	$\Delta \tau$	
Literature data									
SPS	$\text{B}_4\text{C}$	–	78.6	12.2	1850	60	100	5	[21]
SPS	$\text{B}_4\text{C}$	–	97.8	$35.3 \pm 2.6$	2100	50	50	10	[22]
SPS	$\text{CrB}_2$	–	97.0	16.0	1800	50	100	15	[23]
SPS	$\text{Cr}_3\text{C}_2$	–	98.9	18.9	1300	30	100	10	[24]
Hot pressing	$\text{B}_4\text{C} + 20 \text{ wt. } \% \text{CrB}_2$	–	99.0	–	1900	50	40	60	[5]
Hot pressing	$\text{B}_4\text{C} + 25 \text{ wt. } \% \text{Cr}_3\text{C}_2$	–	90.0	–	2030	–	10	60	[6; 8]
Experimental data from this study									
SPS	$\text{B}_4\text{C}$	2.52/2.40	95.2	$22.7 \pm 1.8$	1800	60	100	10	–
SPS	$\text{CrB}_2$	5.20/4.81	92.5	$12.6 \pm 0.3$	1800	60	100	10	–
SPS	$\text{Cr}_3\text{C}_2$	6.68/6.08	91.0	$11.4 \pm 0.1$	1300	30	100	10	–
SPS	$\text{B}_4\text{C} + 20 \text{ wt. } \% \text{CrB}_2$	2.92/2.81	96.2	$26.8 \pm 1.3$	1800	60	100	10	–
SPS	$\text{B}_4\text{C} + 25 \text{ wt. } \% \text{Cr}_3\text{C}_2$	3.43/3.03	88.3	$17.7 \pm 5.6$	1800	60	100	10	–

respond to boron carbide grains (Fig. 5, g). Trace amounts of oxide compounds (up to 1.0 at. %) were also identified in these regions.

The ceramic samples were subjected to Vickers hardness testing under a load of 1 kg. The test results, along with the sample characteristics, are presented in Table 2.

The theoretical density of the composite materials was calculated based on the phase composition of the bulk ceramic samples. Quantitative analysis of the crystalline phases (Fig. 5, a, e) was performed using PowderCell 2.4 software. Following this analysis, the theoretical density of the composite materials was determined using the density values of the identified phases ( $B_4C$ ,  $CrB_2$ , and C).

The data presented in Table 2 reveals the following hardness trend:  $B_4C + 20 \text{ wt. } \% CrB_2 > B_4C > B_4C + 25 \text{ wt. } \% Cr_3C_2 > CrB_2 > Cr_3C_2$ , specifically  $26.8 > 22.7 > 17.7 > 12.6 > 11.4 \text{ GPa}$ . The introduction of chromium diboride as a sintering additive led to an increase in the relative density of the bulk ceramic sample from 95.2 to 96.2 %, which is consistent with experimental data from [25]. This increase in density also contributed to improved mechanical properties, as reflected by the rise in hardness from 22.7 to 26.8 GPa.

The addition of chromium carbide during the sintering process resulted in a decrease in both the density and mechanical properties of the ceramic, reducing the hardness to 17.7 GPa. This decrease in relative density is attributed to the formation of porous regions containing a significant amount of free carbon. For the  $B_4C$  sample with  $Cr_3C_2$  addition, fracture toughness was also investigated. The results showed that the fracture toughness of pure boron carbide was  $2.5 \pm 0.2 \text{ MPa}\cdot\text{m}^{1/2}$ , while the introduction of 25 wt. %  $Cr_3C_2$  increased this value to  $3.3 \pm 0.3 \text{ MPa}\cdot\text{m}^{1/2}$ , which is comparable to the results reported in [5; 9].

## Conclusion

In this study, the fabrication of bulk ceramics based on compounds from the boron–carbon–chromium system was successfully demonstrated. The powders used for sintering the bulk samples included boron carbide ( $B_4C$ ), chromium carbide ( $Cr_3C_2$ ), and chromium diboride ( $CrB_2$ ). Notably, these powders were synthesized using a vacuum-free direct current arc reactor specifically developed by the authors of this research. The hardness of the  $B_4C$ -based ceramic was measured at 22.7 GPa, and the incorporation of 20 wt. %  $CrB_2$  as a sintering additive led to an increase in hardness to 26.8 GPa. Furthermore, the addition of 25 wt. %  $Cr_3C_2$  enhanced the fracture toughness

from 2.5 to 3.3  $\text{MPa}\cdot\text{m}^{1/2}$ . The hardness of ceramics based on chromium carbide and chromium diboride was found to be 11.4 and 12.6 GPa, respectively.

## References / Список литературы

1. Domnich V., Reynaud S., Haber R.A., Chhowalla M. Boron carbide: Structure, properties, and stability under stress. *Journal of the American Ceramic Society*. 2011; 94(11):3605–3628. <https://doi.org/10.1111/j.1551-2916.2011.04865.x>
2. Roy T.K., Subramanian C., Suri A.K. Pressureless sintering of boron carbide. *Ceramics International*. 2006; 32(3):227–233. <https://doi.org/10.1016/j.ceramint.2005.02.008>
3. Datye A., Koneti S., Gomes G., Wu K., Lin H. Synthesis and characterization of aluminum oxide–boron carbide coatings by air plasma spraying. *Ceramics International*. 2010;36(5):1517–1522. <https://doi.org/10.1016/j.ceramint.2010.02.024>
4. La Salvia J.C., Leavy R.B., Houskamp J.R., Miller H.T., MacKenzie D.E., Campbell J. Ballistic impact damage observations in a hot-pressed boron carbide. In: *Advances in ceramic armor V*. 2009;45–55. <https://doi.org/10.1002/9780470584330.ch5>
5. Yamada S., Hirao K., Yamauchi Y., Kanzaki S.  $B_4C$ – $CrB_2$  composites with improved mechanical properties. *Journal of the European Ceramic Society*. 2003;23(3):561–565. [https://doi.org/10.1016/S0955-2219\(02\)00094-8](https://doi.org/10.1016/S0955-2219(02)00094-8)
6. Li X., Jiang D., Zhang J., Lin Q., Chen Z., Huang Z. Pressureless sintering of boron carbide with  $Cr_3C_2$  as sintering additive. *Journal of the European Ceramic Society*. 2014;34(5):1073–1081. <https://doi.org/10.1016/j.jeurceramsoc.2013.11.036>
7. Chalgin A.V., Vikhman S.V., Ordan'yan S.S., Danilovich D.P., Nechaeva M.V. Principles of technology and mechanical properties of structural ceramics based on the ternary system  $SiC$ – $B_4C$ – $CrB_2$ . *MRS Online Proceedings Library (OPL)*. 2015;1765:11–16. <https://doi.org/10.1557/opl.2015.800>
8. Krutskii Yu.L., Nepochatov Yu.K., Pel' A.N., Skovorodin I.N., Dyukova K.D., Krutskaya T.M., Kuchumova I.D., Mats O.E., Tyurin A.G., Emurlaeva Yu.Yu., Podryabinkin S.I. Synthesis of polydisperse boron carbide and synthesis of a ceramic on its basis. *Russian Journal of Applied Chemistry*. 2019;92(6):750–758. <https://doi.org/10.1134/S1070427219060041>  
 Крутский Ю.Л., Непочатов Ю.К., Пель А.Н., Сквородин И.Н., Дюкова К.Д., Крутская Т.М., Кучумова И.Д., Матц О.Э., Тюрин А.Г., Эмурлаева Ю.Ю., Подрябинкин С.И. Синтез полидисперсного карбида бора и получение керамики на его основе. *Журнал прикладной химии*. 2019;92(6):719–727. <https://doi.org/10.1134/S1070427219060041>
9. Gudyma T.S., Shestakov V.A., Dik D.V., Krutskii Yu.L., Anisimov A.G., Cherkasova N.Yu., Ukhina A.V. Synthesis of  $B_4C/CrB_2$  powders by boron-carbide reduction using nanofiber carbon for the fabrication of ceramics. *Nanobiotechnology Reports*. 2023;18:S55–S62. <https://doi.org/10.1134/S2635167623600517>

10. Gao Y., Etzold A., Munhollon T., Rafaniello W., Haber R. Processing factors influencing the free carbon contents in boron carbide powder by rapid carbothermal reduction. *Diamond and Related Materials*. 2016;61:14–20. <https://doi.org/10.1016/j.diamond.2015.11.005>
11. Kovalev I.D., Ponomarev V.I., Vershinnikov V.I., Konovlikhin S.V. SHS-produced boron carbide: Some special features of crystal structure. *International Journal of Self-Propagating High-Temperature Synthesis*. 2012;21(2):134–138. <https://doi.org/10.3103/S1061386212020033>
12. Alkan M., Sonmez M.S., Derin B., Yücel O. Effect of initial composition on boron carbide production by SHS process followed by acid leaching. *Solid State Sciences*. 2012;14(11-12):1688–1691. <https://doi.org/10.1016/j.solidstatesciences.2012.07.004>
13. Ramos A.S., Taguchi S.P., Ramos E.C.T., Arantes V.L., Ribeiro S. High-energy ball milling of powder B–C mixtures. *Materials Science and Engineering: A*. 2006;422(1-2):184–188. <https://doi.org/10.1016/j.msea.2006.01.096>
14. Podgornyi V.I., Belashev B.Z., Osaulenko R.N., Ternovoi A.N. Synthesis of carbides in the arc plasma. *Technical Physics*. 2013;(58):1007–1010. <https://doi.org/10.1134/S1063784213070165>
15. Martynov R.S., Pak A.Ya., Volokitin O.G., Nikitin D.S., Larionov K.B., Povalyaev P.V., Gumovskaya A.A., Bolatova Zh., Vassilyeva Yu.Z. Advanced vacuumless arc plasma synthesis of boron carbide powders and bulk ceramics spark plasma sintering. *Bulletin of PNRPU. Mechanical Engineering, Materials Science*. 2023;25(3):65–76. (In Russ.). <https://doi.org/10.15593/2224-9877/2023.3.07>  
 Мартынов Р.С., Пак А.Я., Волокитин О.Г., Никитин Д.С., Ларионов К.Б., Поваляев П.В., Гумовская А.А., Болатова Ж., Васильева Ю.З. Синтез порошка карбида бора безвакуумным электродуговым методом и получение объемной керамики методом искрового плазменного спекания. *Вестник ПНИПУ. Машиностроение. Материаловедение*. 2023;25(3):65–76. <https://doi.org/10.15593/2224-9877/2023.3.07>
16. Vassilyeva Yu.Z., Povalyaev P.V., Neklya Yu.A., Pak A.Ya. Modernization of non-vacuum electric arc reactor for boron carbide powder synthesis. *Materials. Technologies. Design*. 2023;5(5):7–15. (In Russ.). [https://doi.org/10.54708/26587572\\_2023\\_55157](https://doi.org/10.54708/26587572_2023_55157)  
 Васильева Ю.З., Поваляев П.В., Некля Ю.А., Пак А.Я. Модернизация безвакуумного электродугового реактора для синтеза порошка на основе карбида бора. *Materials. Technologies. Design*. 2023;5(5):7–15. [https://doi.org/10.54708/26587572\\_2023\\_55157](https://doi.org/10.54708/26587572_2023_55157)
17. Povalyaev P.V., Pak A.Y., Frantsina E.V., Petrova Y.Y., Egorova V.V. Synthesis of chromium carbide powder by vacuum-free electric arc plasma method. *International Journal of Refractory Metals and Hard Materials*. 2024;123:106795. <https://doi.org/10.1016/j.ijrmhm.2024.106795>
18. Povalyaev P.V., Pak A.Y., Nikolaeva K.V., Danilova-Tret'yak S.M. Synthesis of chromium diboride in an arc-discharge atmospheric plasma. *Journal of Engineering Physics and Thermophysics*. 2024;97:1234–1245. <https://doi.org/10.1007/s10891-024-02996-x>  
 Поваляев П.В., Пак А.Я., Николаева К.В., Данилова-Третьяк С.М. Синтез диборида хрома в атмосферной плазме дугового разряда. *Инженерно-физический журнал*. 2024;97(5):1240. <https://doi.org/10.1007/s10891-024-02996-x>
19. Andrievski R.A. Micro- and nanosized boron carbide: synthesis, structure and properties. *Russian Chemical Reviews*. 2012;81(6):549–559. (In Russ.). <https://doi.org/10.1070/RC2012v081n06ABEH004287>  
 Андриевский Р.А. Микро- и наноразмерный карбид бора: синтез, структура и свойства. *Успехи химии*. 2012;81(6):549–559. <https://doi.org/10.1070/RC2012v081n06ABEH004287>
20. Rutkowski P., Stobierski L., Bućko M.M. The influence of chromium compounds on boron carbide sintering. *Composites Theory and Practice*. 2013;13(14):245–249.
21. Khasanov O.L., Dvilis E.S., Khasanov A.O., Bikbaeva Z.G., Polisadova V.V., Sokolov V.M., Kachaev A.A., Valova Ya.V. Determination of optimal modes of manufacturing high-density ceramics from boron carbide powder by sintering in spark discharge plasma. *Izvestiya Tomskogo Politehnicheskogo Universiteta*. 2012;320(2):58–62. (In Russ.).  
 Хасанов О.Л., Двилис Э.С., Хасанов А.О., Бикбаева З.Г., Полисадова В.В., Соколов В.М., Качаев А.А., Валова Я.В. Определение оптимальных режимов изготовления высокоплотной керамики из порошка карбида бора методом спекания в плазме искрового разряда. *Известия Томского политехнического университета*. 2012;320(2):58–62.
22. Badica P., Grasso S., Borodianska H., Xie S.S., Li P., Tartarok P., Reece M.J., Sakka Y., Vasylykiv O. Tough and dense boron carbide obtained by high-pressure (300 MPa) and low-temperature (1600 °C) spark plasma sintering. *Journal of the Ceramic Society of Japan*. 2014;122(1424):271–275. <https://doi.org/10.2109/jcersj.122.271>
23. Mahesh B., Sairam K., Sonber J.K., Murthy T.S.R.C., Nageswara Rao G.V.S., Srinivasa Rao T., Chakravarty J.K. Sinterability studies of monolithic chromium diboride (CrB<sub>2</sub>) by spark plasma sintering. *International Journal of Refractory Metals and Hard Materials*. 2015;52:66–69. <https://doi.org/10.1016/j.ijrmhm.2015.04.035>
24. Hirota K., Mitani K., Yoshinaka M., Yamaguchi O. Simultaneous synthesis and consolidation of chromium carbides (Cr<sub>3</sub>C<sub>2</sub>, Cr<sub>7</sub>C<sub>3</sub> and Cr<sub>23</sub>C<sub>6</sub>) by pulsed electric-current pressure sintering. *Materials Science and Engineering: A*. 2005;399(1–2):154–160. <https://doi.org/10.1016/j.msea.2005.02.062>
25. Yamada S., Hirao K., Yamauchi Y., Kanzaki S. Mechanical and electrical properties of B<sub>4</sub>C–CrB<sub>2</sub> ceramics fabricated by liquid phase sintering. *Ceramics International*. 2003;29(3):299–304. [https://doi.org/10.1016/S0272-8842\(02\)00120-7](https://doi.org/10.1016/S0272-8842(02)00120-7)

## Information about the Authors



**Yuliya Z. Vassilyeva** – Cand. Sci. (Eng.), Research Scientist, Laboratory of Advanced Materials for Energy Industry (LAMEI), National Research Tomsk Polytechnic University (NRTPU)

 **ORCID:** 0000-0002-6196-639X

 **E-mail:** yzv1@tpu.ru

**Pavel V. Povalyaev** – Junior Research Scientist, LAMEI, NRTPU

 **ORCID:** 0000-0001-6982-7258

 **E-mail:** pvp13@tpu.ru

**Anastasiya A. Kuznetsova** – Student, Weinberg Research Center, NRTPU

 **ORCID:** 0009-0002-6891-6130

 **E-mail:** aak264@tpu.ru

**Aleksandr Ya. Pak** – Dr. Sci. (Eng.), Head of the LAMEI, NRTPU

 **ORCID:** 0000-0001-8447-1309

 **E-mail:** ayapak@tpu.ru

## Сведения об авторах

**Юлия Захаровна Васильева** – к.т.н., науч. сотрудник лаборатории перспективных материалов энергетической отрасли (ЛПМЭО) Национального исследовательского Томского политехнического университета (НИТПУ)

 **ORCID:** 0000-0002-6196-639X

 **E-mail:** yzv1@tpu.ru

**Павел Вадимович Поваляев** – мл. науч. сотрудник ЛПМЭО, НИТПУ

 **ORCID:** 0000-0001-6982-7258

 **E-mail:** pvp13@tpu.ru

**Анастасия Андреевна Кузнецова** – студентка, Научно-образовательный центр Б.П. Вейнберга, НИТПУ

 **ORCID:** 0009-0002-6891-6130

 **E-mail:** aak264@tpu.ru

**Александр Яковлевич Пак** – д.т.н., заведующий ЛПМЭО, НИТПУ

 **ORCID:** 0000-0001-8447-1309

 **E-mail:** ayapak@tpu.ru

## Contribution of the Authors



## Вклад авторов

**Yu. Z. Vassilyeva** – developed the methodology, prepared the starting mixtures, analyzed the obtained samples, participated in the discussion of results, wrote the article, and revised the manuscript based on reviewers' comments.

**P. V. Povalyaev** – conducted the experiments, participated in the discussion of results, wrote the article, and handled reviewers' comments.

**A. A. Kuznetsova** – interpreted the analysis results, participated in the discussion of results, and wrote the article.

**A. Ya. Pak** – defined the research objectives, participated in the discussion of results, and secured funding.

**Ю. З. Васильева** – методология работы, подготовка исходных смесей, анализ полученных образцов, участие в обсуждении результатов, написание статьи, доработка статьи согласно рецензиям.

**П. В. Поваляев** – проведение экспериментов, участие в обсуждении результатов, написание статьи, работа с рецензиями.

**А. А. Кузнецова** – расшифровка результатов анализов, участие в обсуждении результатов, написание статьи.

**А. Я. Пак** – определение цели работы, участие в обсуждении результатов, обеспечение финансирования.

Received 13.11.2024

Revised 24.01.2025

Accepted 27.01.2025

Статья поступила 13.11.2024 г.

Доработана 24.01.2025 г.

Принята к публикации 27.01.2025 г.



UDC 621.762

<https://doi.org/10.17073/1997-308X-2025-3-15-24>Research article  
Научная статья

# Development of a polyoxymethylene-based feedstock for metal injection molding using 09Cr16Ni4Nb stainless steel powder

A. V. Parkhomenko<sup>1</sup>, A. P. Amosov<sup>1</sup> , A. M. Pastukhov<sup>2</sup><sup>1</sup> Samara State Technical University

244 Molodogvardeiskaya Str., Samara 443100, Russia

<sup>2</sup> Penza State University

40 Krasnaya Str., Penza 440026, Russia

 [egundor@yandex.ru](mailto:egundor@yandex.ru)

**Abstract.** Stainless steel powders are among the most widely used raw materials for the production of small, high-precision engineering components by metal injection molding (MIM), a process that combines metal powders with molten polymer binders. This study focuses on the development of feedstock composition and processing parameters for MIM production using domestically sourced components: a martensitic stainless steel powder grade 09Cr16Ni4Nb, a polyoxymethylene-based binder, and processing additives including stearic acid, beeswax, and low-density polyethylene. The starting stainless steel powder had a spherical morphology with a predominant particle size range of 8–23 μm. Scanning electron microscopy, melt flow index (MFI) testing, and helium pycnometry were employed to investigate the microstructure, rheological behavior, and physical properties of the resulting feedstock granules. Dependencies of MFI on the feedstock composition, metal-to-polymer ratio, type and content of additives, and particle size distribution of the metallic phase were established. The optimal feedstock formulation was determined experimentally. The microstructure and physical properties of sintered samples produced from the developed feedstock were evaluated and compared with those made from imported Catamold® feedstock. It was demonstrated that standard heat treatment modes are suitable for MIM-fabricated parts, as the phase transformation behavior of the studied steel does not differ from that of conventionally processed materials. The results confirm that components manufactured from the in-house feedstock comply with relevant regulatory standards and match the performance of their imported counterparts.

**Keywords:** MIM technology, injection molding, powder injection molding, feedstock, stainless steel powder, binder, polyoxymethylene, sintering, composition, structure

**For citation:** Parkhomenko A.V., Amosov A.P., Pastukhov A.M. Development of a polyoxymethylene-based feedstock for metal injection molding using 09Cr16Ni4Nb stainless steel powder. *Powder Metallurgy and Functional Coatings*. 2025;19(3):15–24. <https://doi.org/10.17073/1997-308X-2025-3-15-24>

# Разработка гранулята на полиформальдегидном связующем на основе порошка нержавеющей стали 09X16H4B для МИМ-технологии

А. В. Пархоменко<sup>1</sup>, А. П. Амосов<sup>1</sup>✉, А. М. Пастухов<sup>2</sup>

<sup>1</sup> Самарский государственный технический университет  
Россия, 443100, г. Самара, ул. Молодогвардейская, 244

<sup>2</sup> Пензенский государственный университет  
Россия, 440026, г. Пенза, ул. Красная, 40

✉ egundor@yandex.ru

**Аннотация.** Металлические порошки нержавеющей стали являются наиболее распространенными исходными материалами, применяемыми для производства малогабаритных высокоточных машиностроительных деталей по технологии инъекционного формования металлических порошков с расплавами полимеров (МИМ-технологии). Настоящая работа посвящена разработке состава и технологических режимов изготовления исходного сырья (гранулята) для производства деталей по МИМ-технологии из отечественных компонентов: порошка нержавеющей стали мартенситного класса 09X16H4B, связующего на основе полиформальдегида и технологических добавок (стеариновой кислоты, пчелиного воска и полиэтилена высокого давления). Исходный порошок нержавеющей стали имел сферическую форму частиц с размером основной массы частиц в диапазоне от 8 до 23 мкм. С применением сканирующей электронной микроскопии, метода определения показателя текучести расплава термопластов и пикнометрического метода исследовались микроструктуры, реологические и физические свойства полученных гранулятов. Установлены зависимости показателя текучести расплава (ПТР) от содержания исходных компонентов гранулята, соотношения металлической и полимерной частей, количества и вида технологических добавок, гранулометрического состава металлической части. Опытным путем определена оптимальная рецептура гранулята. Приведены результаты исследования микроструктуры и физических свойств опытных образцов, изготовленных по МИМ-технологии, в сравнении со спеченными образцами из импортного гранулята марки Catamold®. Показано, что для изделий, полученных по МИМ-технологии, целесообразно использовать типовые режимы термообработки, поскольку схемы фазовых превращений не отличаются от традиционных для данного вида стали. Установлено, что образцы из разработанного гранулята соответствуют требованиям нормативных документов на применяемый материал и не уступают по физическим показателям гранулятам импортного производства.

**Ключевые слова:** МИМ-технология, инъекционное формование, литье под давлением, гранулят, фидсток, порошок нержавеющей стали, связующее, полиформальдегид, спекание, состав, структура

**Для цитирования:** Пархоменко А.В., Амосов А.П., Пастухов А.М. Разработка гранулята на полиформальдегидном связующем на основе порошка нержавеющей стали 09X16H4B для МИМ-технологии. *Известия вузов. Порошковая металлургия и функциональные покрытия.* 2025;19(3):15–24. <https://doi.org/10.17073/1997-308X-2025-3-15-24>

## Introduction

The metal injection molding (MIM) process integrates the principles of powder metallurgy and polymer injection molding. This method involves the preparation of feedstock – a homogeneous mixture of fine metal powders and polymer binders – followed by injection molding of green parts, subsequent binder removal, and sintering to produce fully dense metallic components. MIM-produced parts combine the geometric complexity and dimensional precision typical of polymer-molded products with the mechanical strength inherent to metals [1]. A key advantage of MIM technology lies in its capability for high-volume production of small, intricately shaped components that generally require no further machining.

In metal injection molding, the starting material is a feedstock – a composite granulated material consisting of fine metal powders uniformly mixed with a polymer binder. Optimization of the feedstock composition is a critical step in ensuring the quality and efficiency of the MIM process. The typical volume fraction of metal powder in the feedstock ranges from 50 to 65 %, although it can be increased to 80 % or higher. However, increasing the metal powder content leads to a rise in the feedstock's viscosity, which may negatively affect the injection molding process [2; 3].

The characteristics of metal powders have a significant impact on the properties of final parts produced by the MIM process [4]. One of the key requirements for such powders is low surface energy, which facilitates effective mixing with the binder. This requirement

is best met by powders composed of spherical particles with diameters up to 50  $\mu\text{m}$ , preferably in the range of 1 to 5  $\mu\text{m}$ . For example, a granulometric analysis of BASF's Catamold<sup>®</sup> 42CrMo4 feedstock revealed that it consists of fine spherical metal powders with particle sizes ranging from 1 to 5  $\mu\text{m}$  [5].

Other important powder characteristics include particle shape, particle size distribution, and surface morphology. Particle shape affects the rheological behavior of the feedstock and the dimensional stability of the molded part during thermal processing. Irregularly shaped particles can enhance the mechanical strength of the part after binder removal, but they reduce packing density and increase feedstock viscosity. This, in turn, requires a higher binder content and may lead to excessive porosity in sintered components. The same applies to spherical particles with rough surfaces featuring protrusions and indentations [6]. Smooth, spherical particles are considered optimal for MIM technology due to their high packing density and low flow viscosity, although they may result in reduced strength of the debound parts. The most favorable performance in MIM is often achieved using mixtures of spherical and irregularly shaped particles [7; 8].

The average particle size of the powder is another critical parameter in MIM technology. Fine powders tend to agglomerate more readily, which makes them particularly suitable for MIM applications [9]. However, the minimum particle size is limited by the flowability of the powder–binder mixture: at elevated temperatures, smaller particles reduce the flowability of the feedstock, which negatively affects the injection molding process. The maximum particle size, on the other hand, influences the densification of the sintered component: larger particles decrease the likelihood of achieving high final density [10]. Improvements in the microstructure of sintered parts can be achieved by using powders with a bimodal particle size distribution, combining coarse and fine particles to reduce porosity by filling the interstitial voids between larger particles. As shown in [11], a broad particle size distribution enhances packing efficiency but complicates feedstock homogenization, thereby impairing uniform powder–binder dispersion during molding. By carefully controlling the shape and size of both spherical and irregular particles, it is possible to achieve high packing density and tailor the properties of the final components [12].

The range of metals used in metal injection molding is diverse and includes low-alloy steels, heat-resistant and corrosion-resistant alloys, as well as materials based on copper, nickel, cobalt, and titanium. In addition, intermetallics, magnetic alloys, carbides, and borides are also employed [13]. Unlike conventional

metalworking methods, where up to 80 % of the material may be lost as machining waste, the MIM process achieves a material utilization rate of approximately 99 %, which is particularly advantageous when working with high-cost metals such as stainless steels and titanium alloys. Recent international studies frequently report the use of spherical 17-4PH martensitic stainless steel powders [14–21]. For example, in [19], a gas-atomized 17-4PH stainless steel powder with particle sizes ranging from 4.8 to 30  $\mu\text{m}$  was employed. In [20], a water-atomized 17-4PH powder with near-spherical morphology was used. The authors of [21] utilized four different 17-4PH stainless steel powders varying in both particle size and morphology.

The binder plays a critical role in the metal injection molding process, as it must ensure low viscosity at high powder loading and remain chemically inert to facilitate effective mixing. Commonly used binders include low-molecular-weight polymers or waxes. Additives are often incorporated to adjust the binder's properties. One of the essential requirements for the binder system is its ability to provide sufficient viscosity to enable the molding of components with complex geometries. Another mandatory property is its ability to adequately wet the surface of the powder particles to optimize mixing and ensure proper shaping of the final part. To this end, surfactants such as titanates, silanes, phosphates, and stearates are introduced into the process to reduce the viscosity of the feedstock and increase solid loading by promoting interfacial adhesion between the powder and the binder.

Given that the MIM process is intended for manufacturing components with complex geometries, one of the essential requirements for binder components is adequate strength. High strength performance is typically achieved using polyoxymethylene (also known as polyacetal or polyformaldehyde) in the binder formulation. POM-based binder systems provide excellent mold filling and ensure the dimensional stability of molded parts. Components produced from such feedstock exhibit high strength and hardness, favorable fatigue properties, and minimal shrinkage upon sintering [22–24]. One of the most widely used binder systems in MIM technology consists of a composition based on polyoxymethylene, low-density polyethylene, and stearic acid. These components help preserve part geometry and structural integrity, even under conditions of increased porosity following polyoxymethylene removal [4].

One of the most critical properties of MIM feedstock is its homogeneity, which is essential for minimizing phase separation during injection molding and for achieving isotropic shrinkage during debinding and sintering. Inhomogeneous feedstock can

lead to visible defects in the final sintered part, as well as excessive porosity, cracking, and distortion. To achieve the required level of homogeneity, various types of mixers, crushers, mills, and screw extruders are employed. Effective mixing requires uniform shear throughout all regions of the mixing chamber. The most efficient solution is the use of a twin-screw extruder, which provides intensive shear combined with a short residence time of the metal–polymer compound at elevated temperatures [1].

To optimize the powder–binder composition and to select appropriate additives and modifiers during feedstock preparation, rheological tests are conducted to evaluate melt flow behavior. The molten feedstock is extruded through a die/nozzle of specified diameter under standard conditions to determine the melt flow index (MFI). This parameter characterizes the material’s ability to flow into the mold cavity during injection.

The aim of the present study was to develop a domestically produced metal powder feedstock based on stainless steel powder and a polyoxymethylene binder for the fabrication of steel parts by metal injection molding. In addition, the study aimed to establish relationships between the composition and structure of the metal–polymer compound, its processing parameters, and the physical, mechanical, rheological, and performance characteristics of both the feedstock and the resulting sintered MIM components.

## Materials and methods

To develop the feedstock, a spherical metal powder of low-carbon stainless steel grade 09Cr16Ni4Nb was used. The powder was produced by gas atomization and supplied by Polema JSC (Tula, Russia). The selected polymer binder was polyoxymethylene (POM) grade Tekhnaset A-110 (TU 2226–020–11517367), manufactured by Polyplastic Research and Production Company (Moscow, Russia). The surfactants used in the formulation included technical-grade stearic acid T-32 (GOST 6484–96), produced by Nefis Cosmetics (Kazan, Russia), and natural beeswax (GOST 21179–2000). To retain the structural integrity of the molded part after binder removal, low-density polyethylene (LDPE) grade 15813-020 (GOST 16337–22), produced by Kazanorgsintez PJSC (Kazan, Russia), was incorporated as a backbone binder component.

The particle size distribution of the metal powder was measured using an Analysette 22 Compact laser particle size analyzer (Fritsch GmbH, Germany). The microstructure of the starting materials and of the feedstocks developed from domestically sourced components was examined using a JSM-6390A scan-

ning electron microscope (JEOL, Japan). The rheological properties of the feedstock were evaluated in accordance with GOST 11645–73 using a Modular Melt Flow 7026 instrument (Ceast S.p.A., Italy) at a temperature of 190 °C and a load of 21.6 kgf. Density and inhomogeneity were measured with an AccuPyc 1340 helium pycnometer (Micromeritics, USA). The hardness of sintered parts was measured according to GOST 9013–59 using a WPM hardness testing machine (WPM Leipzig, Germany). Compression and tensile tests of sintered samples were carried out in accordance with GOST 18227–85 using an Instron 5988 universal testing machine (USA).

## Results and discussion

The starting 09Cr16Ni4Nb stainless steel powder exhibited a particle size distribution as shown in Fig. 1. The majority of the particles ranged from 8 to 23 μm in diameter, which meets the key requirements for metal powders intended for MIM feedstock production.

To determine the optimal ratio between the metallic and polymeric components, eight batches of feedstock with varying compositions were prepared. The feedstock was produced following a specific sequence of component mixing: stearic acid (SA) or beeswax (BW) was first added to the 09Cr16Ni4Nb stainless steel powder, followed by low-density polyethylene (LDPE), and finally polyoxymethylene (POM) was introduced. The granulation process was carried out under the following conditions:

Screw temperature, °C	160–180
Screw rotation speed, rpm	120–130
Pelletizer cutter speed, rpm	1100

The appearance of the resulting feedstock granules based on 09Cr16Ni4Nb stainless steel powder is shown in Fig. 2.

The results of melt flow index (MFI) and density measurements for the experimental batches of feedstock are presented in Table 1.

Beeswax and stearic acid were used as surfactants. The compositions containing beeswax (formulations 5–8) exhibited higher melt flow index (MFI) values, which, in turn, resulted in lower feedstock density. The MFI trends for the investigated feedstock formulations are shown in Fig. 3.

The most promising feedstocks were formulations 2 (with stearic acid) and 6 (with beeswax), which are recommended for further investigation.

Green parts of a component referred to as the “substrate” were molded using feedstock 2. Fig. 4, *a* shows the green part (left) and the sintered “substrate” com-

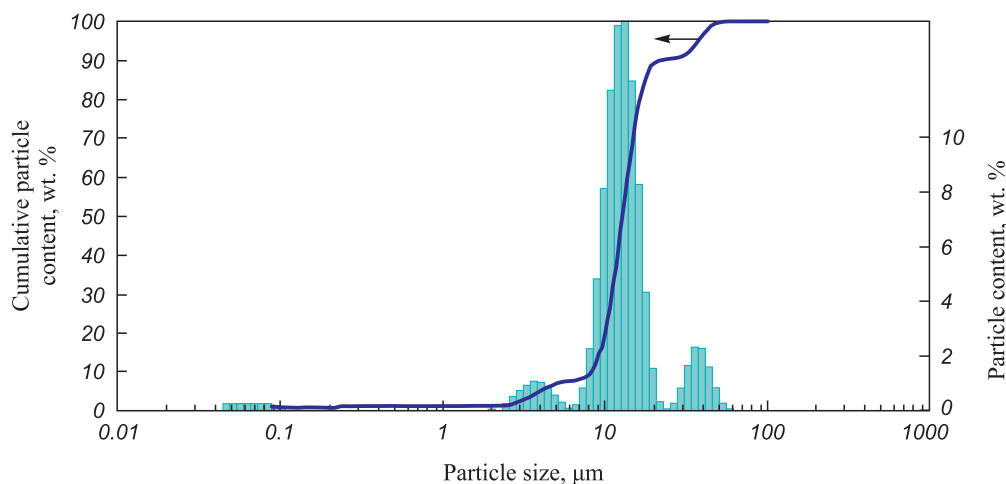


Fig. 1. Particle size distribution of the 09Cr16Ni4Nb stainless steel powder

Рис. 1. Гранулометрический состав порошка нержавеющей стали 09Х16Н4Б



Fig. 2. Appearance of the 09Cr16Ni4Nb feedstock granules

Рис. 2. Внешний вид гранулята 09Х16Н4Б

Injection molding of green parts using the 09Cr16Ni4Nb stainless steel powder was performed on a thermoplastic injection molding machine under the following conditions:

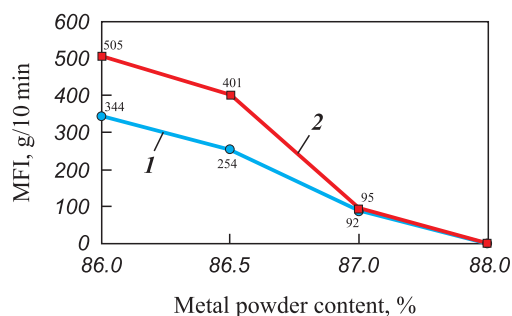


Fig. 3. Dependences of MFI on metal powder content in the feedstock

1 – formulations 1–4; 2 – formulations 5–8

Рис. 3. Зависимости ПТР от содержания металлической части в грануляте

1 – состав гранулятов 1–4; 2 – состав гранулятов 5–8

ponent (right). For comparative analysis, parts were also produced from imported Catamold® Stainless 17-4PH feedstock. Additionally, standard test samples were prepared for microstructural examination and mechanical property testing (Fig. 4, b), with dimensions in accordance with GOST R 59651–2021.

Table 1. Rheological and physical properties of feedstock granules based on 09Cr16Ni4Nb stainless steel powder

Таблица 1. Реологические и физические свойства гранулятов из порошка нержавеющей стали 09Х16Н4Б

Feedstock formulation No.	Component content, wt. %					MFI, g/10 min	Density, g/cm <sup>3</sup>
	09Cr16Ni4Nb	POM	LDPE	SA	BW		
1	86.0	11.5	1.0	1.5	–	344	4.2
2	86.5	11.0	1.0	1.5	–	254	4.6
3	87.0	10.5	1.0	1.5	–	92	4.5
4	88.0	9.5	1.0	1.5	–	0	4.6
5	86.0	11.5	1.0	–	1.5	505	4.2
6	86.5	11.0	1.0	–	1.5	401	4.2
7	87.0	10.5	1.0	–	1.5	95	4.4
8	88.0	9.5	1.0	–	1.5	0	4.5

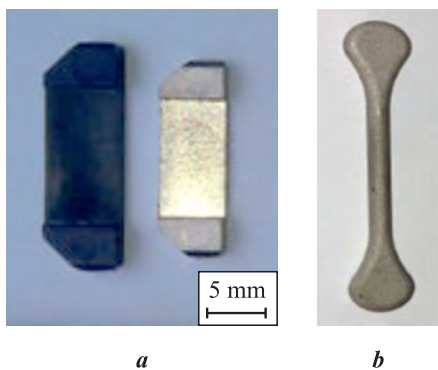


Fig. 4. Appearance of samples made from the developed feedstock

*a* – green part (left) and sintered substrate component (right)  
*b* – reference test sample

Рис. 4. Внешний вид образцов из разработанного гранулята  
*a* – заготовка (слева) и спеченная деталь «подложка» (справа)  
*b* – образцы-свидетели

Mold temperature, °C . . . . . 130 ± 10  
Injection pressure, МПа . . . . . 120 ± 10  
Shot volume, cm<sup>3</sup> . . . . . 10  
Temperature settings by zone, °C:  
nozzle . . . . . 190 ± 5  
zone 1 . . . . . 175 ± 5  
zone 2 . . . . . 180 ± 5  
zone 3 . . . . . 185 ± 5  
Aging in a press mould, s:  
mold holding . . . . . 5  
mold cooling . . . . . 10

Microstructural analysis of the green parts made from the metal–polymer composite revealed that samples produced from the imported Catamold® feedstock (Fig. 5, *b*) exhibited lower homogeneity and contained agglomerates of the metallic phase up to 15 μm in size. In contrast, the green parts produced from the domestically developed feedstock (Fig. 5, *a*) exhibited a homogeneous particle distribution.

Binder removal from the samples was carried out in a catalytic furnace using concentrated nitric acid vapor. The mass loss during debinding was approximately 7.5 %. The catalytic debinding parameters for green parts produced from 09Cr16Ni4Nb stainless steel powder are listed below:

Temperature, °C . . . . . 112 ± 5  
Purge time, min:  
before the cycle . . . . . 40  
after the cycle . . . . . 60  
Cycle duration, h . . . . . 5  
Acid feed rate, mL/min . . . . . 0.8

Sintering of the samples was carried out under vacuum at a heating rate of 5 °C/min up to a temperature of 1330 °C, with a holding time of 2 h.

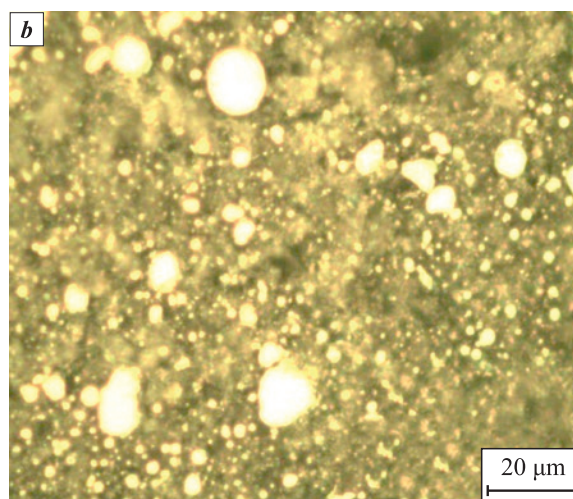
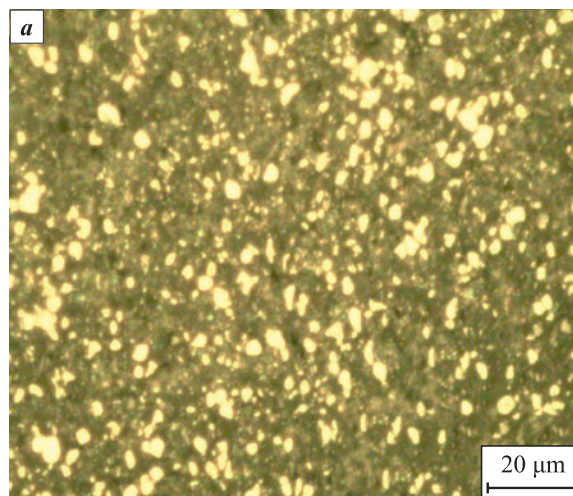


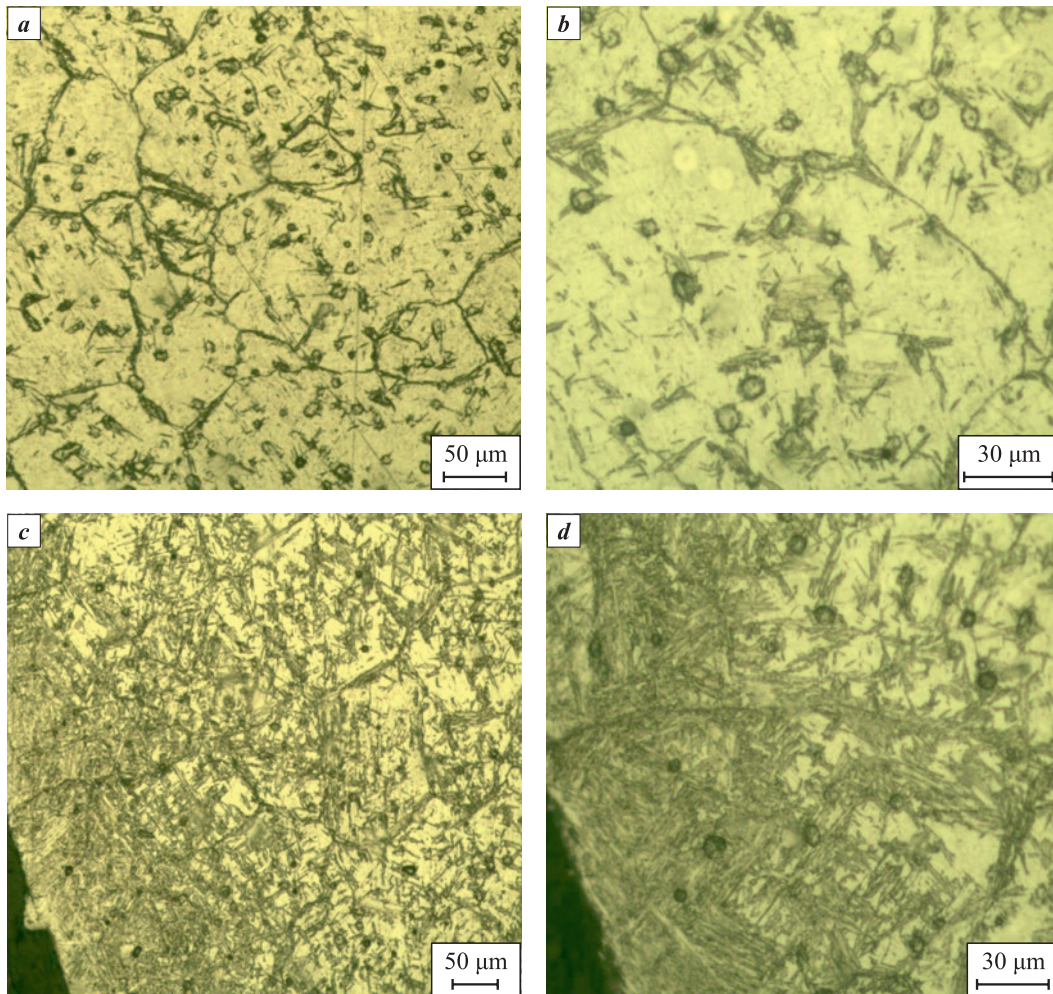
Fig. 5. Microstructure of the green part made from the in-house feedstock (*a*) and from Catamold® feedstock (*b*)

Рис. 5. Микроструктура заготовки из гранулята собственного производства (*a*) и из гранулята Catamold® (*b*)

The microstructures of the central region and the edge of the sintered 09Cr16Ni4Nb stainless steel sample produced by the MIM process using the in-house feedstock are shown in Fig. 6.

Metallographic analysis of the samples revealed that the microstructure of the sintered part was heterogeneous. The edge of the sample exhibited a martensitic structure, while the central region showed a granular ferrite–carbide structure with isolated areas of martensite. The presence of white regions indicated retained austenite. Additionally, microporosity was observed, which is characteristic of components produced by the MIM process.

Table 2 presents the physical and mechanical properties of sintered samples made from the in-house feedstock in comparison with those produced from imported Catamold® Stainless 17-4PH feedstock, as well as the requirements specified in GOST R 59651–2021.



**Fig. 6.** Microstructure of the central region (*a, b*) and edge (*c, d*) of the sample produced from the in-house feedstock after sintering

**Рис. 6.** Микроструктура центрального участка (*a, b*) и края (*c, d*) образца из гранулята собственного производства после спекания

The physical and mechanical properties of the sintered samples were found to meet the requirements of GOST R 59651–2021 for the target material and surpassed those of the imported equivalent. The sintered samples demonstrate high strength and hardness, indicative of increased brittleness.

A subsequent heat treatment cycle was performed in accordance with GOST 977–88, using the following parameters:

- normalizing at  $t = 1050\text{ °C}$  ( $\tau = 30\text{ min}$ ) in vacuum;
- tempering at  $t = 600\text{ °C}$  ( $\tau = 2\text{ h}$ ) in vacuum;

**Table 2. Physical and mechanical characteristics of sintered samples made from 09Cr16Ni4Nb stainless steel powder**

**Таблица 2. Физико-механические характеристики спеченных образцов из порошка нержавеющей стали 09X16H4Б**

Material	Ultimate tensile strength, $\sigma_u$ , kgf/mm <sup>2</sup>	Yield strength $\sigma_{0.2}$ , kgf/mm <sup>2</sup>	Elongation at break, %	Density $\rho$ , g/cm <sup>3</sup>	Vickers hardness (HV10)
Experimental 09Cr16Ni4Nb feedstock	162	106	8	7.87	440
Catamold® Stainless 17-4PH	81–97	66–76	≥6	≥7.65	264–301
GOST R 59651-2021	≥110	≥93	≥8	≥7.50	≥330

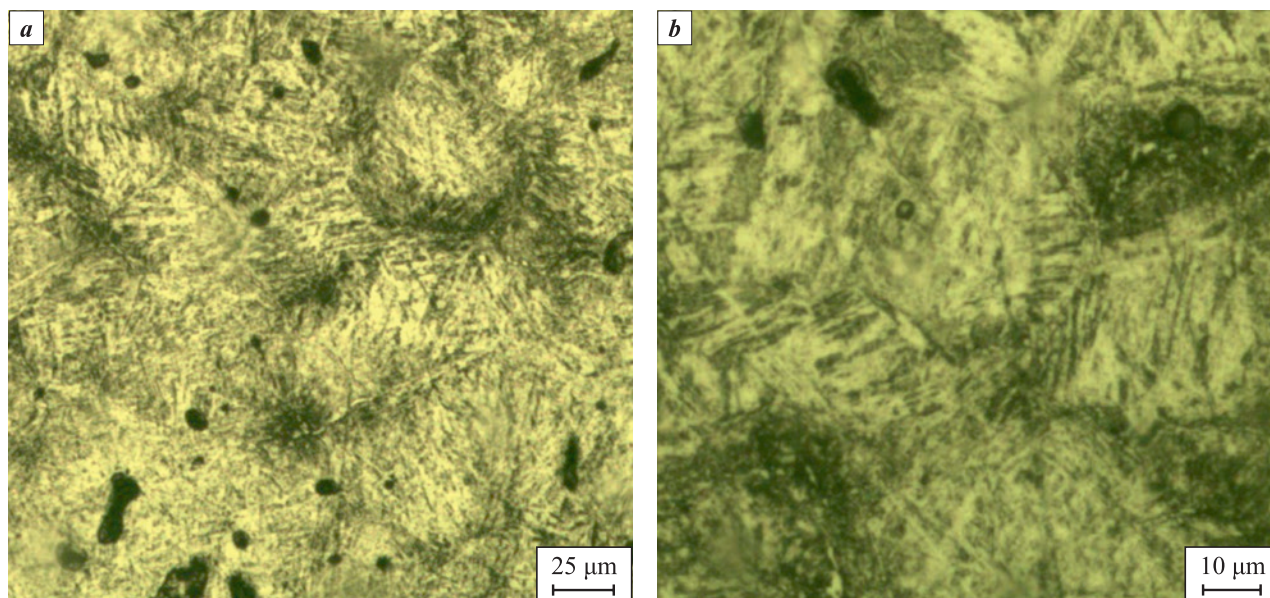


Fig. 7. Microstructure of the sample after heat treatment

Рис. 7. Микроструктура образца после термической обработки

Table 3. Physical and mechanical properties samples of stainless steel powder 09Cr16Ni4Nb after heat treatment

Таблица 3. Физико-механические свойства образцов из порошка нержавеющей стали 09X16H4B после термической обработки

Material	Ultimate tensile strength, $\sigma_w$ , kgf/mm <sup>2</sup>	Yield strength $\sigma_{0.2}$ , kgf/mm <sup>2</sup>	Elongation at break, %	Vickers hardness (HV10)	Density $\rho$ , g/cm <sup>3</sup>
09Cr16Ni4Nb feedstock	127	107	9	355	7.69
GOST R 59651-2021	$\geq 110$	$\geq 93$	$\geq 8$	$\geq 330$	$\geq 7.50$

– austenitizing with holding at  $t = 1050$  °C ( $\tau = 30$  min) in vacuum, followed by cooling to 100 °C;

– cryogenic treatment at  $-70$  °C ( $\tau = 4$  h);

– tempering at  $t = 300$  °C ( $\tau = 2$  h) in vacuum.

Cryogenic treatment was applied to reduce the amount of retained austenite and improve its stability in the samples [24].

Microstructural analysis performed after heat treatment revealed a tempered martensite structure with a medium acicular morphology. Residual microporosity was also observed, which is typical for samples produced using the MIM process (Fig. 7). The microporosity was not evaluated quantitatively, as the acceptability of parts is determined based on their physical and mechanical properties.

The physical and mechanical properties of the samples after heat treatment are presented in Table 3.

The results showed that heat treatment increases ductility and reduces the hardness and brittleness of the material by relieving internal stresses in the samples.

## Conclusions

1. Domestically produced feedstocks for MIM technology were developed using a polyoxymethylene binder and 09Cr16Ni4Nb stainless steel powder.

2. The effect of the ratio between polymer components and metal powder on the rheological properties of the feedstock was established.

3. The optimal ratio between the metal and polymer components of the feedstock was determined. The most suitable formulation is as follows, wt. %: 09Cr16Ni4Nb – 86.5; polyoxymethylene – 11.0; LDPE – 1.0; stearic acid – 1.5.

4. The microstructures of the sintered samples before and after heat treatment were studied. It was shown that the application of standard heat treatment modes is appropriate for MIM-fabricated parts, as the phase transformation diagrams are consistent with those of conventionally processed steel of this grade.

5. It was confirmed that steel components produced from the developed feedstock meet the physical and mechanical requirements specified in regulatory docu-

ments and are not inferior to parts manufactured from imported feedstock.

## References / Список литературы

- German R.M., Bose A. Injection molding of metals and ceramics. New Jersey, USA: Metal Powder Industries Federation, 1997. 414 p.
- Liu Z.Y., Loh N.H., Tor S.B., Khor K.A. Characterization of powder injection molding feedstock. *Materials Characterization*. 2002;49(4):313–320.  
[https://doi.org/10.1016/S1044-5803\(02\)00282-6](https://doi.org/10.1016/S1044-5803(02)00282-6)
- Li Y., Jiang F., Zhao L., Huang B. Critical thickness in binder removal process for injection molded compacts. *Materials Science and Engineering: A*. 2003;362(1–2):292–299.  
[https://doi.org/10.1016/S0921-5093\(03\)00613-0](https://doi.org/10.1016/S0921-5093(03)00613-0)
- Parkhomenko A.V., Amosov A.P., Samboruk A.R., Ignatov S.V., Kostin D.V., Shul'timova A.S. Development of domestic powder granulate with a polyformaldehyde-based binder for MIM-technology. *Russian Journal of Non-Ferrous Metals*. 2015;56(1):68–72.  
<https://doi.org/10.3103/S1067821215010149>  
Пархоменко А.В., Амосов А.П., Самборук А.Р., Игнатов С.В., Костин Д.В., Шул'тимова А.С. Разработка отечественного порошкового гранулята со связующим на основе полиформальдегида для МИМ-технологии. *Известия вузов. Порошковая металлургия и функциональные покрытия*. 2013;(4):8–13.  
<https://doi.org/10.17073/1997-308X-2013-4-8-13>
- Parkhomenko A.V., Amosov A.P., Samboruk A.R., Ermoshkin A.A. Investigation of composition and structure of imported granulate for MIM technology. In: *High technologies in mechanical engineering: Materials of the All-Russian Scientific and Technical Intellectual Conference with International Participation* (Samara, 11–17 November 2010). Samara: SSTU, 2010. P. 202–204. (In Russ.).  
Пархоменко А.В., Амосов А.П., Самборук А.Р., Ермошкин А.А. Исследование состава и структуры импортного гранулята для МИМ-технологии. В сб.: *Высокие технологии в машиностроении: Материалы Всероссийской научно-технической интеллектуальной конференции с международным участием* (Самара, 11–17 ноября 2010 г.). Самара: СамГТУ, 2010. С. 202–204.
- Contreras J.M., Jiménez-Morales A., Torralba J.M. Influence of particle size distribution and chemical composition of the powder on final properties of Inconel 718 fabricated by Metal Injection Moulding (MIM). *PIM International*. 2010;4(1):67–70.
- Ahn S., Park S.J., Lee Sh., Atre S.V., German R.M. Effect of powders and binders on material properties and molding parameters in iron and stainless steel powder injection molding process. *Powder Technology*. 2009;193(2):162–169.  
<https://doi.org/10.1016/j.powtec.2009.03.010>
- Mahmud N.N., Azam F.A.A., Ramli M.I., Foudzi F.M., Ameyama K., Sulong A.B. Rheological properties of irregular-shaped titanium-hydroxyapatite bimodal powder composite moulded by powder injection moulding. *Journal of Materials Research and Technology*. 2021;11:2255–2264.  
<https://doi.org/10.1016/j.jmrt.2021.02.016>
- Okubo K., Tanaka Sh., Ito H. The effects of metal particle size and distributions on dimensional accuracy for micro parts in micro metal injection molding. *Microsystem Technologies*. 2010;16:2037–2041.  
<https://doi.org/10.1007/s00542-010-1122-9>
- Sotomayor M.E., Várez A., Levenfeld B. Influence of powder particle size distribution on rheological properties of 316L powder injection molding feedstocks. *Powder Technology*. 2010;200(1–2):30–36.  
<https://doi.org/10.1016/j.powtec.2010.02.003>
- Meendering D.N., Malhotra D., Baltich L.K. Conditioning metal powder for injection molding: Patent 5314658 (USA). 1994.
- Barriere T., Liu B., Gelin J.C. Analyses of powder segregation in MIM. *Metal Powder Report*. 2002;57(5):30–33.  
[https://doi.org/10.1016/S0026-0657\(02\)80173-4](https://doi.org/10.1016/S0026-0657(02)80173-4)
- Parkhomenko A.V., Amosov A.P., Samboruk A.R. Development of metal powder applications for MIM technology. In: *High technologies in mechanical engineering: Materials of the All-Russian Scientific and Technical Intellectual Conference with International Participation* (Samara, 11–17 April 2024). Samara: SSTU, 2024. P. 285–289. (In Russ.).  
Пархоменко А.В., Амосов А.П., Самборук А.Р. Развитие применения металлических порошков для МИМ-технологии. В сб.: *Высокие технологии в машиностроении: Материалы XXI Всероссийской научно-технической конференции с международным участием* (Самара, 10–12 апреля 2024 г.). Самара: СамГТУ, 2024. С. 285–289.
- Pandey A.K., Chaudhari A.P., Vemula P., Sunil B., Nayak K.Ch., Date P.P. Effect of powder loading and testing condition on the different properties of metal injection molding parts. *Materials Today: Proceedings*. 2020;33(8):5492–5497.  
<https://doi.org/10.1016/j.matpr.2020.03.309>
- Haihong Ma, Shuo Li, Zhesheng Jin, Yiwen Tian, Fengmei Ren, Zhengfa Zhou, Weibing Xu. Effect of 17-4PH stainless steel powders interaction on feedstocks. *Powder Technology*. 2020;372:204–211.  
<https://doi.org/10.1016/j.powtec.2020.05.106>
- Mukundab B.N., Hausnerovaac B. Variation in particle size fraction to optimize metal injection molding of water atomized 17-4PH stainless steel feedstocks. *Powder Technology*. 2020;368:130–136.  
<https://doi.org/10.1016/j.powtec.2020.04.058>
- Machaka R., Ndlangamandla P., Seeranea M. Capillary rheological studies of 17-4PH MIM feedstocks prepared using a custom CSIR binder system. *Powder Technology*. 2018; 326:37–43. <https://doi.org/10.1016/j.powtec.2017.12.051>
- Basir A., Bakar A., Nashrah S., Jamadon H., Muhammad N. Feedstock properties and debinding mechanism of yttria-stabilized zirconia / stainless steel 17-4PH micro-components fabricated via two-component micro-powder injection molding process. *Ceramics International*. 2021;47(14):20476–20485.  
<https://doi.org/10.1016/j.ceramint.2021.04.057>

19. Naranjo J.A., Berges C., Campana R., Herranz G. Rheological and mechanical assessment for formulating hybrid feedstock to be used in MIM & FFF. *Results in Engineering*. 2023;19:101258.  
<https://doi.org/10.1016/j.rineng.2023.101258>
20. Langlais D., Demers V., Brailovski V. Rheology of dry powders and metal injection molding feedstocks formulated on their base. *Powder Technology*. 2022;396(A):13–26.  
<https://doi.org/10.1016/j.powtec.2021.10.039>
21. Ammosova L., Cano S.C., Schuschnigg S., Kukla C., Mönkkönen K., Suvanto M., Gonzalez-Gutierrez J. Effect of metal particle size and powder volume fraction on the filling performance of powder injection moulded parts with a micro textured surface. *Precision Engineering*. 2021;72:604–612.  
<https://doi.org/10.1016/j.precisioneng.2021.06.014>
22. Wohlfrom H., Maat R.F.J., Blomacher M. Metal powder injection molding material and metal powder injection molding method: Patent 2006/0099103A1 (USA). 2006.
23. Berlin A.A., Deberdeev R.Ya., Perukhin Yu.V., Garipov R.M. Polyoxymethylenes. Moscow.: Nauka, 2008. 286 p. (In Russ.).  
 Берлин А.А., Дебердеев Р.Я., Перухин Ю.В., Гарипов Р.М. Полиоксиметилены. М.: Наука, 2008. 286 с.
24. Grinberg E.M., Goncharov S.S., Markova E.V. The heat treatment modes effect on residue austenite amount in 09Cr16Ni4Nb cast steel. *Izvestiya TulGU. Technical Sciences*. 2012;6(2):280–285. (In Russ.).  
 Гринберг Е.М., Гончаров С.С., Маркова Е.В. Влияние режимов термической обработки на количество остаточного аустенита в стали 09Х16Н4БЛ. *Известия ТулГУ. Технические науки*. 2012;6(2):280–285.

### Information about the Authors



### Сведения об авторах

**Andrei V. Parkhomenko** – Graduate Student of the Department of Metallurgy, Powder Metallurgy, Nanomaterials (MPMN), Samara State Technical University (SamSTU)  
**ORCID:** 0009-0007-0442-0044  
**E-mail:** parhomandr@gmail.com

**Андрей Валерьевич Пархоменко** – аспирант кафедры «Металловедение, порошковая металлургия, наноматериалы» (МПМН) Самарского государственного технического университета (СамГТУ)  
**ORCID:** 0009-0007-0442-0044  
**E-mail:** parhomandr@gmail.com

**Aleksandr P. Amosov** – Dr. Sci. (Phys.-Math.), Professor, Head of the Department of MPMN, SamSTU  
**ORCID:** 0000-0003-1994-5672  
**E-mail:** egundor@yandex.ru

**Александр Петрович Амосов** – д.ф.-м.н., проф., заведующий кафедрой МПМН, СамГТУ  
**ORCID:** 0000-0003-1994-5672  
**E-mail:** egundor@yandex.ru

**Alexandr M. Pastukhov** – Graduate Student of the Department of Information and Measuring Equipment and Metrology, Penza State University  
**ORCID:** 0009-0003-6566-9872  
**E-mail:** alexpastuch@mail.ru

**Александр Михайлович Пастухов** – аспирант кафедры «Информационно-измерительная техника и метрология» Пензенского государственного университета  
**ORCID:** 0009-0003-6566-9872  
**E-mail:** alexpastuch@mail.ru

### Contribution of the Authors



### Вклад авторов

**A. V. Parkhomenko** – formulation of research objectives, experimental planning, participation in experiments, preparation and presentation of experimental results, participation in data analysis and discussion, writing and editing of the manuscript.

**А. В. Пархоменко** – постановка задач исследования, планирование экспериментов, участие в проведении экспериментов, подготовка и оформление результатов экспериментов, участие в анализе и обсуждении результатов, написание и редактирование текста статьи.

**A. P. Amosov** – definition of the research goal, synthesis of the obtained results, participation in manuscript writing.

**А. П. Амосов** – определение цели работы, обобщение полученных результатов, участие в написании статьи.

**A. M. Pastukhov** – conducting experiments, preparation and presentation of experimental results, participation in data analysis and discussion.

**А. М. Пастухов** – проведение экспериментов, подготовка и оформление результатов экспериментов, участие в анализе и обсуждении результатов.

Received 31.03.2025  
 Revised 02.05.2025  
 Accepted 05.05.2025

Статья поступила 31.03.2025 г.  
 Доработана 02.05.2025 г.  
 Принята к публикации 05.05.2025 г.



UDC 544.452 + 621.762.2 + 666.3

<https://doi.org/10.17073/1997-308X-2025-3-25-38>Research article  
Научная статья

# Self-propagating high-temperature synthesis of a highly dispersed $\text{Si}_3\text{N}_4$ -SiC ceramic powders composition using sodium azide and polytetrafluoroethylene

I. A. Uvarova, A. P. Amosov<sup>✉</sup>, Yu. V. Titova, V. A. NovikovSamara State Technical University  
244 Molodogvardeiskaya Str., Samara 443100, Russia[✉ egundor@yandex.ru](mailto:egundor@yandex.ru)

**Abstract.** Refractory ceramic composite materials of the silicon nitride–silicon carbide ( $\text{Si}_3\text{N}_4$ -SiC) system possess a wide range of valuable properties and are used across various industrial fields as excellent refractories, structural heat-resistant materials capable of withstanding high mechanical loads at elevated temperatures, and lightweight functional materials for microwave radiation shielding in aviation and aerospace applications. The performance of  $\text{Si}_3\text{N}_4$ -SiC composite ceramics can be significantly enhanced by increasing the dispersion of the component powders, transitioning from micron-sized particles to highly dispersed powders ( $<1 \mu\text{m}$ ). This study focuses on improving a simple, energy-efficient method of azide self-propagating high-temperature synthesis (SHS) for obtaining such highly dispersed powder compositions, using mixtures of sodium azide ( $\text{NaN}_3$ ) with elemental silicon and carbon powders, activated and modified by carbiding addition of powdered polytetrafluoroethylene (PTFE). These charge compositions, in both bulk and pressed forms, were combusted in a nitrogen atmosphere at 3 MPa. The maximum pressure and solid product yield were measured. The phase composition and microstructure of the combustion products were examined using X-ray diffraction (XRD) and scanning electron microscopy (SEM). The introduction of PTFE as a reactive carbiding and activating additive effectively overcame the limitations of conventional azide SHS processes that use halide salts such as  $\text{NH}_4\text{F}$ ,  $\text{Na}_2\text{SiF}_6$ , and  $(\text{NH}_4)_2\text{SiF}_6$ . In addition to ensuring a high dispersion of the synthesized powders, the phase composition – particularly for the pressed charges – became significantly closer to the target theoretical composition. Notably, the silicon carbide content in the  $\text{Si}_3\text{N}_4$ -SiC product increased substantially, while the amounts of free silicon and carbon impurities decreased.

**Keywords:** silicon nitride, silicon carbide, powder compositions, self-propagating high-temperature synthesis, sodium azide, polytetrafluoroethylene, combustion products, phase composition, microstructure

**Acknowledgements:** The work was supported by the Russian Science Foundation under grant No. 23-29-00680.

**For citation:** Uvarova I.A., Amosov A.P., Titova Yu.V., Novikov V.A. Self-propagating high-temperature synthesis of a highly dispersed  $\text{Si}_3\text{N}_4$ -SiC ceramic powders composition using sodium azide and polytetrafluoroethylene. *Powder Metallurgy and Functional Coatings*. 2025;19(3):25–38. <https://doi.org/10.17073/1997-308X-2025-3-25-38>

# Самораспространяющийся высокотемпературный синтез высокодисперсной композиции керамических порошков $\text{Si}_3\text{N}_4$ – $\text{SiC}$ с применением азида натрия и политетрафторэтилена

И. А. Уварова, А. П. Амосов<sup>✉</sup>, Ю. В. Титова, В. А. Новиков

Самарский государственный технический университет  
Россия, 443100, г. Самара, ул. Молодогвардейская, 244

✉ egundor@yandex.ru

**Аннотация.** Тугоплавкие керамические композиционные материалы системы «нитрид кремния – карбид кремния» ( $\text{Si}_3\text{N}_4$ – $\text{SiC}$ ) обладают широким спектром ценных свойств и находят применение в различных промышленных областях в качестве прекрасных огнеупоров, конструкционных жаропрочных материалов в условиях больших механических нагрузок при высоких температурах, легких функциональных материалов для защиты от микроволнового излучения в авиации и космонавтике. Свойства композиционной керамики  $\text{Si}_3\text{N}_4$ – $\text{SiC}$  могут существенно улучшаться при повышении дисперсности компонентов композита, при переходе от компонентов микронных размеров к высокодисперсным (<1 мкм). Работа посвящена усовершенствованию простого энергосберегающего метода азидного самораспространяющегося высокотемпературного синтеза (СВС) композиций таких порошков из смесей порошка азида натрия ( $\text{NaN}_3$ ) и элементных порошков кремния и углерода за счет использования активирующей и карбидизирующей добавки порошкового политетрафторэтилена (ПТФЭ). Эти смеси (шихты) в насыпном и прессованном виде сжигались в реакторе с давлением газообразного азота 3 МПа. Измерялись максимальное давление и выход твердых продуктов горения. С применением сканирующей электронной микроскопии и рентгенофазового анализа определялись микроструктура и фазовый состав продуктов горения. Использование добавки ПТФЭ позволило устранить недостатки традиционного азидного СВС композиций  $\text{Si}_3\text{N}_4$ – $\text{SiC}$  с применением галоидных солей  $\text{NH}_4\text{F}$ ,  $\text{Na}_2\text{SiF}_6$  и  $(\text{NH}_4)_2\text{SiF}_6$ . При сохранении высокой дисперсности синтезированных композиций порошков  $\text{Si}_3\text{N}_4$ – $\text{SiC}$  их фазовый состав, особенно при использовании прессованных шихт, стал значительно ближе к задаваемому теоретическому составу, существенно увеличилось содержание карбида кремния в синтезированном продукте  $\text{Si}_3\text{N}_4$ – $\text{SiC}$  при уменьшении содержания примесей свободных кремния и углерода.

**Ключевые слова:** нитрид кремния, карбид кремния, композиции порошков, самораспространяющийся высокотемпературный синтез, азид натрия, политетрафторэтилен, продукты горения, состав, структура

**Благодарности:** Работа выполнена при поддержке Российского научного фонда в рамках гранта № 23-29-00680.

**Для цитирования:** Уварова И.А., Амосов А.П., Титова Ю.В., Новиков В.А. Самораспространяющийся высокотемпературный синтез высокодисперсной композиции керамических порошков  $\text{Si}_3\text{N}_4$ – $\text{SiC}$  с применением азида натрия и политетрафторэтилена. *Известия вузов. Порошковая металлургия и функциональные покрытия.* 2025;19(3):25–38.  
<https://doi.org/10.17073/1997-308X-2025-3-25-38>

## Introduction

Refractory ceramic composite materials of the silicon nitride–silicon carbide ( $\text{Si}_3\text{N}_4$ – $\text{SiC}$ ) system possess a wide range of valuable properties and are used in various industrial applications. Primarily, these materials are excellent refractories and can be used at high temperatures (up to 1500 °C) due to their outstanding oxidation and creep resistance, chemical stability, low thermal expansion coefficient, and thermal shock resistance [1]. Such refractories are typically produced by reaction bonding of  $\text{SiC}$  powder with  $\text{Si}_3\text{N}_4$  particles synthesized via direct nitridation of silicon in a pressed powder mixture of  $\text{SiC}$  and  $\text{Si}$  under a nitrogen atmosphere at elevated temperatures (1300–1450 °C) for several hours [1; 2]. The resulting product is a two-

phase mixture of  $\alpha$ - $\text{Si}_3\text{N}_4$  and  $\beta$ - $\text{Si}_3\text{N}_4$ . The density and mechanical strength of the composites increase with a higher content of the fibrous  $\alpha$ - $\text{Si}_3\text{N}_4$  phase, which is promoted by reducing the particle sizes of  $\text{SiC}$  and  $\text{Si}$ , as well as by the presence of trace oxygen impurities in the nitrogen atmosphere. This oxygen leads to intensive oxidation of silicon, formation of  $\text{SiO}$  vapor, and gas-phase synthesis of  $\alpha$ - $\text{Si}_3\text{N}_4$  [1; 2]. While commercially produced silicon carbide refractories (without  $\text{Si}_3\text{N}_4$  in their composition) exhibit a compressive strength of up to 100 MPa at approximately 20 % porosity [3], a reaction-bonded composite with a composition of 46 $\text{SiC}$ –50 $\text{Si}_3\text{N}_4$ –4 $\text{Y}_2\text{O}_3$  (wt. %) demonstrates a compressive strength of 319 MPa at 26 % porosity [1].

Si<sub>3</sub>N<sub>4</sub>–SiC composite refractories are also produced by other methods such as semi-dry pressing (with up to 8 % liquid binder), plastic forming (up to 24 % binder), and slip casting (with up to 80 % water), followed by drying and sintering at temperatures up to 1600 °C [4–6]. In these methods, the starting materials are typically mixtures of polydisperse Si<sub>3</sub>N<sub>4</sub> and SiC micropowders, with particle sizes ranging from fine fractions (1–5 μm) to coarse ones (50–200 μm), to achieve optimal packing density in both the powder mixture and the final composite. However, the use of such relatively coarse powders, combined with a porosity of approximately 20 %, limits the ability of Si<sub>3</sub>N<sub>4</sub>–SiC refractories to reach their maximum mechanical strength, particularly at elevated temperatures.

To use Si<sub>3</sub>N<sub>4</sub>–SiC composites as structural heat-resistant materials under high mechanical loads at elevated temperatures (e.g., in gas turbine engines), or as ultra-hard tooling and wear-resistant materials, it is essential to achieve the highest possible values of hardness, strength, and fracture toughness. To achieve near-theoretical density and reduce porosity to below one percent, alternative fabrication methods must be employed. These include pressureless sintering of Si<sub>3</sub>N<sub>4</sub> and SiC powder mixtures at temperatures up to 2000 °C (including liquid-phase sintering), hot pressing, hot isostatic pressing, spark plasma sintering, and additive manufacturing techniques [5; 7–10]. Numerous studies utilizing these methods have shown that the mechanical properties of Si<sub>3</sub>N<sub>4</sub>–SiC composite ceramics improve significantly with increased fineness of the constituent powders – that is, as particle sizes are reduced from the micron scale to highly dispersed (<1 μm), submicron (0.1–1.0 μm), and even nanoscale (1–100 nm) dimensions. Consequently, considerable research efforts are currently focused on the development of nanostructured Si<sub>3</sub>N<sub>4</sub>–SiC ceramic composites [11–15]. In addition to enhanced mechanical performance, Si<sub>3</sub>N<sub>4</sub>–SiC nanocomposites exhibit improved microwave absorption properties, making them promising candidates for use as lightweight functional materials for electromagnetic shielding in aerospace and aviation applications [16].

At first glance, the *ex situ* fabrication of Si<sub>3</sub>N<sub>4</sub>–SiC nanocomposites – based on mechanical mixing of pre-synthesized Si<sub>3</sub>N<sub>4</sub> and SiC nanopowders followed by compaction and sintering – appears to be the most straightforward approach. However, such nanopowders are extremely costly, as they cannot be produced by simple mechanical milling of inexpensive coarse powders, but instead require synthesis via various complex and expensive chemical routes [5]. Furthermore, nanoparticles exhibit pronounced inter-

particle adhesion, forming dense agglomerates that are difficult to disperse through mechanical mixing, thereby impeding the formation of a homogeneous nanopowder blend. This lack of homogeneity often results in structural defects during densification and sintering, including chemical inhomogeneity, grain size non-uniformity, porosity, and crack formation [14]. From this standpoint, when dealing with highly dispersed powders, *in situ* chemical synthesis methods are preferable. These approaches enable the direct formation of the desired ceramic powder composition from precursor reagents, eliminating the drawbacks associated with *ex situ* mechanical mixing of pre-synthesized ceramic powders [1; 14].

Several chemical synthesis methods have been developed for producing submicron and nanopowder compositions of Si<sub>3</sub>N<sub>4</sub>–SiC. These include pyrolysis of silicon-containing polymers, methane pyrolysis followed by coating of Si<sub>3</sub>N<sub>4</sub> particles with highly dispersed carbon, carbothermal reduction of silicon dioxide in the presence of gaseous nitrogen, gas-phase reactions, and plasma-chemical synthesis [14–21]. However, these methods are characterized by high energy consumption due to the need for elevated temperatures and prolonged heat treatment, as well as the use of expensive equipment and reagents. As a result, such techniques remain largely confined to laboratory-scale production of composite powders and have not yet been transferred to industrial-scale manufacturing. Currently, commercial suppliers of ceramic powders continue to produce primarily single-phase powders, and most nanocomposite ceramic powders are still obtained by conventional methods involving the mixing and milling of their constituent single-phase powders [14; 15]. Nevertheless, chemical synthesis methods for composite powders are regarded as advanced and promising, warranting further development and industrial implementation. Once this goal is achieved, high-quality nanocomposite powders will become commercially available, which is expected to have a positive impact on the performance characteristics of the resulting composite ceramics [14; 15].

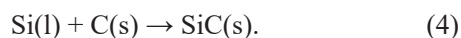
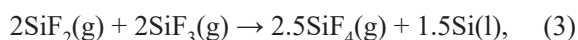
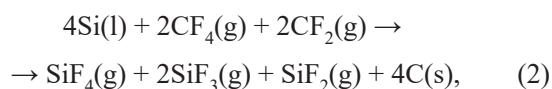
Among the chemical methods used to synthesize submicron and nanoscale Si<sub>3</sub>N<sub>4</sub>–SiC powder compositions, self-propagating high-temperature synthesis (SHS) stands out for its simplicity and energy efficiency. This method is based on the combustion of inexpensive precursor reagents [22–24]. In the simplest case, combustion of a powder mixture of silicon (particle size  $d < 15 \mu\text{m}$ ) and technical carbon ( $d < 1 \mu\text{m}$ ) in gaseous nitrogen at a pressure of 1–7 MPa – that is, in the Si–nC–N<sub>2</sub> system – can be initiated when the carbon black content does not exceed  $n = 0.8$ . The combustion product is a Si<sub>3</sub>N<sub>4</sub>–SiC

powder composition containing 5–60 wt. % SiC, with the remainder comprising silicon nitride predominantly in the  $\beta$ -phase, along with a minor amount of unreacted silicon. Most of the resulting particles are 2–3  $\mu\text{m}$  in size, though larger particles up to 15  $\mu\text{m}$  are also present, typically in the form of columnar crystals or agglomerates of finer particles.

The addition of powdered polytetrafluoroethylene (PTFE)  $(\text{C}_2\text{F}_4)_n$  in small amounts (5–15 wt. %) acts as an activating agent, extending the combustion limits of the Si–C–N<sub>2</sub> system and enabling the synthesis of composites with a wide range of Si<sub>3</sub>N<sub>4</sub>:SiC ratios (from 0 to 100 %). The resulting powders exhibit micron-scale particle sizes and a low fraction of the  $\alpha$ -Si<sub>3</sub>N<sub>4</sub> phase [22]. A more advanced approach involves azide self-propagating high-temperature synthesis (azide SHS), applied to systems based on Si–C–NaN<sub>3</sub>–halide salts. In this method, silicon (Si), technical carbon (C), sodium azide (NaN<sub>3</sub>) as the nitriding agent, and halide salts (NH<sub>4</sub>F, Na<sub>2</sub>SiF<sub>6</sub>, and (NH<sub>4</sub>)<sub>2</sub>SiF<sub>6</sub>) as activating, gasifying additives are used. Combustion of these bulk powder mixtures in a 4.5 L reactor under 4 MPa of nitrogen produces highly dispersed Si<sub>3</sub>N<sub>4</sub>–SiC powder compositions containing 1.6–41.8 wt. % SiC. Compared to earlier combustion-based SHS products, these compositions feature finer particle sizes (mainly in the range of 100–500 nm) and a markedly higher content of the  $\alpha$ -Si<sub>3</sub>N<sub>4</sub> phase – up to ten times greater than that of  $\beta$ -Si<sub>3</sub>N<sub>4</sub> [23–25]. However, the experimental compositions deviated significantly from the theoretical ones, with an excess of silicon nitride, a reduced fraction of silicon carbide, and notable levels of free silicon (up to 5.7 wt. %) and free carbon (up to 5.1 wt. %) as impurities.

It is well known that the synthesis reaction of silicon carbide from elemental silicon and technical carbon powders (Si + C = SiC) is weakly exothermic and cannot proceed in combustion mode under standard conditions [26]. However, the reactivity of the Si + C mixture can be enhanced through preheating, application of an electric field, mechanical activation, chemical activation, or by using a gaseous nitrogen or air environment, enabling the synthesis of SiC via combustion. One of the simplest and most effective approaches involves the use of polytetrafluoroethylene  $(\text{C}_2\text{F}_4)_n$  as a chemical activator. This method enables complete reaction of the mixture  $\text{Si} + 0.9\text{C} + 0.05\text{C}_2\text{F}_4 \rightarrow \text{SiC} + 0.1\text{F}_2$  in a nitrogen atmosphere at 3 MPa, resulting in the formation of SiC particles with an average size of ~200 nm [27]. The reaction stages and structure formation in the combustion wave of Si–C–C<sub>2</sub>F<sub>4</sub> mixtures with relatively high PTFE content (C<sub>2</sub>F<sub>4</sub>:C = 0.5÷3.0) were studied in [28] by burning pressed powder mixtures in an argon atmosphere at 0.5 MPa. The combus-

tion products, in addition to silicon carbide, contained 16–33 % residual silicon (necessary for subsequent Si<sub>3</sub>N<sub>4</sub> formation in Si<sub>3</sub>N<sub>4</sub>–SiC composite synthesis) and consisted of porous agglomerates 10–20  $\mu\text{m}$  in size, incorporating crystallized silicon droplets and SiC grains measuring 0.3–0.7  $\mu\text{m}$ . Furthermore, PTFE can be used not only as an activating additive but also as a carbiding reagent in place of technical carbon during the combustion of a bulk Si + C<sub>2</sub>F<sub>4</sub> mixture in gaseous argon at 0.5 MPa and the synthesis of silicon carbide in the form of fibers (100–500 nm in diameter) and equiaxed particles (0.5–3.0  $\mu\text{m}$ ), which aggregate into porous agglomerates [29]. However, the overall SiC yield in this case is quite low – only about 10 % of the charge reacts to form cotton-like (fluffy) SiC, while the remainder consists of a black powder of unreacted carbon and silicon. This result is attributed to the following sequence of reactions involved in the formation of silicon carbide with PTFE (C<sub>2</sub>F<sub>4</sub>) [28; 29]:



At the first stage (1), PTFE undergoes exothermic decomposition in the preheating zone, producing gaseous fluorides and solid carbon particles. During the intermediate stages (2) and (3), the gaseous fluorides react with each other and with molten silicon. In the final stage (4), silicon and carbon particles – originating both from the initial soot and from PTFE decomposition – react to form the target silicon carbide. Completion of all these stages is essential to obtain highly dispersed SiC; if only the first stage occurs, the result is merely the formation of gaseous fluorides and soot particles [29]. Combustion involving PTFE proceeds at a high rate and is accompanied by intense gas evolution, resulting in the scattering of the charge components. Under these conditions, silicon particles are unlikely to react with carbon particles, as such a reaction is improbable in the gas phase [29]. Therefore, when using PTFE, the charge should be pressed into briquettes – rather than used in bulk form – preferably with a diameter of at least 30 mm, and the combustion should be conducted under elevated gas pressure in an SHS reactor to prevent the escape of PTFE decomposition products from the reaction zone [27–30].

As demonstrated in our previous study [31], this approach proved effective in the azide SHS of another highly dispersed powder composition, AlN–SiC, using PTFE. Partial replacement of carbon in the carbiding mixture with  $0.9C + 0.05C_2F_4$  eliminated, in most cases and across various target AlN/SiC phase ratios, the drawbacks associated with conventional azide SHS using halide salts such as  $(NH_4)_2SiF_6$ ,  $AlF_3$ , and  $NH_4F$ . While maintaining the high dispersity of the synthesized AlN–SiC powder compositions, their phase composition – especially when pressed charges were used – became significantly closer to the intended theoretical composition. The SiC phase content increased substantially, while undesirable secondary phases such as silicon nitride and the water-insoluble salt cryolite ( $Na_3AlF_6$ ) were eliminated.

An attempt to synthesize the target stoichiometric composition of the highly dispersed  $Si_3N_4$ –SiC nitride–carbide system by fully replacing carbon with PTFE in the initial azide SHS reagent mixture was unsuccessful [32]. In bulk mixtures, only small amounts of the desired  $Si_3N_4$  and SiC phases were formed, with free carbon being the predominant combustion product. This result aligns with the findings reported in [29] and is attributed to the combustion proceeding only through the initial stages – specifically, reactions (1) and (2), which involve PTFE decomposition and the generation of gaseous silicon fluorides and free carbon. In pressed mixtures, a substantial fraction of the silicon particles was able to react with carbon (reaction 4), leading to increased formation of the target  $Si_3N_4$  and SiC phases. However, due to continued scattering of the charge components during combustion, a significant portion of the silicon remained unreacted. As a result, the amount of synthesized SiC was considerably lower than the theoretical value predicted by the stoichiometric equations.

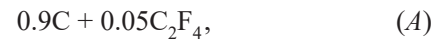
In light of these findings and building upon previous studies [23–25; 32], the present work aimed to increase the SiC content and bring the composition of the highly dispersed  $Si_3N_4$ –SiC material closer to its theoretical target. To this end, we investigated the azide SHS process involving partial substitution of carbon with PTFE in the initial reagent mixture – specifically, the combustion process and resulting products of the Si– $NaN_3$ –C– $C_2F_4$  system.

## Research methodology

To investigate the azide SHS process for synthesizing highly dispersed  $Si_3N_4$ –SiC compositions with partial substitution of carbon by PTFE in the initial charge (reagent mixture), the following starting

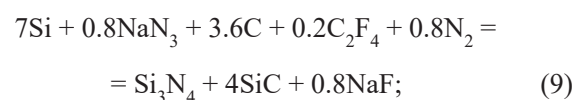
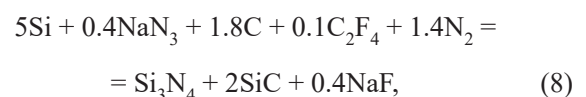
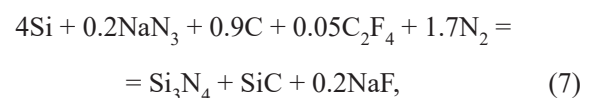
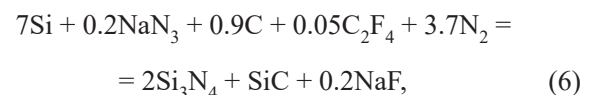
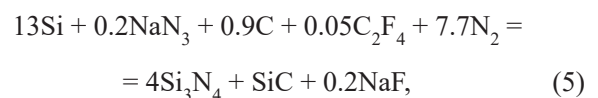
materials were used (wt. % unless otherwise noted): silicon powder, grade Kr00 ( $\geq 99.9\%$ ,  $d = 40\ \mu m$ ); sodium azide powder, analytical grade ( $\geq 98.71\%$ ,  $d = 100\ \mu m$ ); polytetrafluoroethylene (PTFE), grade PN-40 ( $\geq 99.0\%$ ,  $d = 40\ \mu m$ ); and technical carbon black, grade P701 ( $\geq 88.0\%$ ,  $d = 70\ nm$ , in the form of agglomerates up to  $1\ \mu m$ ).

According to [22], achieving a high SiC content in silicon nitride-based composites requires partial replacement of technical carbon with an activating carbiding additive – polytetrafluoroethylene (PTFE) – in amounts of 5, 10, and 15 %. This yields carbiding mixtures of technical carbon and PTFE with the following compositions, each equivalent to 1 mol of carbiding carbon:

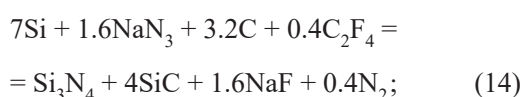
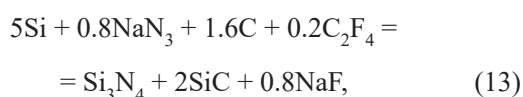
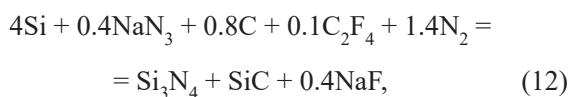
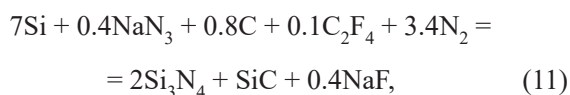
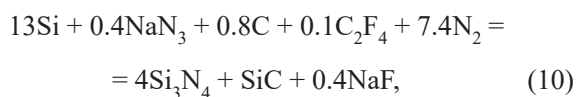


In this azide SHS approach, the strongly nitriding reagent sodium azide ( $NaN_3$ ) is added to the charge in quantities sufficient to neutralize the fluorine released during the complete decomposition of PTFE and bind it as water-soluble sodium fluoride (NaF), which can subsequently be removed from the SHS product by washing with water. As a result, the stoichiometric equations for the azide SHS of  $Si_3N_4$ –SiC powder compositions for five molar ratios of the target phases ( $Si_3N_4:SiC = 4:1, 2:1, 1:1, 1:2, 1:4$ ) using carbiding mixtures (A)–(C) containing PTFE and combusted in a nitrogen atmosphere are as follows:

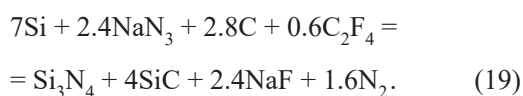
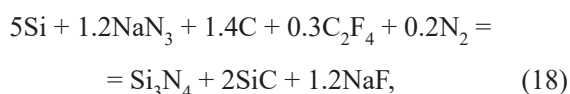
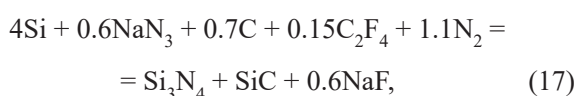
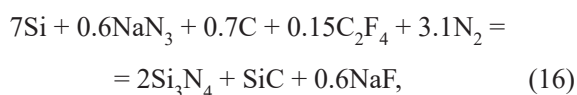
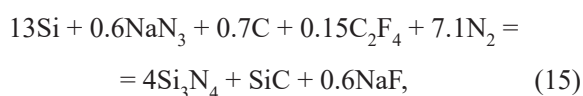
– for carbiding mixture (A):



– for carbiding mixture (B):



– for carbiding mixture (C):

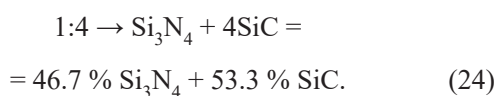
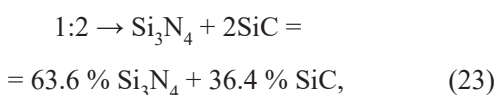
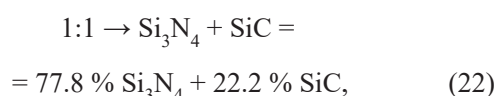
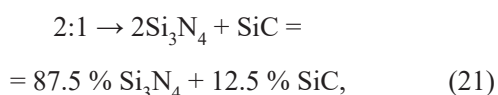
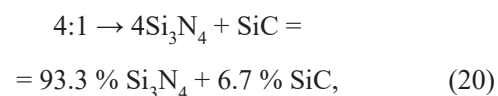


The reagent mixtures corresponding to equations (5)–(19), each with an average mass of 22 g, were combusted in a 4.5 L azide SHS reactor under an initial nitrogen pressure of  $P_0 = 3$  MPa. Combustion was performed in two forms: as a bulk charge, placed in a tracing-paper crucible (30 mm in diameter and 45 mm in height), and as briquetted charges, compacted under 7 MPa into cylindrical pellets measuring 30 mm in diameter and approximately 22 mm in height. Combustion was initiated using a tungsten spiral heater. The maximum gas pressure ( $P_{\max}$ ), generated during combustion was recorded via a manometer. After cooling, the combustion products were removed from the reactor, ground into free-flowing powder using a porcelain mortar, and washed with

water to remove the byproduct – sodium fluoride (NaF). The dried and washed combustion product was weighed, and the mass loss ( $\Delta m$ , %) was determined as the difference between the initial charge mass ( $m_0$ ) and the final product mass ( $m_f$ ). This mass loss was interpreted as deviation of reactants and products caused by intense combustion. The phase composition of the synthesized products was analyzed using an ARL X'TRA powder X-ray diffractometer (Thermo Fisher Scientific, Switzerland) equipped with a copper anode X-ray tube. Diffraction patterns were processed and the quantitative phase composition determined by the Rietveld refinement method using HighScore Plus software and the COD-2024 crystallographic database. The morphology and particle size of the synthesized powders were examined using a JSM-6390A scanning electron microscope (JEOL, Japan).

## Results and discussion

In chemical equations (5)–(19), the composition of the reaction products is expressed in moles, while in the experiments, it is given in weight percent. When converting the molar ratios of silicon nitride to silicon carbide to weight percentages, the following theoretical ratios of the target  $\text{Si}_3\text{N}_4$ –SiC compositions are obtained, assuming complete removal of the water-soluble byproduct sodium fluoride (NaF) from the products of reactions (5)–(19):



The experimentally determined combustion parameters – including the maximum pressure in the reactor ( $P_{\max}$ ) and mass loss ( $\Delta m$ ) – for the initial bulk and pressed powder charges corresponding to reactions (5)–(19), along with the phase compositions of the washed solid reaction products, are summarized in the Table.

**Combustion parameters of the initial powder mixtures (charges) for reactions (5)–(19)  
and theoretical and experimental phase compositions of the washed solid reactions  
for bulk and pressed charges**

**Параметры горения исходных порошковых смесей (шихт) реакций (5)–(19)  
и теоретический и экспериментальный фазовые составы промытых твердых продуктов реакций  
для насыпных и прессованных шихт**

Reaction equation	Si <sub>3</sub> N <sub>4</sub> :SiC (mol)	P <sub>max</sub> , МПа	Δm, %	Phase composition of reaction products, wt. %						
				Theoretical		Experimental				
				Si <sub>3</sub> N <sub>4</sub>	SiC	α-Si <sub>3</sub> N <sub>4</sub>	β-Si <sub>3</sub> N <sub>4</sub>	SiC	Si	C
Bulk charges										
(5)	4:1			No combustion						
(6)	2:1			No combustion						
(7)	1:1			No combustion						
(8)	1:2			No combustion						
(9)	1:4	3.19	38.9	46.7	53.3	–	–	–	56.0	44.0
(10)	4:1			No combustion						
(11)	2:1	3.00	83.8	87.5	12.5	30.0	59.0	8.0	–	–
(12)	1:1	3.70	46.3	77.8	22.2	18.0	56.0	23.0	3.0	–
(13)	1:2	4.02	19.4	63.6	36.4	19.0	52.0	27.0	2.0	–
(14)	1:4	4.02	30.6	46.7	53.3	22.0	24.0	52.0	2.0	–
(15)	4:1	3.50	58.2	93.3	6.7	40.1	50.7	5.2	4.0	–
(16)	2:1	3.19	57.0	87.5	12.5	35.0	51.4	9.6	4.0	–
(17)	1:1	3.89	74.6	77.8	22.2	23.3	53.6	20.5	2.6	–
(18)	1:2	4.23	80.1	63.6	36.4	20.9	44.8	30.6	3.7	–
(19)	1:4	4.13	81.4	46.7	53.3	20.9	29.1	49.0	1.0	–
Pressed charges										
(5)	4:1			No combustion						
(6)	2:1			No combustion						
(7)	1:1			No combustion						
(8)	1:2	3.00	15.0	63.6	36.4	58.0	–	35.0	7.0	–
(9)	1:4	3.29	9.9	46.7	53.3	33.0	26.0	37.0	4.0	–
(10)	4:1			No combustion						
(11)	2:1	3.29	56.9	87.5	12.5	34.2	60.4	5.4	–	–
(12)	1:1	3.45	17.2	77.8	22.2	29.0	49.0	16.0	–	6.0
(13)	1:2	3.96	32.4	63.6	36.4	25.0	44.0	31.0	–	–
(14)	1:4	3.78	27.1	46.7	53.3	22.1	37.6	40.3	–	–
(15)	4:1	3.54	17.5	93.3	6.7	43.6	49.1	6.3	1.0	–
(16)	2:1	3.78	18.6	87.5	12.5	30.2	59.5	10.3	–	–
(17)	1:1	4.01	12.6	77.8	22.2	27.9	48.5	21.6	2.0	–
(18)	1:2	4.04	35.3	63.6	36.4	23.0	45.0	32.0	1.0	–
(19)	1:4	4.36	80.4	46.7	53.3	23.6	27.9	48.5	–	–

The Table shows that the bulk charges corresponding to reactions (5)–(8) did not combust, while combustion of the charge from equation (9) did not yield the target phases Si<sub>3</sub>N<sub>4</sub> and SiC. Instead, the combustion products were merely a mixture of free silicon and carbon. These results can be explained by the fact that

reactions (5)–(9) used carbiding mixture (A), which contains the lowest amount of the activating additive – polytetrafluoroethylene (0.05C<sub>2</sub>F<sub>4</sub> per 1 mole of carbiding carbon). At the same time, these charges included a relatively large amount of poorly reactive silicon powder – ranging from 4 to 13 moles. Only

the charge in equation (9), which had the highest PTFE content ( $0.2C_2F_4$ ), was able to sustain combustion. However, under bulk conditions, this reaction yielded only a mixture of Si and C particles, consistent with the findings reported in [29]. This outcome is attributed to the progression of only reaction (1) – the exothermic decomposition of PTFE – as the first stage of the process. The table also shows that the pressed charges from equations (5)–(7), which also used  $0.05C_2F_4$  as the activating additive, did not combust. Meanwhile, the charges from equations (8) and (9), containing  $0.1C_2F_4$  and  $0.2C_2F_4$  respectively, did combust, but the resulting phase composition deviated significantly from the theoretical one. The products contained considerable amounts of free silicon and less SiC than expected. The recorded maximum gas pressures in the reactor –  $P_{max} = 3.00$  and  $3.29$  MPa – were either equal to or only slightly higher than the initial pressure  $P_0 = 3.00$  MPa. The relatively small mass losses during combustion ( $\Delta m = 15.0$  and  $9.9\%$ ) also point to the low combustion intensity of charges using carbiding mixture (A). (The observed match between the maximum gas pressure and the initial pressure –  $P_{max} = P_0 = 3.00$  MPa – can be by the concurrent increase in nitrogen gas pressure in the reactor due to the combustion-induced temperature rise and the simultaneous decrease in the amount of gaseous nitrogen caused by its significant uptake during the formation of silicon nitride).

It is worth noting that in a similar case of synthesizing a different composition – AlN–SiC – via azide-assisted SHS with the use of PTFE, all bulk and pressed charges based on carbiding mixture (A) underwent combustion, and did so intensively, reaching maxi-

imum reactor pressures ranging from 3.51 to 4.38 MPa. These conditions yielded good results in the formation of the target phases AlN and SiC [31]. This outcome is explained by the fact that, in the charges intended for AlN–SiC synthesis, the  $0.05C_2F_4$  PTFE additive was combined with only 1 mol of poorly reactive Si powder and 1 to 4 mol of highly reactive Al powder.

The Table shows that when using carbiding mixture (B), which contains an increased amount of the activating PTFE additive –  $0.1C_2F_4$  per 1 mol of carbiding carbon – in the charges for reactions (10)–(14), only the charges for reaction (10) fail to combust, both in bulk and pressed form. This is due to the presence of the highest amount (13 mol) of poorly reactive silicon powder in these mixtures. In reactions (11)–(14), the silicon content decreases to 4–7 mol, and the corresponding charges undergo combustion. The combustion of bulk mixtures is more intense, characterized by a somewhat higher pressure rise and greater mass loss. In some  $Si_3N_4$ :SiC molar ratios, the phase composition of the target products from bulk charges more closely approximates the theoretical composition than that of the pressed charges, although up to 3 % of free silicon impurity is still present.

Finally, the Table shows that when using carbiding mixture (C), which contains the highest amount ( $0.15C_2F_4$ ) of the activating PTFE additive per 1 mol of carbiding carbon for reactions (15)–(19), all the corresponding charges undergo intense combustion in both bulk and pressed form, reaching similar maximum reactor pressures ranging from 3.50 to 4.36 MPa. The mass loss strongly depends on the  $Si_3N_4$ :SiC molar ratio. At a 1:4 ratio, the mass loss reaches very high values (up to 80 %) for both bulk and pressed

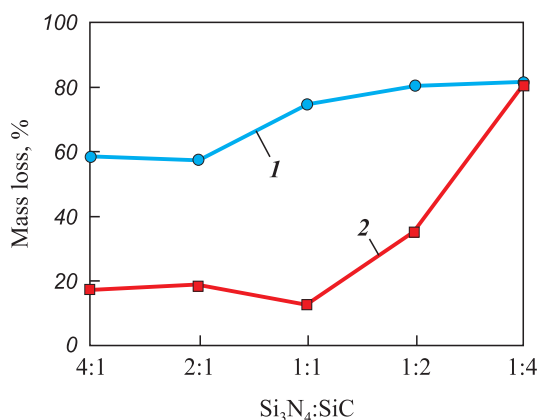


Fig. 1. Mass loss during combustion of bulk (1) and pressed (2) charges synthesized using carbiding mixture (C), as a function of the  $Si_3N_4$ :SiC molar ratio

Рис. 1. Зависимость разброса массы при горении насыпных (1) и прессованных (2) шихт с карбидизирующей смесью (C) от мольного соотношения  $Si_3N_4$ :SiC

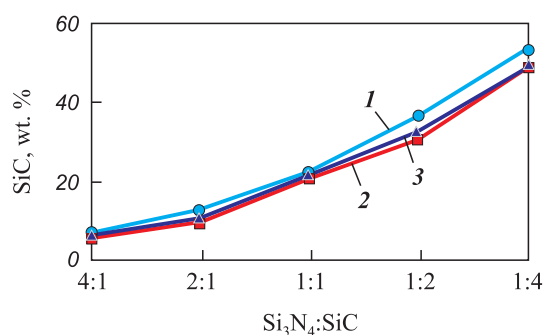


Fig. 2. Relative theoretical (1) and experimental (2, 3) contents of the SiC phase in washed combustion products of bulk (2) and pressed (3) charges synthesized using carbiding mixture (C), as a function of the  $Si_3N_4$ :SiC molar ratio

Рис. 2. Зависимость относительного теоретического (1) и экспериментального (2, 3) содержания фазы SiC в промытых продуктах горения насыпных (2) и прессованных (3) шихт с карбидизирующей смесью (C) от мольного соотношения  $Si_3N_4$ :SiC

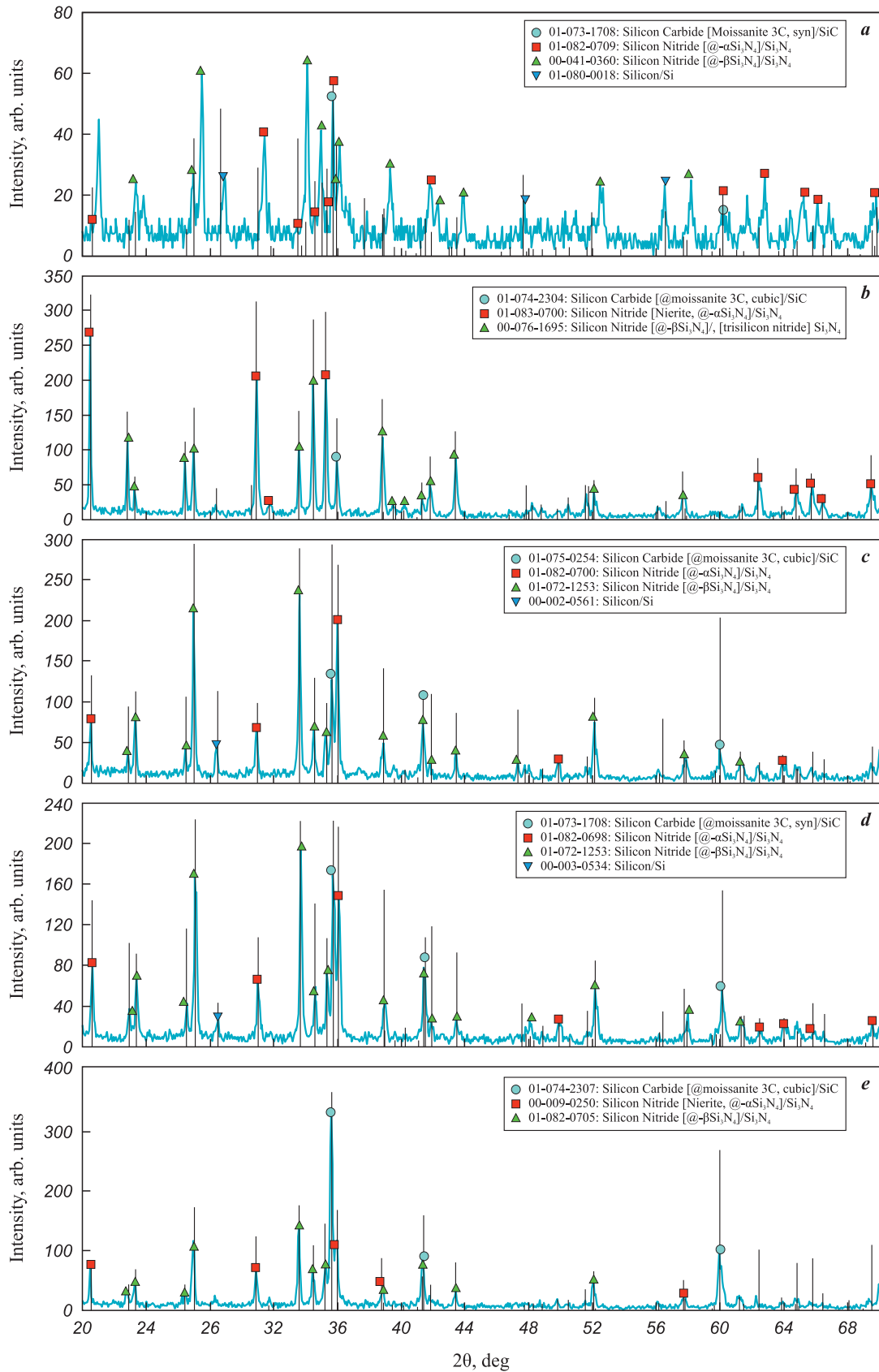


Fig. 3. XRD patterns of combustion products from pressed charges (15)–(19)

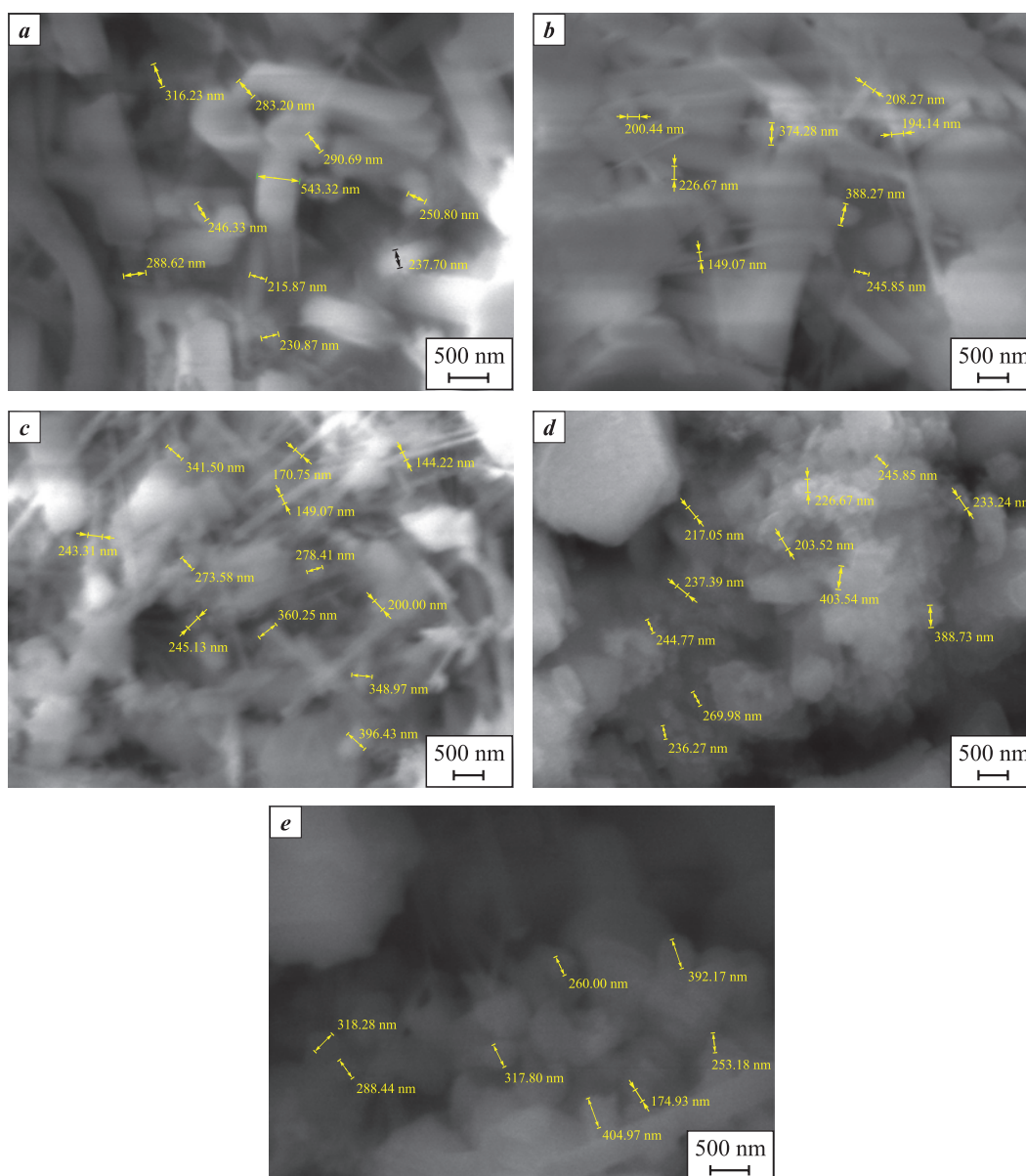
*a* – mixture corresponding to equation (15), *b* – (16), *c* – (17), *d* – (18), *e* – (19)

Рис. 3. Рентгеновские дифрактограммы продуктов горения прессованных шихт (15)–(19)

*a* – шихта из уравнения (15), *b* – (16), *c* – (17), *d* – (18), *e* – (19)

charges. For other  $\text{Si}_3\text{N}_4:\text{SiC}$  ratios, the mass loss remains high for bulk charges (from 57.0 to 80.1 %) but is relatively low for pressed charges (from 12.6 to 35.3 %). The composition of the washed combustion products obtained from the pressed charges is significantly closer to the theoretical values compared to that of the bulk charges, both in terms of  $\text{Si}_3\text{N}_4$  and SiC phase content at all ratios, and in terms of lower levels of free silicon impurity: up to 2.0 % for pressed charges versus up to 4.0 % for bulk charges. The mass loss during combustion and the SiC phase content in the washed products obtained using carbiding mixture (C) are presented graphically in Figs. 1 and 2.

As shown in Fig. 1, the mass loss during combustion of the pressed mixtures is significantly lower than that of the bulk mixtures and becomes nearly identical – and very high – only at the  $\text{Si}_3\text{N}_4:\text{SiC}$  molar ratio of 1:4, reaching 80.4 and 81.4 %, respectively. However, an experiment involving the combustion of this pressed mixture at a higher initial nitrogen pressure in the reactor (increased from 3 to 4 MPa) demonstrated a substantial reduction in mass loss – by a factor of two – to 41.9 %, while maintaining a similar phase composition in the washed combustion product:  $\alpha\text{-Si}_3\text{N}_4 = 42.0$  wt. %,  $\beta\text{-Si}_3\text{N}_4 = 51.0$  wt. %, SiC = 6.0 wt. %, Si = 1.0 wt. %.



**Fig. 4.** Microstructure of the combustion products from pressed charges (15)–(19)  
*a* – mixture corresponding to equation (15), *b* – (16), *c* – (17), *d* – (18), *e* – (19)

**Рис. 4.** Микроструктура продуктов горения прессованных шихт (15)–(19)  
*a* – шихта из уравнения (15), *b* – (16), *c* – (17), *d* – (18), *e* – (19)

As evident from the Table and Fig. 2, the phase composition of the washed combustion products of the pressed charges containing PTFE in carbiding mixture (C) shows the best agreement with the theoretical phase composition in terms of  $\text{Si}_3\text{N}_4$  and SiC content across all investigated  $\text{Si}_3\text{N}_4$ :SiC molar ratios. This experimentally obtained phase composition is much closer to the theoretical composition of  $\text{Si}_3\text{N}_4$ –SiC composites than the results previously reported for conventional azide SHS (without PTFE), which yielded a significantly lower SiC content in the combustion products compared to the theoretical values [23–25].

The X-ray diffraction (XRD) patterns obtained from the washed combustion products of the pressed charges synthesized using carbiding mixture (C) are shown in Fig. 3.

The XRD patterns display strong reflections from the target phases  $\text{Si}_3\text{N}_4$  and SiC, as well as either weak reflections from residual free Si or none at all. Silicon nitride is present in two polymorphic forms:  $\alpha$ - $\text{Si}_3\text{N}_4$  and  $\beta$ - $\text{Si}_3\text{N}_4$ . As shown in Fig. 3 and the table, the contents of these phases are approximately equal at  $\text{Si}_3\text{N}_4$ :SiC molar ratios of 4:1 and 1:4. At other ratios, however, the  $\alpha$ -phase content is roughly half that of the  $\beta$ -phase. Overall, the  $\alpha$ -phase constitutes a significant fraction – ranging from 30 to 50 % – of the silicon nitride phase in the synthesized  $\text{Si}_3\text{N}_4$ –SiC composites.

The microstructure of the synthesized composites is presented in Fig. 4.

As shown in Fig. 4, the combustion products of all pressed charges are predominantly composed of highly dispersed particles smaller than 1–2  $\mu\text{m}$ . The combustion product of the charge from reaction (15) with a  $\text{Si}_3\text{N}_4$ :SiC molar ratio of 4:1 contains a significant fraction of columnar crystals with a transverse size of approximately 500 nm and a length of up to 2  $\mu\text{m}$ , along with a small amount of finer equiaxed particles and nanofibers with diameters below 100 nm. The combustion product of the charge from reaction (16) with a 2:1 ratio includes a large fraction of coarser columnar crystals, approximately 1  $\mu\text{m}$  in diameter and up to 5  $\mu\text{m}$  in length, as well as equiaxed particles up to 2  $\mu\text{m}$  and a small fraction of nanofibers. The product from reaction (17) with a 1:1 ratio stands out for its large proportion of nanofibers in a mixture with equiaxed particles up to 1  $\mu\text{m}$  in size. The combustion product of reaction (18) with a 1:2 ratio primarily consists of agglomerates of relatively fine equiaxed particles ranging from 100 nm to 0.5  $\mu\text{m}$ . Finally, the combustion product of reaction (19) with a 1:4 ratio mainly contains agglomerates of larger equiaxed particles, ranging from 200 nm to 1  $\mu\text{m}$ .

## Conclusion

The conventional approach of azide-assisted SHS using halide salts such as  $\text{NH}_4\text{F}$ ,  $\text{Na}_2\text{SiF}_6$ , and  $(\text{NH}_4)_2\text{SiF}_6$  as activating gasifying additives previously enabled the synthesis of highly dispersed (<1  $\mu\text{m}$ )  $\text{Si}_3\text{N}_4$ –SiC powder compositions through combustion in a nitrogen atmosphere from mixtures of silicon powder, technical carbon, sodium azide, and a halide salt. These compositions exhibited a high content of the  $\alpha$ -phase of silicon nitride. However, their phase compositions significantly deviated from the theoretical values, showing a much higher content of silicon nitride and a markedly lower content of silicon carbide, along with notable impurities of free silicon (up to 5.7 wt. %) and free carbon (up to 5.1 wt. %) [23–25].

In the present study, polytetrafluoroethylene (PTFE) was used instead of halide salts as both an activating and carbiding additive – partially replacing technical carbon – while sodium azide served as the nitriding additive in an amount sufficient to neutralize the fluorine released during complete PTFE decomposition. This approach facilitated the combustion of silicon–carbon powder mixtures in a nitrogen atmosphere and significantly increased the silicon carbide content in the synthesized  $\text{Si}_3\text{N}_4$ –SiC product, while reducing the amounts of free silicon and carbon impurities. The most favorable results were obtained using carbiding mixture (C), which contained the highest PTFE amount ( $0.15\text{C}_2\text{F}_4 + 0.7\text{C}$ ). This can be attributed to the higher content of poorly reactive silicon powder (4 to 13 mol) in the charges for synthesizing  $\text{Si}_3\text{N}_4$ –SiC compositions compared to, for example, a similar PTFE-based azide SHS process for AlN–SiC compositions. In the latter case, the best results were achieved using carbiding mixture (A) with the lowest PTFE content ( $0.05\text{C}_2\text{F}_4 + 0.9\text{C}$ ) in charges containing only 1 mol of poorly reactive Si powder and 1 to 4 mol of highly reactive Al powder.

Based on the obtained data on mass loss during combustion and on the phase composition of the combustion products, it can be recommended that  $\text{Si}_3\text{N}_4$ –SiC powder compositions be synthesized via combustion of pressed charges in azide SHS with partial replacement of 0.3 mol of carbon by 0.15 mol of PTFE, at an initial nitrogen pressure of 3 MPa (or 4 MPa to reduce mass loss when the  $\text{Si}_3\text{N}_4$ :SiC phase ratio is 1:4). The resulting combustion products are predominantly mixtures of highly dispersed particles smaller than 1–2  $\mu\text{m}$  and contain a substantial fraction (30–50 %) of the  $\alpha$ -phase in the silicon nitride component of the synthesized  $\text{Si}_3\text{N}_4$ –SiC compositions. The phase composition of these products is significantly closer to the calculated theoretical composi-

tion of the target  $\text{Si}_3\text{N}_4$ –SiC system than that achieved using conventional azide SHS without PTFE.

## References / Список литературы

- Li J., Yuan W.J., Deng C.J., Zhu H. X. The effect of Si contents on the reaction-bonded  $\text{Si}_3\text{N}_4$ /SiC composite ceramics. *IOP Conference Series: Materials Science and Engineering*. 2013;47(1):012060. <https://doi.org/10.1088/1757-899X/47/1/012060>
- Chenhong M., Li Y., Jiang P., Yue X. Synthesis mechanism of  $\alpha$ - $\text{Si}_3\text{N}_4$  whiskers via SiO vapor in reaction bonded  $\text{Si}_3\text{N}_4$ –SiC composite. *Journal of Alloys and Compounds*. 2023;938(6):168723. <https://doi.org/10.1016/j.jallcom.2023.168723>
- Karklit A.K., Porinsh N.M., Katorgin G.M., Norkina A.S., Solominskaya I.Yu. Refractory products, materials and raw materials. Moscow: Metallurgiya, 1990. 416 p. (In Russ.).  
 Карклит А.К., Поринш Н.М., Каторгин Г.М., Норкина А.С., Соломинская И.Ю. Огнеупорные изделия, материалы и сырье: Справочник. М.: Metallurgiya, 1990. 416 с.
- Strelov K.K. Theoretical foundations of refractory materials technology. Moscow: Metallurgiya, 1985. 480 p. (In Russ.).  
 Стрелов К.К. Теоретические основы технологии огнеупорных материалов. М.: Metallurgiya, 1985. 480 с.
- Surendranathan A.O. An introduction to ceramics and refractories. 1<sup>st</sup> ed. Boca Raton: CRC Press, Taylor & Francis Group, 2015. 524 p. <https://doi.org/10.1201/b17811>
- Shahrestani S., Ismail M., Kakooei S., Beheshti M. Microstructure, phase compositions and mechanical properties of slip cast sintered SiC/ $\text{Si}_3\text{N}_4$  composites. *Ceramics International*. 2021;47(12):13173–13180. <https://doi.org/10.1016/j.ceramint.2021.01.182>
- Yang H., Li Q., Wang Zh., Sun M., Wu H., Cheng X. Effect of different sintering additives on the microstructure, phase compositions and mechanical properties of  $\text{Si}_3\text{N}_4$ /SiC ceramics. *ES Materials and Manufacturing*. 2022;15:65. <https://doi.org/10.30919/esmm5f487>
- Saleem A., Zhang Yu., Gong H., Majeed M.K. Fluoride doped SiC/ $\text{Si}_3\text{N}_4$  composite as a high thermal conductive material with enhanced mechanical properties. *Ceramics International*. 2019;45(16):21004–21010. <https://doi.org/10.1016/j.ceramint.2019.06.289>
- Khajelakzay M., Bakhshi S.R. Optimization of spark plasma sintering parameters of  $\text{Si}_3\text{N}_4$ –SiC composite using response surface methodology (RSM). *Ceramics International*. 2017;43(9):6815–6821. <https://doi.org/10.1016/j.ceramint.2017.02.099>
- Wang J.-Ch., Dommati H., Hsieh Sh.-J. Review of additive manufacturing methods for high-performance ceramic materials. *The International Journal of Advanced Manufacturing Technology*, 2019;103(1–4):2627–2647. <https://doi.org/10.1007/s00170-019-03669-3>
- Basu B., Balani K. Advanced structural ceramics. Hoboken, New Jersey: John Wiley & Sons, Inc., 2011. 502 p.
- Niihara K. New design concept of structural ceramics-ceramic nanocomposites. *Journal of the Ceramic Society of Japan*. 1991;99(1154):982974–982982. <https://doi.org/10.2109/jcersj.99.974>
- Hirano T., Niihara K. Microstructure and mechanical properties of  $\text{Si}_3\text{N}_4$ /SiC composites. *Materials Letters*. 1995;22(5–6):249–254. [https://doi.org/10.1016/0167-577X\(94\)00255-X](https://doi.org/10.1016/0167-577X(94)00255-X)
- Palmero P. Structural ceramic nanocomposites: A review of properties and powders' synthesis methods. *Nanomaterials*. 2015;5(2):656–696. <https://doi.org/10.3390/nano5020656>
- Montanaro L., Palmero P. Advances in the field of nanostructured ceramic composites. *Ceramics*. 2019;2: 296–297. <https://doi.org/10.3390/ceramics2020024>
- Li X., Lei W., Wei J., Zhang Ya., Shi Z. Synthesis and broadband electromagnetic wave absorption for lightweight porous SiC/ $\text{Si}_3\text{N}_4$  composite nanowires. *Ceramics International*. 2023;49(23):37746–37757. <https://doi.org/10.1016/j.ceramint.2023.09.102>
- Riedel R., Seher M., Becker G. Sintering of amorphous polymer-derived Si, N and C containing composite powders. *Journal of The European Ceramic Society*. 1989;5(2):113–122. [https://doi.org/10.1016/0955-2219\(89\)90018-6](https://doi.org/10.1016/0955-2219(89)90018-6)
- Yanai T., Ishizaki K. Mechanical properties of  $\text{Si}_3\text{N}_4$  ceramics prepared from carbon coated powders. *Journal of the Ceramic Society of Japan*. 1993;101(1175):764–768. <https://doi.org/10.2109/jcersj.101.764>
- Suri J., Shaw L., Zawrah M.F. Tailoring the relative contents of  $\text{Si}_3\text{N}_4$  and SiC through carbothermic reduction and nitridation of silica fume. *International Journal of Applied Ceramic Technology*. 2012;9(2):291–303. <https://doi.org/10.1111/j.1744-7402.2011.00710.x>
- Hojo J., Meada H., Kato A. Preparation of composite particles of SiC– $\text{Si}_3\text{N}_4$  system by vapor reaction method. *Yogyo-Kyokai-Shi*. 1987;95(1):45–49.
- Lee H.J., Eguchi K., Yoshida T.J. Preparation of ultra-fine silicon nitride, and silicon nitride and silicon carbide mixed powders in a hybrid plasma. *Journal of the American Ceramic Society*. 2005;73(11):3356–3362. <https://doi.org/10.1111/j.1151-2916.1990.tb06461.x>
- Khachatryan G.L., Arutyunyan A.B., Kharatyan S.L. Activated combustion of a silicon–carbon mixture in nitrogen and SHS of  $\text{Si}_3\text{N}_4$ –SiC composite ceramic powders and silicon carbide. *Combustion, Explosion, and Shock Waves*. 2006;42(5):543–548. <https://doi.org/10.1007/S10573-006-0086-7>  
 Хачатрян Г.Л., Арутюнян А.Б., Харатян С.Л. Активированное горение смеси кремний–углерод в азоте и СВС композиционных керамических порошков  $\text{Si}_3\text{N}_4$ /SiC и карбида кремния. *Физика горения и взрыва*. 2006;42(5):56–62.
- Amosov A.P., Belova G.S., Titova Yu.V., Maidan D.A. Synthesis of highly dispersed powder ceramic composition  $\text{Si}_3\text{N}_4$ –SiC by combustion of components in the Si–C– $\text{NaN}_3$ – $\text{NH}_4\text{F}$  system. *Russian Journal of Inorganic Chemistry*. 2022;67(2):123–130. <https://doi.org/10.1134/S0036023622020024>

- Амосов А.П., Белова Г.С., Титова Ю.В., Майдан Д.А. Синтез высокодисперсной порошковой керамической композиции  $\text{Si}_3\text{N}_4\text{-SiC}$  при горении компонентов в системе  $\text{Si-C-NaN}_3\text{-NH}_4\text{F}$ . *Журнал неорганической химии*. 2022;67(2):1–9.  
<https://doi.org/10.31857/S0044457X22020027>
24. Amosov A.P., Titova Yu.V., Belova G.S., Maidan D.A., Minekhanova A.F. SHS of highly dispersed powder compositions of nitrides with silicon carbide. Review. *Powder Metallurgy and Functional Coatings*. 2022;16(4):34–57.  
<https://doi.org/10.17073/1997-308X-2022-4-34-57>
- Амосов А.П., Титова Ю.В., Белова Г.С., Майдан Д.А., Минеханова А.Ф. СВС высокодисперсных порошковых композиций нитридов с карбидом кремния: Обзор. *Известия вузов. Порошковая металлургия и функциональные покрытия*. 2022;16(4):34–57.  
<https://doi.org/10.17073/1997-308X-2022-4-34-57>
25. Belova G.S. Self-propagating high-temperature synthesis of ceramic nitride-carbide highly dispersed powder compositions  $\text{Si}_3\text{N}_4\text{-SiC}$ ,  $\text{AlN-SiC}$  and  $\text{TiN-SiC}$  using sodium azide and halide salts: Diss. Cand. Sci. (Eng.). Samara: SamSTU, 2022. 209 p. (In Russ.).
- Белова Г.С. Самораспространяющийся высокотемпературный синтез керамических нитридно-карбидных высокодисперсных порошковых композиций  $\text{Si}_3\text{N}_4\text{-SiC}$ ,  $\text{AlN-SiC}$  и  $\text{TiN-SiC}$  с применением азидов натрия и галогенидных солей: Дис. ...канд. техн. наук. Самара: СамГТУ, 2022. 209 с.
26. Mukasyan A.S. Combustion synthesis of silicon carbide. In: *Properties and applications of silicon carbide*. Ed. R. Gerhardt. Rijeka, Croatia: InTech, 2011. P. 361–388.
27. Amirkhanyan N., Kirakosyan H., Zakaryan M., Zurnachyan A., Rodriguez M.A., Abovyan L., Aydinyan S. Sintering of silicon carbide obtained by combustion synthesis. *Ceramics International*. 2023;49(15):26129–26134.  
<https://doi.org/10.1016/j.ceramint.2023.04.233>
28. Vorotilo S., Levashov E.A., Potanin A.Yu., Loginov P.A., Shvyndina N.V. Features of synthesizing ceramic composites discretely reinforced by carbon fibers and SiC nanowires formed in situ in the combustion wave. *Russian Journal of Non-Ferrous Metals*. 2020;61(5):559–570.  
<https://doi.org/10.3103/S1067821220050168>
- Воротыло С., Левашов Е.А., Потанин А.Ю., Loginov П.А., Швындина Н.В. Особенности синтеза керамических композитов, дискретно армированных углеродными волокнами и формирующимися в волне горения in situ волокнами карбида кремния. *Известия вузов. Порошковая металлургия и функциональные покрытия*. 2020;(1):41–54.  
<https://doi.org/10.17073/1997-308X-2020-41-54>
29. Zakorzhevsky V.V., Loryan V.E., Akopdzhanyan T.G. Self-propagating high-temperature synthesis of silicon carbide nanofibers. *Russian Journal of Non-Ferrous Metals*. 2020;61(6):675–679.  
<https://doi.org/10.3103/S106782122006022X>
- Закоржевский В.В., Лорян В.Э., Акопджанян Т.Г. Самораспространяющийся высокотемпературный синтез нановолокон карбида кремния. *Известия вузов. Порошковая металлургия и функциональные покрытия*. 2020;(2):14–20.  
<https://doi.org/10.17073/1997-308X-2020-2-14-20>
30. Nersisyan G.A., Nikogosov V.N., Kharatyan S.L., Merzhanov A.G. Chemical transformation mechanism and combustion regimes in the system silicon-carbon-fluoroplastic. *Combustion, Explosion, and Shock Waves*. 1991;27(6):720–724.  
<https://doi.org/10.1007/BF00814517>
- Нерсисян Г.А., Никогосов В.Н., Харатян С.Л., Мерзханов А.Г. Химический механизм превращения и режимы горения в системе кремний–углерод–фторопласт. *Физика горения и взрыва*. 1991;27(6):77–81.
31. Amosov A.P., Titova Yu.V., Uvarova I.A., Belova G.S. Azide self-propagating high-temperature synthesis of a highly dispersed  $\text{AlN-SiC}$  powder composition using polytetrafluoroethylene. *Powder Metallurgy and Functional Coatings*. 2024; 18(6):28–43.  
<https://doi.org/10.17073/1997-308X-2024-6-28-43>
- Амосов А.П., Титова Ю.В., Уварова И.А., Белова Г.С. Азидный самораспространяющийся высокотемпературный синтез высокодисперсной порошковой композиции  $\text{AlN-SiC}$  с применением политетрафторэтилена. *Известия вузов. Порошковая металлургия и функциональные покрытия*. 2024;18(6):28–43.  
<https://doi.org/10.17073/1997-308X-2024-6-28-43>
32. Titova Yu.V., Uvarova I.A., Amosov A.P., Belova G.S., Maidan D.A. Preparation of  $\text{Si}_3\text{N}_4\text{-SiC}$  powder composition using SHS azide technology using polytetrafluoroethylene. In: *Proceedings of 9<sup>th</sup> International Congress on Energy Fluxes and Radiation Effects (EFRE-2024)* (Tomsk, Russia, 16–21 September 2024). Tomsk: TPU Publishing House, 2024. P. 1489–1494. (In Russ.).  
<https://doi.org/10.56761/EFRE2024.N2-O-031103>
- Титова Ю.В., Уварова И.А., Амосов А.П., Белова Г.С., Майдан Д.А. Получение порошковой композиции  $\text{Si}_3\text{N}_4\text{-SiC}$  по азидной технологии СВС с применением политетрафторэтилена. В сб.: *Proceedings of 9<sup>th</sup> International Congress on Energy Fluxes and Radiation Effects (EFRE-2024)* (Томск, 16–21 сентября 2024 г.). Томск: Изд-во ТПУ, 2024. С. 1489–1494.  
<https://doi.org/10.56761/EFRE2024.N2-O-031103>

### Information about the Authors



**Irina A. Uvarova** – Engineer of the Department of metallurgy, powder metallurgy, nanomaterials (MPMN), Samara State Technical University (SamSTU)

**ORCID:** 0000-0003-3023-3289

**E-mail:** mr.simple2@mail.ru

**Aleksandr P. Amosov** – Dr. Sci. (Phys.-Math.), Prof., Head of the Department of MPMN, SamSTU

**ORCID:** 0000-0003-1994-5672

**E-mail:** egundor@yandex.ru

**Yuliya V. Titova** – Cand. Sci. (Eng.), Associate Prof. of the Department of MPMN, SamSTU

**ORCID:** 0000-0001-6292-280X

**E-mail:** titova600@mail.ru

**Vladislav A. Novikov** – Cand. Sci. (Eng.), Associate Prof. of the Department of MPMN, SamSTU

**ORCID:** 0000-0002-8052-305X

**E-mail:** vladislav\_novyi@mail.ru

### Сведения об авторах

**Ирина Александровна Уварова** – инженер кафедры «Металловедение, порошковая металлургия, наноматериалы» (МПМН) Самарского государственного технического университета (СамГТУ)

**ORCID:** 0000-0003-3023-3289

**E-mail:** mr.simple2@mail.ru

**Александр Петрович Амосов** – д.ф.-м.н., профессор, заведующий кафедрой МПМН, СамГТУ

**ORCID:** 0000-0003-1994-5672

**E-mail:** egundor@yandex.ru

**Юлия Владимировна Титова** – к.т.н., доцент кафедры МПМН, СамГТУ

**ORCID:** 0000-0001-6292-280X

**E-mail:** titova600@mail.ru

**Владислав Александрович Новиков** – к.т.н., доцент кафедры МПМН, СамГТУ

**ORCID:** 0000-0002-8052-305X

**E-mail:** vladislav\_novyi@mail.ru

### Contribution of the Authors



**I. A. Uvarova** – conducted combustion-mode synthesis experiments on powder compositions; prepared and formatted experimental results; participated in the analysis and discussion of the findings; contributed to writing the manuscript.

**A. P. Amosov** – defined the research objective; summarized the obtained results; wrote and edited the manuscript.

**Yu. V. Titova** – formulated the research tasks; planned the experiments; analyzed and discussed the results; contributed to writing the manuscript.

**V. A. Novikov** – performed SEM and XRD analyses of the synthesized powder compositions; participated in the analysis and discussion of the results.

### Вклад авторов

**И. А. Уварова** – проведение экспериментов по синтезу порошковых композиций в режиме горения, подготовка и оформление результатов экспериментов, участие в анализе и обсуждении результатов, участие в написании статьи.

**А. П. Амосов** – определение цели работы, обобщение полученных результатов, написание и редактирование текста статьи.

**Ю. В. Титова** – постановка задач исследований, планирование экспериментов, анализ и обсуждение результатов, участие в написании статьи.

**В. А. Новиков** – проведение СЭМ- и РФА-исследований синтезированных порошковых композиций, участие в анализе и обсуждении результатов.

Received 19.03.2025

Revised 20.03.2025

Accepted 21.03.2025

Статья поступила 19.03.2025 г.

Доработана 20.03.2025 г.

Принята к публикации 21.03.2025 г.



UDC 541.16

<https://doi.org/10.17073/1997-308X-2025-3-39-47>Research article  
Научная статья

# Effect of magnesium oxide on the microstructure and mechanical properties of yttria-stabilized zirconia-based ceramics

E. D. Kuzmenko , S. V. Matrenin, A. R. NassyrbayevNational Research Tomsk Polytechnic University  
30 Lenin Prosp., Tomsk 634050, Russia [kuzmenko70egor@yandex.ru](mailto:kuzmenko70egor@yandex.ru)

**Abstract.** In the present work, sintering and investigation of composite ceramic materials based on nanostructured MgO–ZrO<sub>2</sub> powders were carried out. Zirconium dioxide was additionally stabilized with 3 mol. % yttrium oxide. The nanopowders were pre-treated by mechanical activation using a planetary ball mill at a rotation frequency of 10 Hz. Zirconium dioxide balls were used as the grinding media. The prepared powders were compacted at pressing pressures of 50, 100, 200, and 300 MPa. The compacts were sintered in a high-temperature furnace at 1700 °C. Microstructural studies were performed on the polished surfaces of the sintered samples using scanning electron microscopy (SEM). EDX mapping was conducted to determine the elemental distribution, confirming the presence of two phases in all samples. To evaluate the effectiveness of stabilizing additives on the polymorphic transformation of zirconium dioxide, X-ray diffraction (XRD) analysis was performed. The porosity of the materials and its dependence on the pressing pressure and magnesium oxide content were also assessed. Mechanical properties such as Martens hardness and elastic modulus were measured using a NanoIndenter G200, while flexural strength was evaluated by scratch testing on the same device. Fracture toughness was determined by the indentation method using the Marshall–Evans approach. The influence of magnesium oxide additives on the physical and mechanical properties of the MgO–ZrO<sub>2</sub> composite ceramics was established.

**Keywords:** zirconium dioxide, magnesium oxide, nanostructured powders, activated sintering, ceramics, nanoindentation, EDX mapping

**Acknowledgements:** The research was carried out using the facilities of the Shared Research Center “Nanomaterials and Nanotechnologies” of Tomsk Polytechnic University with support from the Ministry of Science and Higher Education of the Russian Federation, Project No. 075-15-2021-710.

**For citation:** Kuzmenko E.D., Matrenin S.V., Nassyrbayev A.R. Effect of magnesium oxide on the microstructure and mechanical properties of yttria-stabilized zirconia-based ceramics. *Powder Metallurgy and Functional Coatings*. 2025;19(3):39–47. <https://doi.org/10.17073/1997-308X-2025-3-39-47>

# Влияние оксида магния на микроструктуру и механические свойства керамики на основе диоксида циркония, стабилизированного оксидом иттрия

Е. Д. Кузьменко , С. В. Матренин, А. Р. Насырбаев

Национальный исследовательский Томский политехнический университет  
Россия, 634050, г. Томск, пр-т Ленина, 30

 kuzmenko70egor@yandex.ru

**Аннотация.** Проведены спекание и исследование композиционных керамических материалов на основе наноструктурированных порошков  $\text{MgO-ZrO}_2$ . Диоксид циркония был дополнительно стабилизирован 3 мол. % оксидом иттрия. Применяемые нанопорошки предварительно обрабатывались методом механоактивации с помощью планетарной шаровой мельницы при частоте вращения размольных сосудов 10 Гц. В качестве мелющих тел использованы шары из диоксида циркония. Подготовленные порошки были спрессованы при давлении прессования 50, 100, 200 и 300 МПа. Полученные прессовки спекались в высокотемпературной печи при температуре 1700 °С. На подготовленной полированной поверхности спеченных образцов проведены микроструктурные исследования методом растровой электронной микроскопии. Выполнено EDX-картирование для выявления распределения элементов, установлено наличие двух фаз во всех изученных образцах. Для оценки эффективности влияния стабилизирующих добавок на полиморфное превращение диоксида циркония осуществлен рентгенофазовый анализ. В ходе исследования определены пористость материалов и ее зависимость от давления прессования и содержания оксида магния. При проведении индентирования на приборе «NanoIndenter G200» изучены механические свойства образцов – твердость по Мартенсу и модуль упругости, а в ходе Scratch-тестирования на данном оборудовании – их предел прочности на изгиб. По методу индентирования с использованием зависимости Маршала–Эванса определена трещиностойкость образцов. В ходе исследования установлено влияние добавок оксида магния на физико-механические свойства композитной керамики  $\text{MgO-ZrO}_2$ .

**Ключевые слова:** диоксид циркония, оксид магния, наноструктурированные порошки, активированное спекание, керамика, наноиндентирование, EDX-картирование

**Благодарности:** Исследование выполнено с использованием оборудования Центра коллективного пользования Научно-образовательного центра «Наноматериалы и нанотехнологии» Томского политехнического университета при поддержке проекта Минобрнауки России № 075-15-2021-710.

**Для цитирования:** Кузьменко Е.Д., Матренин С.В., Насырбаев А.Р. Влияние оксида магния на микроструктуру и механические свойства керамики на основе диоксида циркония, стабилизированного оксидом иттрия. *Известия вузов. Порошковая металлургия и функциональные покрытия.* 2025;19(3):39–47. <https://doi.org/10.17073/1997-308X-2025-3-39-47>

## Introduction

Zirconium dioxide-based ceramics have found wide application in various fields of science and technology due to their outstanding properties. This material exhibits high fracture toughness [1], low coefficient of friction [2], and significant wear resistance and strength [3]. For this reason, zirconium dioxide-based ceramic materials are widely used in dentistry [4], as well as in the production of hip joint head implants, cutting tools, bearing rolling elements, heat-resistant components, and many other applications.

However, due to the phase transformation of zirconium dioxide into the monoclinic phase and the associated volumetric changes, a number of limitations arise in the manufacturing of components from this material [5]. In particular, the introduction of stabilizing

additives is required – most commonly yttrium, calcium, or cerium oxides. The addition of stabilizers makes it possible to prevent the phase transformation by forming a substitutional solid solution based on zirconium dioxide and the introduced additive. The ionic radius of the substituting elements is close to that of ( $\text{Zr}^{4+}$ ), but slightly larger [6].

The prevention of the phase transformation can also be achieved by other means, in cases where the components do not form solid solutions. One such method is the stabilization by creating a composite material based on  $\text{Al}_2\text{O}_3\text{-ZrO}_2$ . Due to the high elastic modulus of aluminum oxide and its lower thermal expansion, sintering results in a rigid matrix in which zirconium dioxide particles are uniformly distributed and subjected to a compressive stress field. As a result, zirconium dioxide does not undergo polymorphic transfor-

mation, and the composite structure enables improved mechanical properties [7]. Magnesium oxide, silicon nitride, and other high-modulus inclusions can also serve as the matrix material [8].

Zirconium dioxide stabilization can be achieved by the combined effect of several factors. However, complex oxide systems consisting of three or more ceramic oxide components have not yet been sufficiently studied. For example, in [9], the effect of small additions (up to 2 wt. %) of MgO on ZTA–CeO<sub>2</sub> ceramics was evaluated. It was found that the relationship between the additive and the resulting mechanical properties is nonlinear, with optimal values observed at 0.5 wt. % MgO. This was explained by the formation of two new phases – MgAl<sub>11</sub>CeO<sub>19</sub> and MgAl<sub>2</sub>O<sub>4</sub>. In [10], it was noted that increasing the magnesium oxide content up to 8 mol. % enhances fracture toughness while reducing hardness. In [11], the addition of yttrium oxide to Mg–PSZ ceramics resulted in a noticeable increase in hardness with only a slight decrease in fracture toughness. These studies indicate significant potential for developing composite ceramics based on zirconium dioxide with magnesium and yttrium oxide additives.

The objective of this study was to determine the effect of magnesium oxide content on the microstructure and mechanical properties of ceramics in a complex oxide system: MgO–ZrO<sub>2</sub>–Y<sub>2</sub>O<sub>3</sub>.

## Materials and methods

In this study, nanostructured zirconium dioxide powders of grade UDPO VTU 4-25-90 produced by plasma chemical synthesis (with an average particle size of 500 nm) and industrial-grade micron-sized magnesium oxide powders of grade MRTU 6-09-3391-67 (particle size <40 μm) were used. The purity of both powders was 99 %.

A 3 mol. % yttrium oxide additive was introduced into the zirconium dioxide powder. Based on these powders, mixtures with the following compositions (mol. %) were prepared: 2MgO–98ZrO<sub>2</sub>;

4MgO–96ZrO<sub>2</sub>; 8MgO–92ZrO<sub>2</sub>; 16MgO–84ZrO<sub>2</sub>. The compositions of these mixtures in molar and mass percentages are presented in Table.

The powders under investigation were pre-treated by mechanical activation. Mechanical activation was carried out in an Activator-2SL planetary ball mill (Activator Machine-Building Plant, Novosibirsk, Russia) under the following conditions: grinding vessel rotation frequency – 10 Hz, treatment time – 10 min, and a grinding media to powder mass ratio of 3:1. Zirconium dioxide balls were used as grinding media.

The prepared powder mixtures were compacted using carboxymethyl cellulose as a plasticizer at uniaxial pressing pressures of 50, 100, 200, and 300 MPa. The green compacts were then sintered in a high-temperature furnace at 1700 °C with a 1 h dwell time at the target temperature. The densities of the sintered samples were determined using the hydrostatic weighing method. Since the formation of a composite structure with possible new solid solutions complicates the determination of theoretical density, porosity was evaluated based on micrographs of the sample surfaces obtained by scanning electron microscopy (SEM) at low magnification (200×), following the procedure described in [12; 13].

SEM investigations of the sample surfaces and elemental analysis (EDX mapping) were carried out using a Zeiss EVO 50 scanning electron microscope (Carl Zeiss, Germany).

The phase composition of the materials was studied by X-ray diffraction (XRD) using a Shimadzu XRD-7000 diffractometer (Japan) with CuK<sub>α1</sub> radiation (λ = 1.5406 Å) and step scanning in the 2θ range of 10–90°. Diffraction peak identification was performed using the Crystallographica Search-Match software and the PDF4+ structural database. The structural analysis was conducted using the PowderCell 2.4 program and the same database.

The mechanical properties of the sintered samples were evaluated using a NanoIndenter G200 (KLA-Tencor, USA) equipped with a Berkovich diamond tip under a 500 mN load. Martens hardness and elastic modulus were determined from the loading curves. Scratch testing was used to determine the flexural strength of the samples under indentation. This method involves scratching the sample surface under a linearly increasing load up to 10 mN, followed by measurement of the crack depth and width. The nanoindentation procedure is described in detail in [14; 15]. Fracture toughness was determined using a Vickers microhardness tester PMT-3 (LOMO JSC, St. Petersburg, Russia) by the indentation method [16]. Cracks were induced under a 5 N load.

### Composition of powder mixtures

#### Соотношение компонентов в порошковых смесях

Mixture composition	
mol. %	wt. %
2MgO–98ZrO <sub>2</sub>	0.65MgO–99.35ZrO <sub>2</sub>
4MgO–96ZrO <sub>2</sub>	1.33MgO–98.67ZrO <sub>2</sub>
8MgO–92ZrO <sub>2</sub>	2.75MgO–97.25ZrO <sub>2</sub>
16MgO–84ZrO <sub>2</sub>	5.83MgO–94.17ZrO <sub>2</sub>

## Results and discussion

After sintering under the specified conditions, high-density samples were obtained (Fig. 1). Among the studied compositions, the samples with 8MgO–92ZrO<sub>2</sub> exhibited the highest density. It was found that the dependence of the relative density of MgO–ZrO<sub>2</sub> composite ceramics on composition is nonlinear. At all investigated compaction pressures, the relative densities of the sintered samples decreased in the following order (mol. %): 8MgO–92ZrO<sub>2</sub>, 4MgO–96ZrO<sub>2</sub>, 16MgO–84ZrO<sub>2</sub>, 2MgO–98ZrO<sub>2</sub>, which is consistent with the findings reported in [17; 18]. It was shown in [17] that increasing the sintering time for the 8MgO–92ZrO<sub>2</sub> ceramic composition leads to a further increase in density, continuing up to 20 h of treatment. In [18], it was noted that the porosity of MgO–ZrO<sub>2</sub>-based composites varies depending on the presence of magnesium oxide; however, this

dependence differs across temperature ranges, exhibiting both an increase and a decrease in material porosity. Moreover, a linear trend was observed only within specific temperature intervals. The study in [18] was conducted at higher temperatures than the present work and reported elevated porosity levels in the range of 24 to 32 %. These findings highlight the effectiveness of the mechanical activation parameters applied in this study and suggest its further use when working with materials of this composition.

Using EDX mapping to determine the elemental composition of ceramic samples compacted at a pressure of 300 MPa, images of the polished cross-sectional surfaces were obtained. Fig. 2 shows the elemental distribution and microstructure images for the 2MgO–98ZrO<sub>2</sub> composition.

Based on the results of EDX mapping of MgO–ZrO<sub>2</sub>-based samples, the presence of two distinct phases –

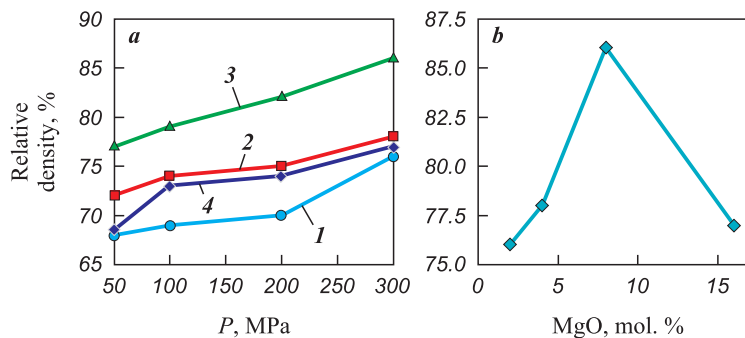


Fig. 1. Dependence of the relative density of sintered samples on pressing pressure (a) and on magnesium oxide content for samples compacted at  $P = 300$  MPa (b)  
Samples, mol. %: 1 – 2MgO–98ZrO<sub>2</sub>, 2 – 4MgO–96ZrO<sub>2</sub>, 3 – 8MgO–92ZrO<sub>2</sub>, 4 – 16MgO–84ZrO<sub>2</sub>

Рис. 1. Зависимость относительной плотности спеченных образцов от давления прессования (a) и содержания оксида магния для образцов, полученных при  $P = 300$  МПа (b)  
Образцы, мол. %: 1 – 2MgO–98ZrO<sub>2</sub>, 2 – 4MgO–96ZrO<sub>2</sub>, 3 – 8MgO–92ZrO<sub>2</sub>, 4 – 16MgO–84ZrO<sub>2</sub>

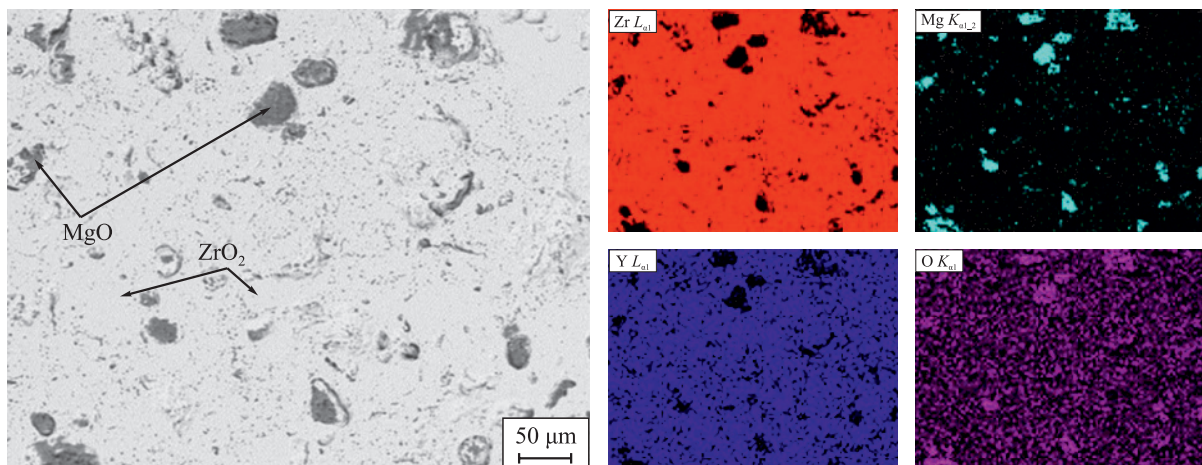
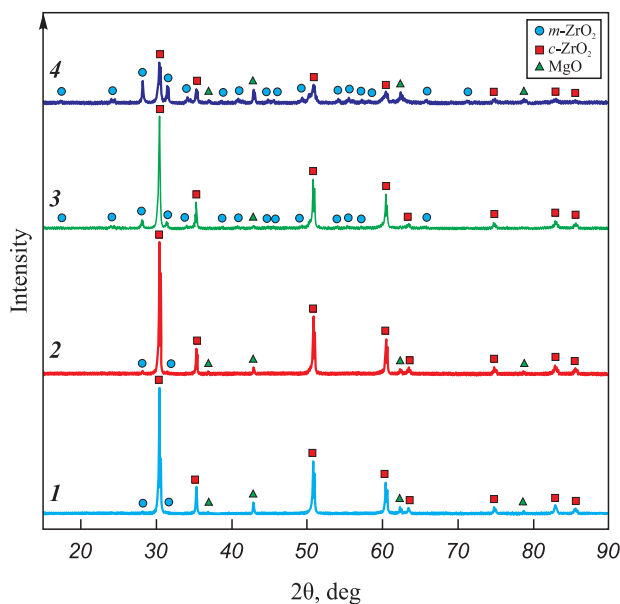


Fig. 2. Elemental analysis of a sintered sample with the composition 2MgO–98ZrO<sub>2</sub>

Рис. 2. Элементный анализ спеченного образца состава 2MgO–98ZrO<sub>2</sub>

MgO and ZrO<sub>2</sub> – was established, which is consistent with the observations reported in [19]. However, according to [10; 11; 20], the formation of a solid solution based on ZrO<sub>2</sub>–MgO should occur. The two-phase composite structure obtained in this study indicates that no interaction between MgO and ZrO<sub>2</sub> takes place during sintering. According to the EDX mapping results, magnesium does not enter the crystalline structure of ZrO<sub>2</sub> and does not form a solid solution based on ZrO<sub>2</sub>–MgO, which is attributed to the stabilizing effect of Y<sub>2</sub>O<sub>3</sub>.



**Fig. 3.** X-ray diffraction (XRD) analysis  
 Samples, mol. %: 1 – 2MgO–98ZrO<sub>2</sub>, 2 – 4MgO–96ZrO<sub>2</sub>,  
 3 – 8MgO–92ZrO<sub>2</sub>, 4 – 16MgO–84ZrO<sub>2</sub>

**Рис. 3.** Рентгенофазовый анализ  
 Образцы, мол. %: 1 – 2MgO–98ZrO<sub>2</sub>, 2 – 4MgO–96ZrO<sub>2</sub>,  
 3 – 8MgO–92ZrO<sub>2</sub>, 4 – 16MgO–84ZrO<sub>2</sub>

To assess the effect of stabilizing additives, XRD analysis was performed (Fig. 3). It was found that zirconium dioxide in the studied samples exists in both the cubic and monoclinic phases, indicating an incomplete stabilization process of zirconium dioxide [10; 21; 22]. According to [23], increasing the sintering temperature should have a positive effect on the stabilization process, which represents a relevant direction for further research.

Mechanical tests showed that the hardness values of the investigated samples varied over a wide range. The highest Martens hardness (8.65 GPa) was recorded for the ceramic with the composition 16MgO–84ZrO<sub>2</sub>, fabricated under a pressing pressure of 300 MPa. At this pressure, all samples exhibited their maximum hardness. An increase in hardness was generally observed with increasing pressing pressure; however, for the 4MgO–96ZrO<sub>2</sub> composition, values deviating from this positive trend were identified.

For the MgO–ZrO<sub>2</sub> ceramic composite materials, it was found that at a pressing pressure of 50 MPa, the hardness values of the investigated samples were approximately the same across all compositions, around 5 GPa. As the pressing pressure increased, the hardness also increased; however, a distinct contribution of magnesium oxide to the hardness enhancement became apparent only at pressures above 200 MPa. This effect is attributed to the reduced influence of porosity at a pressing pressure of ≥200 MPa, a linearly increasing dependence of hardness on the magnesium oxide content was observed (Fig. 4), which is associated with changes in the crystallochemical structure. A similar trend of increasing hardness with higher MgO content was also reported in [18]. Although the authors of [18] used higher sintering temperatures (from 1570 to 1970 K), our results demonstrate that even at lower

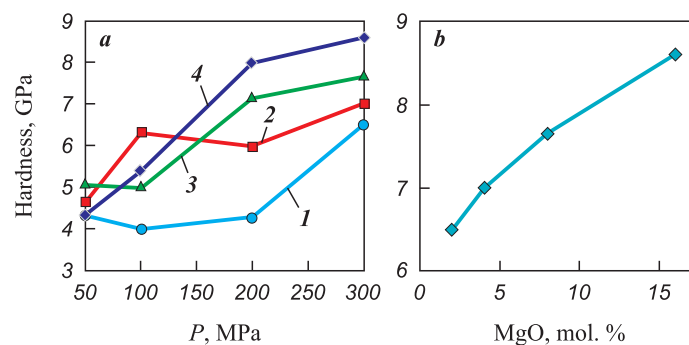


**Fig. 4.** Dependence of Martens hardness of sintered samples on pressing pressure (a) and magnesium oxide content for samples produced at P = 300 MPa (b)  
 Samples, mol. %: 1 – 2MgO–98ZrO<sub>2</sub>, 2 – 4MgO–96ZrO<sub>2</sub>, 3 – 8MgO–92ZrO<sub>2</sub>, 4 – 16MgO–84ZrO<sub>2</sub>

**Рис. 4.** Зависимость твердости по Мартенсу спеченных образцов от давления прессования (a) и от содержания оксида магния для образцов, полученных при P = 300 МПа (b)  
 Образцы, мол. %: 1 – 2MgO–98ZrO<sub>2</sub>, 2 – 4MgO–96ZrO<sub>2</sub>, 3 – 8MgO–92ZrO<sub>2</sub>, 4 – 16MgO–84ZrO<sub>2</sub>

sintering temperatures, magnesium oxide retains its positive effect on material hardness, which highlights the potential of this ceramic composite material for further study at reduced sintering temperatures. At the same time, according to [10; 11], the hardness values of the investigated MgO–ZrO<sub>2</sub>–Y<sub>2</sub>O<sub>3</sub> materials exceed those of MgO–ZrO<sub>2</sub>, Y<sub>2</sub>O<sub>3</sub>–ZrO<sub>2</sub>, and MgO ceramics. For example, the Vickers hardness of MgO–ZrO<sub>2</sub>–Y<sub>2</sub>O<sub>3</sub> ceramics can reach 14.8 GPa, compared to the respective values of 10.9, 12.0–12.5, and 10–11 GPa reported for the above-mentioned materials.

During the study of the elastic modulus of the materials, the highest value – 330.3 GPa – was recorded for the ceramic with the composition 16MgO–84ZrO<sub>2</sub> at a pressing pressure of 300 MPa (Fig. 5). For the MgO–ZrO<sub>2</sub> ceramics, the elastic modulus values deviated from the previously observed trend for hardness. For the 4MgO–96ZrO<sub>2</sub> and 8MgO–92ZrO<sub>2</sub> samples, a nonlinear dependence of the elastic modulus on the applied pressure was observed; however, this property was nearly identical at both the maximum and minimum pressures. Across all applied pressures, the highest elastic modulus was found for the 16MgO–84ZrO<sub>2</sub> composition. At a pressing pressure of 50 MPa, it was observed that the elastic modulus increased with increasing magnesium oxide content. However, with further increases in pressing pressure, this dependence broke down and became nonlinear, no longer associated with porosity levels. It was found that at the highest pressing pressure and maximum material density, the ceramics with compositions 16MgO–84ZrO<sub>2</sub> and 2MgO–98ZrO<sub>2</sub> exhibited the highest elastic moduli, while the compositions 4MgO–96ZrO<sub>2</sub> and 8MgO–92ZrO<sub>2</sub> showed lower values. In other words, a parabolic dependence of the elastic modulus on the magnesium oxide content is formed, with a mini-

mum at 4 mol. % MgO. Study [25] presents the dependence of the elastic modulus on the MgO content in MgO–ZrO<sub>2</sub> composites and shows an increase in modulus up to 20 mol. % MgO. At higher MgO contents, the elastic modulus decreases. However, since the increments of magnesium oxide addition in that study were large (about 20 %), they did not provide sufficient resolution to describe the influence of MgO on the elastic modulus in the 0–20 % range. Therefore, the present study is of particular relevance, as it reveals the behavior of the elastic modulus within this critical composition interval.

In this study, the strength parameters of ceramic samples obtained at a pressing pressure of 300 MPa were determined using the scratch test method, along with the critical stress intensity factors (fracture toughness) (Fig. 6). It was found that the lowest strength (467.17 MPa) was exhibited by the sample with the composition 2MgO–98ZrO<sub>2</sub>. An increase in strength was observed with rising magnesium oxide content, reaching up to 791.15 MPa, with this trend following a hyperbolic pattern. According to [25], the behavior of the strength parameter, similar to that of the elastic modulus, reaches a maximum upon the addition of 20 mol. % MgO, followed by a decline when this content is exceeded, assuming the same fixed intervals of magnesium oxide addition.

In the present study, it was found that the fracture toughness (critical stress intensity factor) varies nonlinearly with increasing magnesium oxide content, reaching a maximum value of 10.53 MPa·m<sup>1/2</sup> with the composition 16 mol. % MgO. Publications [9; 10] report that the introduction of magnesium oxide in various molar fractions increases the fracture toughness of zirconia-based ceramics; however, the dependence is nonlinear. According to [9], the addition of a small

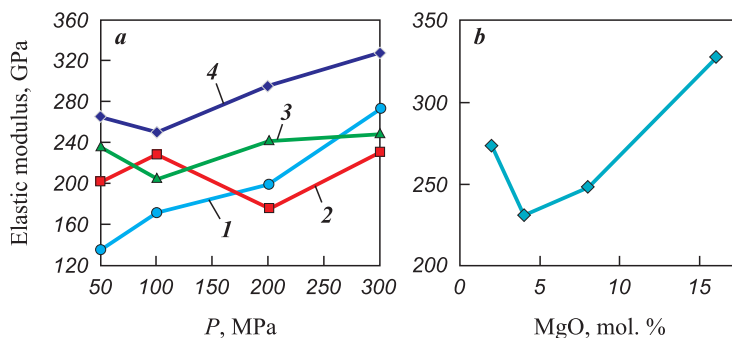


Fig. 5. Dependence of elastic modulus of sintered samples on pressing pressure (a) and magnesium oxide content for samples obtained at  $P = 300$  MPa (b)

Samples, mol. %: 1 – 2MgO–98ZrO<sub>2</sub>, 2 – 4MgO–96ZrO<sub>2</sub>, 3 – 8MgO–92ZrO<sub>2</sub>, 4 – 16MgO–84ZrO<sub>2</sub>

Рис. 5. Зависимость модуля упругости спеченных образцов от давления прессования (a) и от содержания оксида магния для образцов, полученных при  $P = 300$  МПа (b)

Образцы, мол. %: 1 – 2MgO–98ZrO<sub>2</sub>, 2 – 4MgO–96ZrO<sub>2</sub>, 3 – 8MgO–92ZrO<sub>2</sub>, 4 – 16MgO–84ZrO<sub>2</sub>

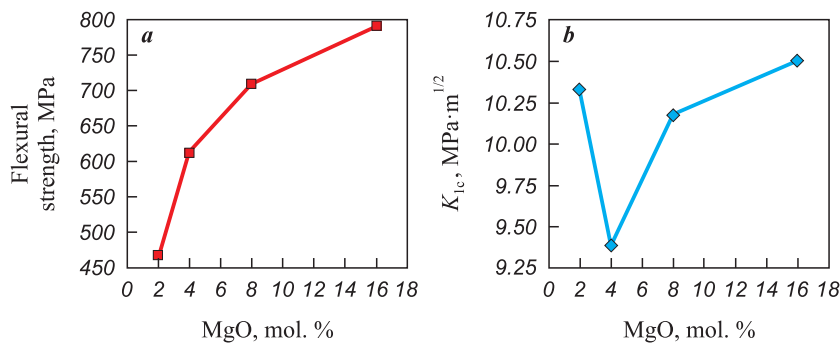


Fig. 6. Dependence of flexural strength (a) and fracture toughness (b) of sintered samples on the magnesium oxide content

Рис. 6. Зависимость предела прочности на изгиб (a) и трещиностойкости (b) спеченных образцов от содержания оксида магния

amount of magnesium oxide – 0.5 mol. % MgO – raises the fracture toughness to 9.14 MPa·m<sup>1/2</sup>. In publication [10], zirconia samples stabilized with 8 mol. % MgO were studied. The authors [10] found that increasing the sintering temperature from 1450 to 1500 °C led to an increase in the critical stress intensity factor from 7.59 to 8.5 MPa·m<sup>1/2</sup>. In the present work, raising the sintering temperature to 1700 °C and introducing an additional stabilizing additive – yttrium oxide – resulted in an increase in fracture toughness to 10.14 MPa·m<sup>1/2</sup> for the sample containing 8 mol. % MgO, which indicates the effectiveness of sintering temperature enhancement for improving this parameter.

## Conclusions

1. The conducted study established that the consolidation of MgO–ZrO<sub>2</sub> ceramic powder mixtures with additional stabilization of zirconium dioxide using yttrium oxide enables the formation of a composite structure. It was shown that magnesium does not enter the crystal structure of ZrO<sub>2</sub> and does not form a ZrO<sub>2</sub>–MgO-based solid solution due to the stabilizing effect of Y<sub>2</sub>O<sub>3</sub>.

2. Mechanical activation of the ceramic batches at a rotation frequency of 10 Hz for 10 min resulted in a reduction in the porosity of the sintered materials compared to previously reported data.

3. It was found that increasing the pressing pressure to 300 MPa has a positive effect on the mechanical properties of the materials.

4. Among the investigated samples, the highest Martens hardness (8.65 GPa) was observed for the ceramic with a composition of 16MgO–84ZrO<sub>2</sub> obtained at a pressing pressure of 300 MPa. An increase in the magnesium oxide content has a positive effect on the hardness of the material; however, a significant

contribution of MgO to the improvement in hardness is observed only at  $P > 200$  MPa, which is associated with a reduced contribution of porosity to the resulting hardness.

5. The sample with a composition of 16MgO–84ZrO<sub>2</sub> obtained at a pressing pressure of 300 MPa exhibited the highest elastic modulus among all tested materials – 330.3 GPa. This composition demonstrated the highest elastic modulus values at all applied pressing pressures. For the samples obtained at  $P = 300$  MPa, a parabolic dependence of the elastic modulus on magnesium oxide content was revealed, with a minimum at 4 mol. % MgO.

6. It was found that increasing the magnesium oxide content leads to higher tensile strength, reaching 791.15 MPa at 16 mol. % MgO.

7. It was shown that the dependence of the critical stress intensity factor on magnesium oxide content is nonlinear, with a maximum value of 10.53 MPa·m<sup>1/2</sup> at 16 mol. % MgO.

## References / Список литературы

1. Soon G., Pingguan-Murphy B., Lai K.W., Akbar S.A. Review of zirconia-based bioceramic: Surface modification and cellular response. *Ceramics International*. 2016; 42(11):12543–12555. <https://doi.org/10.1016/j.ceramint.2016.05.077>
2. Ghaemi M.H., Reichert S., Krupa A., Sawczak M., Zykova A., Lobach K., Svitlychnyi Y. Zirconia ceramics with additions of alumina for advanced tribological and biomedical applications. *Ceramics International*. 2017; 43(13):9746–9752. <https://doi.org/10.1016/j.ceramint.2017.04.150>
3. Smirnov V.V., Smirnov S.V., Obolkina T.O., Antonova O.S., Goldberg M.A., Barinov S.M. Low-temperature liquid-phase sintering of zirconium dioxide: study of phase composition and microstructure. *Reports of the Russian Academy of Sciences. Chemistry, Materials Science*.

- 2020;494(1);37–41. (In Russ.).  
<https://doi.org/10.31857/S268695352005012X>
- Смирнов В.В., Смирнов С.В., Оболкина Т.О., Антонова О.С., Гольдберг М.А., Баринов С.М. Низкотемпературное жидкофазное спекание диоксида циркония: исследование фазового состава и микроструктуры. Доклады Российской академии наук. Химия, науки о материалах. 2020;494(1);37–41.  
<https://doi.org/10.31857/S268695352005012X>
4. Goldberg M.A., Smirnov V.V., Barinov S.M. Creation of new ceramic materials based on zirconium dioxide and aluminum oxide for medical applications. In: *Baikov Institute of Metallurgy and Materials Science of the RAS – 80 years: Collection of scientific articles*. Moscow: Interkontakt Nauka, 2018. P. 286–292. (In Russ.).  
<https://doi.org/10.30791/978-5-902063-58-20286-292>
  - Гольдберг М.А., Смирнов В.В., Баринов С.М. Создание новых керамических материалов на основе диоксида циркония и оксида алюминия для медицинских применений. В сб. науч. тр.: *Институт металлургии и материаловедения им. А.А. Байкова РАН – 80 лет*. М.: Интерконтакт Наука, 2018. С. 286–292.  
<https://doi.org/10.30791/978-5-902063-58-20286-292>
  5. Hannink R.H.J., Kelly P.M., Muddle B.C. Transformation toughening in zirconia-containing ceramics. *Journal of the American Ceramic Society*. 2000; 83(3):461–487.  
<https://doi.org/10.1111/j.1151-2916.2000.tb01221.x>
  6. Casellas D., Cumbreira F.L., Sánchez-Bajo F., Forsling W., Llanes L., Anglada M. On the transformation toughening of Y–ZrO<sub>2</sub> ceramics with mixed Y–TZP/PSZ microstructures. *Journal of the European Ceramic Society*. 2001;21(6):765–777.  
[https://doi.org/10.1016/S0955-2219\(00\)00273-9](https://doi.org/10.1016/S0955-2219(00)00273-9)
  7. Dmitrievskii A.A., Zhigachev A.O., Zhigacheva D.G., Tyurin A.I. Structure and mechanical properties of the CaO–ZrO<sub>2</sub>–Al<sub>2</sub>O<sub>3</sub> ceramic composites at low corundum concentrations. *Technical Physics*. 2019;64(1):81–91.  
<https://doi.org/10.1134/S1063784219010092>
  - Дмитриевский А.А., Жигачев А.О., Жигачева Д.Г., Тюрин А.И. Структура и механические свойства композиционной керамики CaO–ZrO<sub>2</sub>–Al<sub>2</sub>O<sub>3</sub> при малых концентрациях корунда. *Журнал технической физики*. 2019;89(1):107–111.  
<https://doi.org/10.21883/JTF.2019.01.46970.102-18>
  8. Aragon-Duarte M.C., Nevarez-Rascon A., Esparza-Ponce H.E., Nevarez-Rascon M.M., Talamantes R.P., Ornelas C., Hurtado-Macias A. Nanomechanical properties of zirconia-yttria and alumina zirconia-yttria biomedical ceramics, subjected to low temperature aging. *Ceramics International*. 2017;43(5):3931–3939.  
<https://doi.org/10.1016/j.ceramint.2016.12.033>
  9. Rejab N.A., Azhar A.Z., Kian K.S., Ratnam M.M., Ahmad Z.A. Effects of MgO addition on the phase, mechanical properties, and microstructure of zirconia-toughened alumina added with CeO<sub>2</sub> (ZTA–CeO<sub>2</sub>) ceramic composite. *Materials Science and Engineering: A*. 2014;595:18–24.  
<https://doi.org/10.1016/j.msea.2013.11.091>
  10. Soylemez B., Sener E., Yurdakul A., Yurdakul H. Fracture toughness enhancement of yttria-stabilized tetragonal zirconia polycrystalline ceramics through magnesia-partially stabilized zirconia addition. *Journal of Science: Advanced Materials and Devices*. 2020;5(4):527–534.  
<https://doi.org/10.1016/j.jsamd.2020.09.003>
  11. Chieko Y., Armani P.J. Influence of Y<sub>2</sub>O<sub>3</sub> addition on the microstructure and mechanical properties of Mg–PSZ ceramics. *Materials Science and Engineering: A*. 2011; 1:556–561.
  12. Che T., Mao H.R., Guo R.F., Shen P. Ultrafast synthesis and pressureless densification of multicomponent nitride and carbonitride ceramics. *Ceramics International*. 2023; 49(19):31530–31538.  
<https://doi.org/10.1016/j.ceramint.2023.07.104>
  13. Kosyanov D.Yu., Zavjalov A.P., Vornovskikh A.A., Zakharenko A.M., Liu X., Li J. Some approaches for residual porosity estimating. *IOP Conference Series: Materials Science and Engineering*. 2021;1093(1):12–15.  
<https://doi.org/10.1088/1757-899X/1093/1/012015>
  14. Kuzmenko E.D. Investigation of physical and mechanical properties and microstructure of ceramics based on zirconium carbide and nitride. In: *Proceedings of the XII All Russian scientific conference on current issues of continuum mechanics and celestial mechanics (CICMCM 2023)* (Tomsk, Russia, 15–17 November 2023). Springer, Singapore: 2024. Vol. 412. P. 150–157.  
[https://doi.org/10.1007/978-981-97-1872-6\\_22](https://doi.org/10.1007/978-981-97-1872-6_22)
  15. Matrenin S.V., Mostovshchikov A.V., Mirovoy Yu.A. Study of the structure and physical and mechanical properties of ceramics based on aluminum and zirconium oxynitrides. *Bulletin of the Tomsk Polytechnic University. Geo Assets Engineering*. 2022;333(2):184–192. (In Russ.).  
<https://doi.org/10.18799/24131830/2022/2/3569>
  - Матренин С.В., Мостовщиков А.В., Мировой Ю.А. Исследование структуры и физико-механических свойств керамики на основе оксинитридов алюминия и циркония. *Известия Томского политехнического университета. Инжиниринг георесурсов*. 2022;333(2):184–192.  
<https://doi.org/10.18799/24131830/2022/2/3569>
  16. Moradkhani A., Panahizadeh V., Hoseinpour M. Indentation fracture resistance of brittle materials using irregular cracks: a review. *Heliyon*. 2023;9(9):12.  
<https://doi.org/10.1016/j.heliyon.2023.e19361>
  17. Ahmed Z.S., Chyad F.A. SEM-assisted thermophysical and mechanical properties of sintered MgO–ZrO<sub>2</sub> composite. *Energy Procedia*. 2013;36:872–880.  
<https://doi.org/10.1016/j.egypro.2013.07.100>
  18. Khakhalkin V.V., Kulkov S.N. Effect of hot pressing temperature on the phase composition and crystal structure parameters of the highly dispersed ZrO<sub>2</sub>–MgO powder system. *Perspektivnye Materialy*. 2010;(2):98–102. (In Russ.).
  - Хахалкин В.В., Кульков С.Н. Влияние температуры горячего прессования на фазовый состав и параметры кристаллической структуры высокодисперсной порошковой системы ZrO<sub>2</sub>–MgO. *Перспективные материалы*. 2010;(2):98–102.
  19. Song Q., Zha X., Gao M., Shi J., Ma Y. Influence of ZrO<sub>2</sub> on the phase composition and mechano-physical properties of MgO–ZrO<sub>2</sub> refractories prepared by cold isostatic press-

- ing. *Ceramics International*. 2024;50(17):30474–30482. <https://doi.org/10.1016/j.ceramint.2024.05.345>
20. Sniezek E., Szczerba J., Stoch P., Prorok R., Jastrzebska I., Bodnar W., Burkel E. Structural properties of MgO–ZrO<sub>2</sub> ceramics obtained by conventional sintering, arc melting and field assisted sintering technique. *Materials & Design*. 2016;99:412–420. <https://doi.org/10.1016/j.matdes.2016.03.106>
  21. Rada S., Zhang J., Rada R., Culea E. Advanced zirconia ceramics stabilized with yttria and magnesia: Structure and Vickers microhardness. *Journal of the Mechanical Behavior of Biomedical Materials*. 2022;134:105425. <https://doi.org/10.1016/j.jmbbm.2022.105425>
  22. Abdelgawad M., El-Gamal S.M.A., Ewais E.M., Li S. Effect of magnesia rich spinel on densification and stabilization behavior of monoclinic zirconia. *Journal of the Korean Ceramic Society*. 2021;58:276–286. <https://doi.org/10.1016/j.jmbbm.2022.105425>
  23. Jiang L., Guo S., Bian Y., Zhang M., Ding W. Effect of sintering temperature on mechanical properties of magnesia partially stabilized zirconia refractory. *Ceramics International*. 2016;42(9):10593–10598. <https://doi.org/10.1016/j.ceramint.2016.03.136>
  24. Kuzmenko E.D., Matrenin S.V., Nassyrbayev A.R. Physical and mechanical properties of ceramics based on ZrN–ZrO<sub>2</sub> obtained by spark plasma sintering method. *Bulletin of the Tomsk Polytechnic University. Geo Assets Engineering*. 2024;335(7):166–173. (In Russ.). <https://doi.org/10.18799/24131830/2024/7/4614>  
Кузьменко Е.Д., Матренин С.В., Насырбаев А.Р. Физико-механические свойства керамики на основе ZrN–ZrO<sub>2</sub>, полученной методом искрового плазменного спекания. *Известия Томского политехнического университета. Инжиниринг георесурсов*. 2024; 335(7):166–173. <https://doi.org/10.18799/24131830/2024/7/4614>
  25. Tkachev D.A., Buyakov A.S. Study of strength properties of porous composite ZrO<sub>2</sub>(MgO)–MgO under three-point bending. In: *Actual problems of modern mechanics of continuous media and celestial mechanics*. Tomsk: TSU, 2018. P. 154–158. (In Russ.).  
Ткачев Д.А., Буюков А.С. Исследование прочностных свойств пористого композита ZrO<sub>2</sub>(MgO)–MgO при трехточечном изгибе. В сб: *Актуальные проблемы современной механики сплошных сред и небесной механики*. Томск: ТГУ, 2018. С. 154–158.

## Information about the Authors



## Сведения об авторах

**Egor D. Kuzmenko** – Student, Division for Materials Science, School of Advanced Manufacturing Technologies, National Research Tomsk Polytechnic University (NRTPU)  
 **ORCID:** 0009-0006-7995-9776  
 **E-mail:** kuzmenko70egor@yandex.ru

**Егор Дмитриевич Кузьменко** – студент отделения материаловедения Инженерной школы новых производственных технологий Национального исследовательского Томского политехнического университета (НИТПУ)  
 **ORCID:** 0009-0006-7995-9776  
 **E-mail:** kuzmenko70egor@yandex.ru

**Sergey V. Matrenin** – Cand. Sci. (Eng.), Associate Professor, Division for Materials Science, School of Advanced Manufacturing Technologies, NRTPU  
 **ORCID:** 0000-0002-2188-8120  
 **E-mail:** msv@tpu.ru

**Сергей Вениаминович Матренин** – к.т.н., доцент отделения материаловедения Инженерной школы новых производственных технологий НИТПУ  
 **ORCID:** 0000-0002-2188-8120  
 **E-mail:** msv@tpu.ru

**Artur R. Nassyrbayev** – Assistant, Division for Power and Electrical Engineering, School of Energy & Power Engineering, NRTPU  
 **ORCID:** 0000-0003-4761-8863  
 **E-mail:** arn1@tpu.ru

**Артур Ринатович Насырбаев** – ассистент отделения электроэнергетики и электротехники Инженерной школы энергетики НИТПУ  
 **ORCID:** 0000-0003-4761-8863  
 **E-mail:** arn1@tpu.ru

## Contribution of the Authors



## Вклад авторов

**E. D. Kuzmenko** – development of the main research concept, sample testing, analysis of research results, manuscript preparation, and formulation of conclusions.

**Е. Д. Кузьменко** – формирование основной концепции исследования, проведение испытаний образцов, анализ результатов исследования, подготовка текста статьи, формулировка выводов.

**S. V. Matrenin** – definition of the research aim and objectives, sample testing, scientific supervision, manuscript revision, and refinement of conclusions.

**С. В. Матренин** – постановка цели и задачи исследования, проведение испытаний образцов, научное руководство, корректировка текста статьи, корректировка выводов.

**A. R. Nassyrbayev** – sample testing, performing calculations, and analysis of research results.

**А. Р. Насырбаев** – проведение испытаний образцов, проведение расчетов, анализ результатов исследования.

Received 31.01.2025  
 Revised 31.03.2025  
 Accepted 02.04.2025

Статья поступила 31.01.2025 г.  
 Доработана 31.03.2025 г.  
 Принята к публикации 02.04.2025 г.



UDC 621.9.048 : 621.793.182

<https://doi.org/10.17073/1997-308X-2025-3-48-59>

Research article

Научная статья



# Structure and properties of two-layer coatings in the HfSi<sub>2</sub>–HfB<sub>2</sub>–MoSi<sub>2</sub> system produced by electrospark deposition and magnetron sputtering

E. I. Zamulaeva<sup>✉</sup>, P. A. Loginov, Ph. V. Kiryukhantsev-Korneev,

N. V. Shvindina, M. I. Petrzhik, E. A. Levashov

National University of Science and Technology “MISIS”

1 Bld, 4 Leninskiy Prosp., Moscow 119049, Russia

✉ [zamulaeva@gmail.com](mailto:zamulaeva@gmail.com)

**Abstract.** A two-layer coating with a total thickness of approximately 15 μm was obtained using a combined technology of electrospark deposition (ESD) and high-power impulse magnetron sputtering (HiPIMS), employing HfSi<sub>2</sub>–HfB<sub>2</sub>–MoSi<sub>2</sub> ceramic electrodes/target on a niobium substrate. The formation mechanism, morphology, and structure of the coatings were investigated using glow discharge optical emission spectroscopy (GDOES), scanning electron microscopy (SEM), and transmission electron microscopy (TEM). It was found that the ESD coating consists of 65 wt. % phases formed through interaction between the electrode and the substrate – namely NbSi<sub>2</sub> and Nb<sub>5</sub>Si<sub>3</sub> – and exhibits a silicon concentration gradient (from 8 to 54 at. %) across the coating thickness, from the substrate toward the surface. The outer amorphous HiPIMS coating is ~5 μm thick. Analysis of structural and phase transformations during heating of the ESD coatings up to 900 °C showed that annealing leads to its separation into two layers: an inner layer composed of dendritic grains of the metastable γ-Nb<sub>5</sub>Si<sub>3</sub> phase and an outer layer based on NbSi<sub>2</sub>. The HiPIMS coating crystallizes sequentially, forming (Hf,Mo)B<sub>2</sub> at 700 °C, MoSi<sub>2</sub> at 800 °C, and Hf<sub>3</sub>Si<sub>2</sub> and HfSi<sub>2</sub> at 900 °C, with the silicon content remaining virtually unchanged. As a result of the two-stage deposition process and subsequent high-temperature annealing, a multilayer protective ceramic coating was obtained, consisting of an outer layer of (Hf,Mo)B<sub>2</sub>–MoSi<sub>2</sub>–HfSi<sub>2</sub>, an intermediate layer of NbSi<sub>2</sub>, and an inner layer of Nb<sub>5</sub>Si<sub>3</sub>, with hardness values of 9.4, 23.3, and 19.4 GPa, respectively. This coating significantly extends the service life of niobium grade Nb-1.

**Keywords:** electrospark deposition (ESD), high-power impulse magnetron sputtering (HiPIMS), oxidation-resistant ceramics, niobium substrate, two-layer coating, *in situ* HRTEM during heating, structural and phase transformations, selective nanoindentation

**Acknowledgements:** This research was supported by the Ministry of Science and Higher Education of the Russian Federation as part of the State Assignment (Project FSME-2025-0003).

**For citation:** Zamulaeva E.I., Loginov P.A., Kiryukhantsev-Korneev Ph.V., Shvindina N.V., Petrzhik M.I., Levashov E.A. Structure and properties of two-layer coatings in the HfSi<sub>2</sub>–HfB<sub>2</sub>–MoSi<sub>2</sub> system produced by electrospark deposition and magnetron sputtering. *Powder Metallurgy and Functional Coatings*. 2025;19(3):48–59. <https://doi.org/10.17073/1997-308X-2025-3-48-59>

# Структура и свойства двухслойных покрытий в системе $\text{HfSi}_2\text{–HfB}_2\text{–MoSi}_2$ , полученных методами электроискрового и магнетронного напыления

Е. И. Замулаева <sup>✉</sup>, П. А. Логинов, Ф. В. Кирюханцев-Корнеев,  
Н. В. Швындина, М. И. Петржик, Е. А. Левашов

Национальный исследовательский технологический университет «МИСИС»  
Россия, 119049, г. Москва, Ленинский пр-т, 4, стр. 1

✉ zamulaeva@gmail.com

**Аннотация.** При использовании комбинированной технологии электроискрового осаждения (ЭИО) и высокоомощного импульсного магнетронного распыления (ВИМР) с применением электрода/мишени из керамики  $\text{HfSi}_2\text{–HfB}_2\text{–MoSi}_2$  на подложке ниобия получено двухслойное покрытие толщиной ~15 мкм. Механизм формирования, морфология и структура покрытия исследованы методами рентгеноструктурного фазового анализа, оптической эмиссионной спектроскопии тлеющего разряда, рентгеноспектрального микроанализа, растровой и просвечивающей электронной микроскопии. Установлено, что ЭИО-покрытие на 65 мас. % состоит из фаз, являющихся продуктами взаимодействия электрода с подложкой:  $\text{NbSi}_2$ ,  $\text{Nb}_5\text{Si}_3$ , и имеет градиентное распределение кремния (от 8 до 54 ат. %) по толщине в направлении от подложки к поверхности покрытия. Верхнее аморфное ВИМР-покрытие характеризуется толщиной ~5 мкм. Анализ структурно-фазовых превращений при нагреве ЭИО-покрытия до 900 °С показал, что отжиг приводит к его разделению на два слоя: внутреннего из дендритных зерен метастабильной фазы  $\gamma\text{-Nb}_5\text{Si}_3$  и внешнего на основе  $\text{NbSi}_2$ . ВИМР-покрытие кристаллизуется с последовательным образованием фаз  $(\text{Hf},\text{Mo})\text{B}_2$  при 700 °С,  $\text{MoSi}_2$  при 800 °С и  $\text{Hf}_3\text{Si}_2$ ,  $\text{HfSi}_2$  при 900 °С. При этом содержание Si практически не изменяется. Таким образом, в результате двухстадийного процесса осаждения и последующего высокотемпературного отжига получено многослойное защитное керамическое покрытие, состоящее из внешнего слоя  $(\text{Hf},\text{Mo})\text{B}_2\text{–MoSi}_2\text{–HfSi}_2$ , промежуточного слоя  $\text{NbSi}_2$  и внутреннего слоя  $\text{Nb}_5\text{Si}_3$  со значениями твердости 9,4, 23,3 и 19,4 ГПа соответственно, позволяющее значительно продлить срок службы ниобия марки НБ-1.

**Ключевые слова:** электроискровое осаждение, высокоомощное импульсное магнетронное распыление, жаростойкая керамика, ниобиевая подложка, двухслойное покрытие, *in situ* ПЭМ ВР при нагреве, фазово-структурные превращения, избирательное наноидентифицирование

**Благодарности:** Работа выполнена при финансовой поддержке Министерства науки и высшего образования РФ в рамках государственного задания (проект FSME-2025-0003).

**Для цитирования:** Замулаева Е.И., Логинов П.А., Кирюханцев-Корнеев Ф.В., Швындина Н.В., Петржик М.И., Левашов Е.А. Структура и свойства двухслойных покрытий в системе  $\text{HfSi}_2\text{–HfB}_2\text{–MoSi}_2$ , полученных методами электроискрового и магнетронного напыления. *Известия вузов. Порошковая металлургия и функциональные покрытия*. 2025;19(3):48–59. <https://doi.org/10.17073/1997-308X-2025-3-48-59>

## Introduction

The potential for using niobium and its alloys in components operating at high temperatures and in aggressive gaseous environments largely depends on the application of protective coatings [1; 2]. Among the most promising are coatings based on silicides such as  $\text{NbSi}_2$  [3–5],  $\text{MoSi}_2$  [6–8],  $\text{NbSi}_2\text{–MoSi}_2$  [9], and  $\text{NbSi}_2\text{–HfSi}_2$  [10], due to the formation of a  $\text{SiO}_2$  film on their surface at elevated temperatures. A characteristic feature of such coatings is the formation of an intermediate diffusion layer of  $\text{Nb}_5\text{Si}_3$ . Since the enthalpy of formation of  $\text{Nb}_5\text{Si}_3$  (–516.8 kJ/mol) is lower than that of  $\text{NbSi}_2$  (–161 kJ/mol) [11; 12], the  $\text{Nb}_5\text{Si}_3$  layer forms first during thermochemical treatment and is subsequently transformed into the  $\text{NbSi}_2$  phase [3–12].

The rate of mutual diffusion between the coating and the substrate – which leads to coating thinning and, consequently, a reduction in performance – can be reduced by introducing diffusion barriers [13–15], modifying the coatings with diffusion inhibitors [16; 17], or forming additional layers of mullite ( $3\text{Al}_2\text{O}_3\cdot 2\text{SiO}_2$ ) [17; 18] or borosilicate glass ( $\text{B}_2\text{O}_3\cdot\text{SiO}_2$ ) [19; 20]. Multilayer coatings can also be produced by combining several technological approaches in a single process [21; 22] or by employing two-stage processes [2; 17].

In [23], the feasibility of using heterophase electrospark coatings based on  $\text{MoSi}_2\text{–MoB–HfB}_2$  to improve the performance of the heat-resistant nickel superalloy EP741NP was demonstrated. Enhancement of the oxidation resistance of electrospark coatings through the application of an upper magnetron-sputtered layer

has been demonstrated for steels [24] and nickel alloys [25].

The aim of this study is to fabricate two-layer ceramic coatings on Nb-1 niobium using a combination of electrospark deposition (ESD) and high-power impulse magnetron sputtering (HiPIMS), and to investigate the effect of vacuum annealing on their composition, structure, and properties.

## Materials and methods

The consumable ceramic electrodes and targets were produced by self-propagating high-temperature synthesis (SHS) from elements (wt. %: 59 Hf, 28 Si, 11 Mo, 2 B), followed by hot pressing of the synthesized products [26]. Both the ESD electrodes and the HiPIMS targets had the following phase composition (wt. %): hafnium silicide (34  $\text{HfSi}_2$ ), molybdenum silicide (17  $\text{MoSi}_2$ ), hafnium boride (19  $(\text{Hf},\text{Mo})\text{B}_2$ ), elemental silicon (21 Si), and hafnium oxide (9  $\text{HfO}_2$ ) [27]. The ESD electrodes were fabricated as rectangular rods measuring  $4\times 4\times 50$  mm, while the HiPIMS targets were discs with a diameter of 120 mm and a thickness of 10 mm.

The coatings were deposited onto Nb-1 niobium plates measuring  $10\times 10\times 3$  mm. The ESD process was carried out in an argon atmosphere using the Alier-303 Metal unit (Russia–Moldova) under the following parameters: discharge current 120 A, pulse frequency 3200 Hz, and pulse duration 20  $\mu\text{s}$ . HiPIMS deposition was performed using a UVN-2M system equipped with a magnetron and ion source. Target sputtering was performed using the TruPlasma 4002 system (Trumpf, Germany) at an average power of 1 kW, with a peak power of up to 50 kW, peak current of 50 A, pulse frequency of 1 kHz, and pulse duration of 50  $\mu\text{s}$ . The two-layer ESD + HiPIMS coatings were obtained by sequential application of the ESD and HiPIMS processes.

The microstructure and elemental composition were examined using an S-3400N scanning electron microscope (Hitachi High-Technology Corporation, Japan) equipped with a NORAN X-ray System 7 energy-dispersive X-ray spectroscopy (EDS) unit (Thermo Scientific, USA). Metallographic cross-sections were prepared using a Rotopol-21 polishing system (Struers, Denmark). Elemental depth profiling of the coatings was carried out by glow discharge optical emission spectroscopy (GDOES) using a Profiler-2 instrument (Horiba Jobin Yvon, France). Phase composition was determined by X-ray diffraction (XRD) using a DRON-4 automated diffractometer (Burevestnik R&D Center, Russia) with  $\text{CuK}_\alpha$  radiation over a  $2\theta$  range of  $10\text{--}120^\circ$ . The obtained X-ray diffraction patterns were analyzed using the JCPDS database.

To analyze the structural and phase transformations occurring in the coatings during heating, high-resolution transmission electron microscopy (HRTEM) and electron diffraction were used. The studies were carried out in the column of a JEM 2100 microscope (JEOL, Japan) during isothermal holding at temperatures of 400, 500, 600, 700, 800, and 900  $^\circ\text{C}$  for 20–25 min. The heating rate was 100  $^\circ\text{C}/\text{min}$ . The elemental compositions of the as-deposited coatings and those cooled from 900  $^\circ\text{C}$  were analyzed by EDS using an X-Max80T detector (Oxford Instruments, UK). Lamellae were prepared using focused ion beam (FIB) milling in a Scios DualBeam scanning electron-ion microscope (FEI, USA). Annealing of the coatings was performed in a VSI-16-22-U vacuum furnace (VakETO, Russia) at 900  $^\circ\text{C}$  for 30 min under low vacuum.

The hardness ( $H$ ) and Young's modulus ( $E$ ) of the coatings were determined by selective nanoindentation [28] using a NanoHardnessTester (CSM Instruments, Switzerland) with Indentation 3.0 software, in accordance with GOST R 8.748–2011 (ISO 14577).

## Results and discussion

Despite the use of the same material as both the electrode and target for coating deposition, the layers formed by electrospark deposition (ESD) and high-power impulse magnetron sputtering (HiPIMS) differ in structure and phase composition. During ESD, due to high temperatures in the interelectrode gap, local melting of the electrode and the treated substrate occurs, resulting in a coating with  $a \sim 10\text{--}12$  thickness (Fig. 1, *a*). Across the coating thickness, from the surface toward the substrate, an elemental concentration gradient is observed: the niobium content increases from 18 to 85 at. %, while the contents of the electrode-derived elements Hf, Mo, B, O, and silicon decrease from 54 to 8 at. % (Fig. 1, *b*).

During HiPIMS, the coating is formed by atomic fluxes with a high fraction of ionized species and has a thickness of  $\sim 5$   $\mu\text{m}$  (Fig. 1, *c*). The elemental concentrations within the HiPIMS-deposited layer remain constant throughout its thickness, and no substrate material (Nb) is detected in the coating, which is confirmed by the sharp interface (Fig. 1, *d*).

In sequentially deposited ESD + HiPIMS coatings, no pronounced interaction between the layers is observed (Fig. 1, *e*). The individual thicknesses of each layer are preserved, forming a two-layer coating with a total thickness of  $\sim 15$   $\mu\text{m}$ . EDS analysis shows that the niobium concentration in the ESD layer is 27.3 at. % (region 1 in Fig. 1, *e*, at. %: 8.8 O; 43.6 Si; 27.3 Nb; 4.9 Mo; 15.4 Hf), while in the HiPIMS layer it is only 0.5 at. % (region 2 in Fig. 1, *e*, at. %: 10.5 O; 55.0 Si;

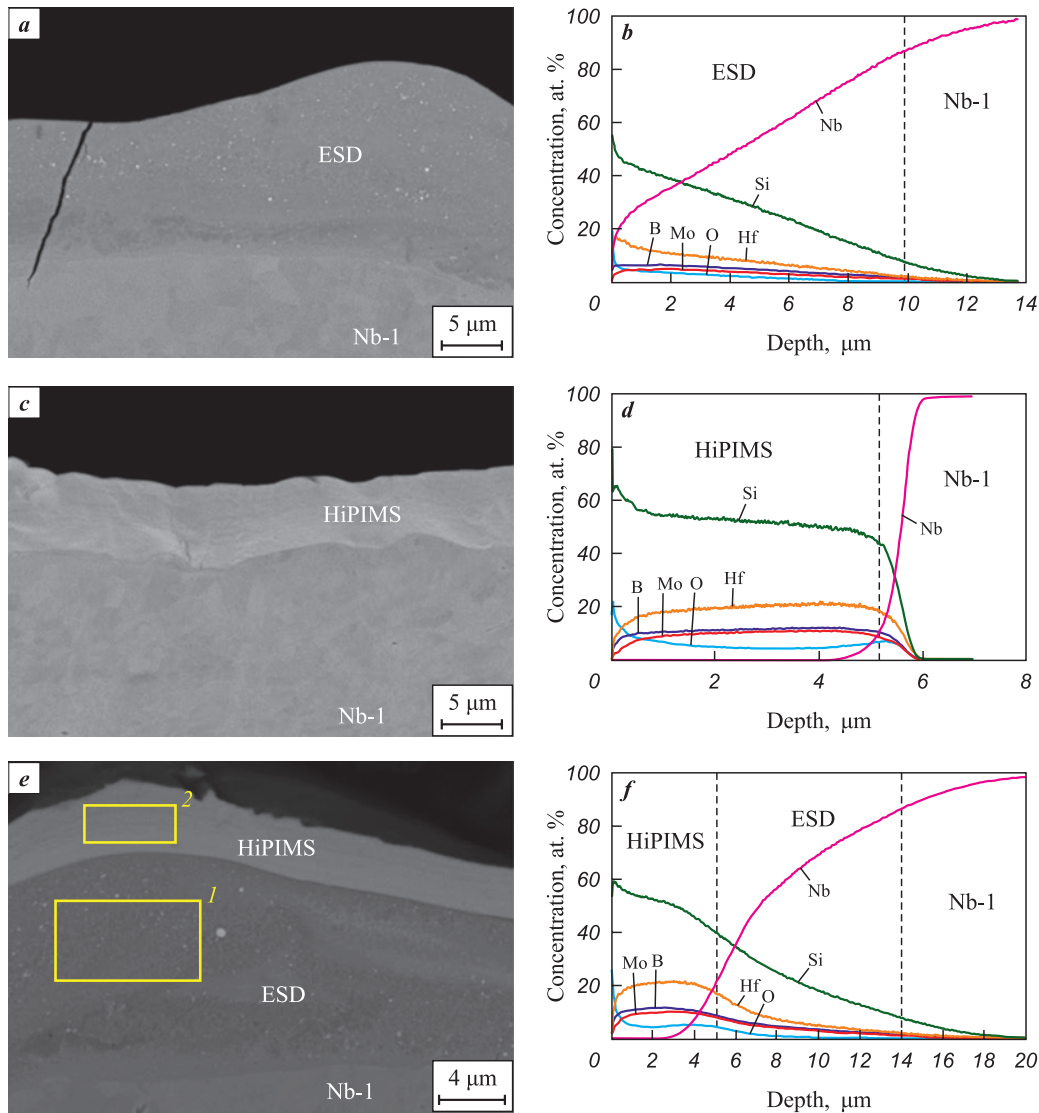


Fig. 1. Cross-sectional microstructures and GDOES profiles of coatings: (a, b); HiPIMS (c, d); ESD + HiPIMS (e, f)

Рис. 1. Микроструктуры поперечных шлифов и ОЭСТР-профили покрытий ЭИО (a, b); ВИМП (c, d); ЭИО + ВИМП (e, f)

0.5 Nb; 10.3 Mo; 23.7 Hf). The GDOES profile can be divided into three zones: the first (0–5 μm) corresponds to the magnetron-sputtered layer, the second (approximately 5–14 μm) corresponds to the ESD coating, and the final section corresponds to the substrate (Fig. 1, f).

X-ray diffraction patterns of the coatings are shown in Fig. 2. The formation of NbSi<sub>2</sub> and Nb<sub>5</sub>Si<sub>3</sub> phases in the ESD layer – as a result of interfacial diffusion-reactions between the electrode material and the niobium substrate – indicates strong adhesion of the coating to the substrate (Fig. 2, a). The coating also contains (Hf,Mo)B<sub>2</sub>, free Si, and HfO<sub>2</sub> phases, consistent with the electrode composition. In the microstructure, HfO<sub>2</sub> appears as bright inclusions (Figs. 1, a, e). After vacuum annealing, all major phases remain present at approximately the same concentrations (Fig. 2, b, Table 1). The Si phase disappears due to its reaction

with the substrate, forming NbSi<sub>2</sub>. In addition, a Nb<sub>2</sub>B<sub>3</sub> boride phase forms in an amount of 5 wt. %.

The HiPIMS coating is X-ray amorphous: the diffractogram shows only substrate reflections and broad amorphous halos (Fig. 2, c). However, after vacuum annealing, crystalline phases such as HfSi<sub>2</sub>, MoSi<sub>2</sub>, and (Hf,Mo)B<sub>2</sub> are identified (Fig. 2, d). The formation of NbSi<sub>2</sub> is attributed to the diffusion of niobium from the substrate, while the presence of MoO<sub>3</sub> results from residual oxygen impurities in the target material. The phase analysis results are summarized in Table 2, excluding the contribution of the substrate (Nb), as the coating thickness is less than the X-ray penetration depth.

The microstructure of the ESD + HiPIMS coating after vacuum annealing is shown in Fig. 3, a. Within the electrosputtered layer, an outer region with a sharply defined boundary forms, corresponding

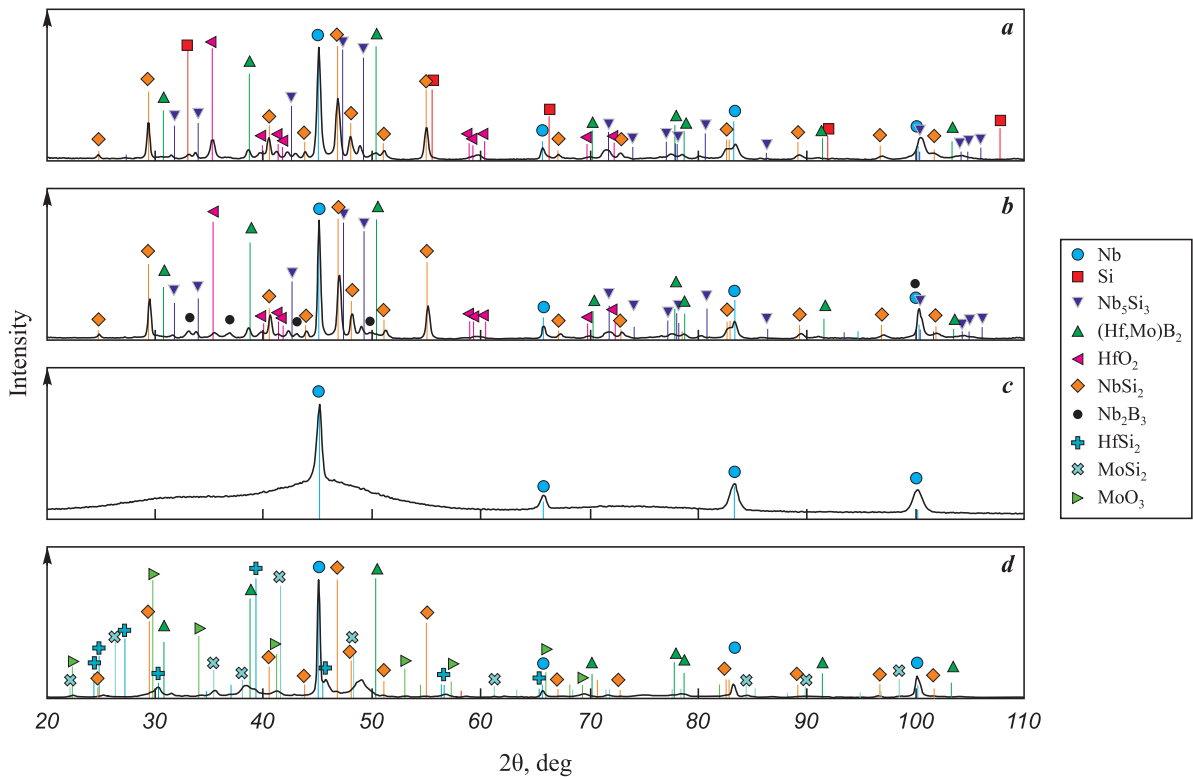


Fig. 2. X-ray diffraction patterns of ESD (*a, b*) and HiPIMS (*c, d*) coatings  
*a, c* – before annealing; *b, d* – after annealing ( $t = 900\text{ }^{\circ}\text{C}$ ,  $\tau = 30\text{ min}$ )

Рис. 2. Рентгенограммы покрытий ЭИО (*a, b*) и ВИМП (*c, d*)  
*a, c* – до отжига; *b, d* – после отжига ( $t = 900\text{ }^{\circ}\text{C}$ ,  $\tau = 30\text{ мин}$ )

to the NbSi<sub>2</sub> phase (region 2 in Fig. 3, *a*, at. %: 2.9 O; 64.2 Si; 28.8 Nb; 2.1 Mo; 2.0 Hf). Bright HfO<sub>2</sub> inclusions are observed both in the outer dark layer and in the inner layer adjacent to the substrate. According to EDS data, the inner region contains a lower silicon concentration of 28.1 at. % (region 3, at. %: 7.4 O; 28.1 Si; 48.3 Nb; 4.2 Mo; 12.0 Hf). These results indicate that heat treatment promotes silicon homogenization within the ESD layer and reduces microscale com-

positional inhomogeneities originating from individual mass transfer events. The magnetron-sputtered layer, which is compositionally and structurally uniform, retains its original composition after crystallization (region 1, at. %: 11.5 O; 52.8 Si; 0.5 Nb; 10.9 Mo; 24.1 Hf) and does not contribute to NbSi<sub>2</sub> formation. The elemental distribution map confirms an increased silicon concentration in the outer ESD layer and a higher niobium content in the inner region (Fig. 3, *b*).

Table 1. Phase composition of ESD coatings before and after annealing

Таблица 1. Фазовый состав ЭИО-покрытий до и после отжига

Phase	Structure type	As-deposited coating			Annealed coating		
		Content, wt. %	Lattice parameter, nm		Content, wt. %	Lattice parameter, nm	
			<i>a</i>	<i>c</i>		<i>a</i>	<i>c</i>
NbSi <sub>2</sub>	<i>hP9/3</i>	49	0.4785	0.6591	50	0.4783	0.6589
Nb <sub>5</sub> Si <sub>3</sub>	<i>hP16/19</i>	15	0.7565	0.5260	13	0.7578	0.5258
(Hf,Mo)B <sub>2</sub>	<i>hP3/4</i>	3	0.3112	0.3358	4	0.3123	0.3373
Si	<i>cF8/1</i>	3	0.5417	–	–	–	–
HfO <sub>2</sub>	<i>oP24/16</i>	8	–	–	7	–	–
Nb <sub>2</sub> B <sub>3</sub>	<i>oC20/4</i>	–	–	–	5	–	–
Nb	<i>cI2/1</i>	22	0.3294	–	21	0.3300	–

**Table 2. Phase composition of HiPIMS coating after annealing**

**Таблица 2. Фазовый состав ВИМР-покрытия после отжига**

Phase	Structure type	Content, wt. %	Lattice parameter, nm		
			<i>a</i>	<i>b</i>	<i>c</i>
HfSi <sub>2</sub>	<i>oC12/1</i>	31	3.698	14.648	3.678
MoSi <sub>2</sub>	<i>hP3/4</i>	34	0.4602	–	0.6570
HfB <sub>2</sub>	<i>hP3/4</i>	12	0.3141	–	0.3470
NbSi <sub>2</sub>	<i>hP9/3</i>	10	0.4801	–	0.6600
MoO <sub>3</sub>	<i>mP8/6</i>	13	1.0595	–	0.3728

The initial lamella containing both ESD and HiPIMS layers, used for in situ investigation of structural and phase transformations during heating in the TEM column, is shown in Fig. 4, *a*. After cooling from 900 °C, a new layer appears at the interface with the HiPIMS coating (Fig. 4, *b*). According to EDS data, its composition corresponds to the NbSi<sub>2</sub> phase (Fig. 4, *c*). Electron diffraction analysis confirms this identification: diffraction rings with interplanar spa-

cings  $d/n = 0.356, 0.218, 0.210,$  and  $0.136$  nm correspond to the (101), (111), (112), and (114) planes of the  $h$ -NbSi<sub>2</sub> phase. Additional rings with  $d/n = 0.638, 0.319, 0.240, 0.218, 0.210,$  and  $0.140$  nm, corresponding to the (100), (200), (210), (211), (112), and (402) planes, are assigned to the Nb<sub>5</sub>Si<sub>3</sub> phase (Fig. 4, *d*).

No significant structural changes were observed in the inner region of the ESD coating during heating (Figs. 5, *a–c*). However, after cooling the sample from 900 °C to room temperature, contrast variations appeared in certain areas. These may be attributed either to diffusion-driven elemental redistribution – accompanied by the dissolution of some structural and phase components – or to stress relaxation (Fig. 5, *d*).

As a result of non-equilibrium crystallization during ESD,  $\gamma$ -Nb<sub>5</sub>Si<sub>3</sub> phase grains are observed in the coating, formed in the direction from the substrate toward the surface and resembling dendrites in their morphology. Dendritic growth of the metastable Nb<sub>5</sub>Si<sub>3</sub> phase due to non-equilibrium crystallization in Nb–Si alloys has been reported in [29; 30]. A HRTEM image of a silicide grain oriented along the  $[\bar{1}10]$  direction, the cor-

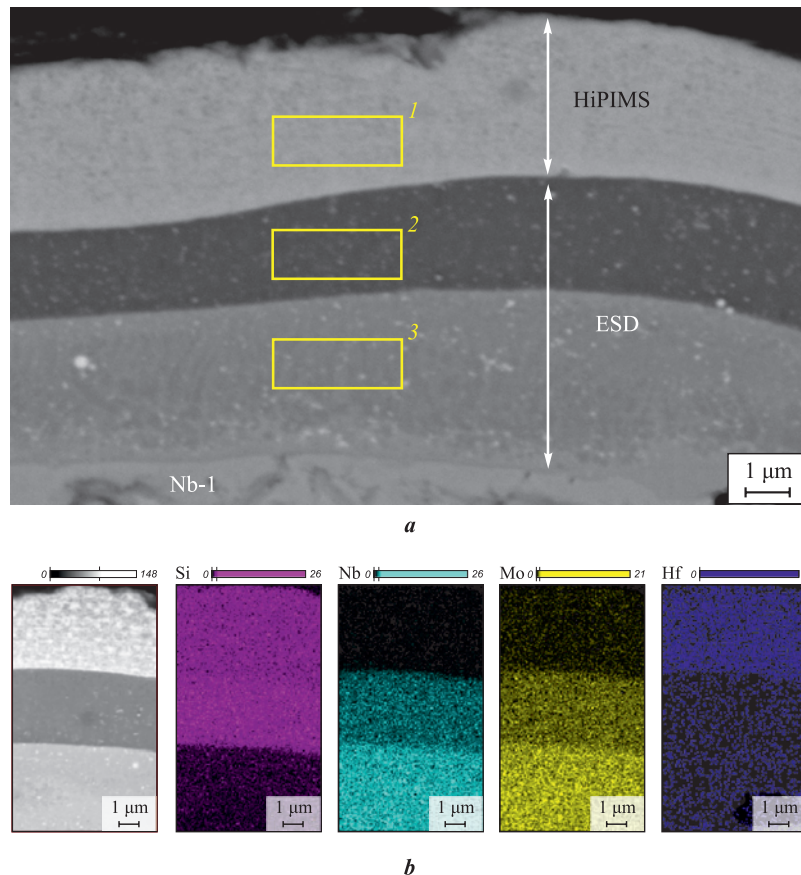


**Fig. 3. Microstructure of the ESD + HiPIMS coating (a) and elemental distribution map in the intermediate layer (b) after heat treatment**

**Рис. 3. Микроструктура ЭИО+ВИМР-покрытия (a) и карта распределения элементов в промежуточном слое (b) после отжига**

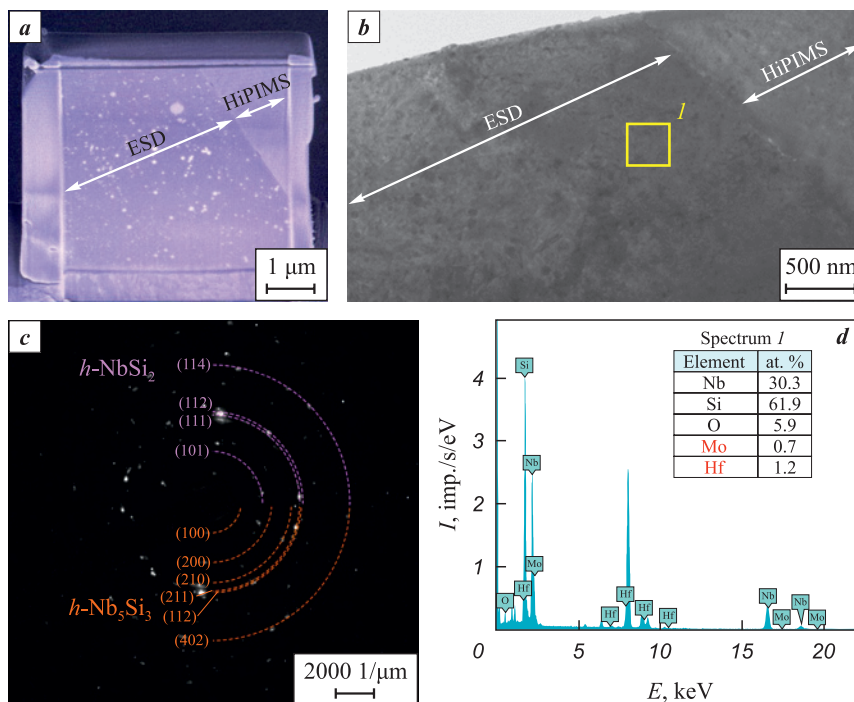


Fig. 4. Microstructure of the lamella before (a) and after heating and cooling from 900 °C (b); electron diffraction pattern (c) and EDS data (d) for the intermediate layer

Рис. 4. Микроструктура ламели до (a) и после нагрева и охлаждения с 900 °C (b); электронограмма (c) и данные РСМА (d) для промежуточного слоя

responding electron diffraction pattern, and EDS data are shown in Figs. 5, e–g. The presence of HfO<sub>2</sub> grains, 50–100 nm in size, was also confirmed in the coating. A HRTEM image of an oxide particle oriented along the [024] direction, together with the corresponding diffraction pattern and EDS results, is presented in Figs. 5, h–j.

The HiPIMS coating remains stable up to 600 °C and retains a layered structure (Fig. 6, a). The corresponding electron diffraction pattern displays a broad diffuse ring, indicating that the coating is in an amorphous state. Crystallization begins at 700 °C, as evidenced by the appearance of diffraction rings with interplanar spacings of  $d/n = 0.355, 0.261, 0.213,$  and  $0.178$  nm, corresponding to the (001), (100), (101),

and (002) planes of the (Hf,Mo)B<sub>2</sub> phase (Figs. 6, b, f). As the temperature increases to 800 °C, additional reflections emerge at  $d/n = 0.291, 0.225,$  and  $0.213$  nm, attributed to the (101), (110), and (103) planes of the MoSi<sub>2</sub> phase (Figs. 6, c, g).

Further heating to 900 °C leads to the formation of hafnium silicides. Hf<sub>3</sub>Si<sub>2</sub>, reflections corresponding to the (110), (001), (210), and (211) planes with  $d/n = 0.493, 0.357, 0.309,$  and  $0.262$  nm indicate the presence of Hf<sub>3</sub>Si<sub>2</sub>, while reflections at  $0.355, 0.262, 0.226,$  and  $0.206$  nm from the (110), (111), (131), and (061) planes correspond to HfSi<sub>3</sub> (Figs. 6, d, h). After cooling, the coating structure remained unchanged. Four crystalline phases were observed: Hf<sub>3</sub>Si<sub>2</sub>, HfSi<sub>2</sub>, MoSi<sub>2</sub>, and (Hf,Mo)B<sub>2</sub>.

Table 3. Mechanical properties of coatings and Nb-1 substrate

Таблица 3. Механические свойства покрытий и подложки

ESD coating		HiPIMS coating		Nb-1 substrate	
As-deposited	Annealed	As-deposited	Annealed	As-deposited	Annealed
<i>H</i> , GPa					
18.3	23.3*/19.4**	12.5	9.3	1.8	2.5
<i>E</i> , GPa					
285	292*/256**	216	207	123	112
* Outer layer based on NbSi <sub>2</sub> .					
** Inner layer based on Nb <sub>3</sub> Si <sub>3</sub> .					

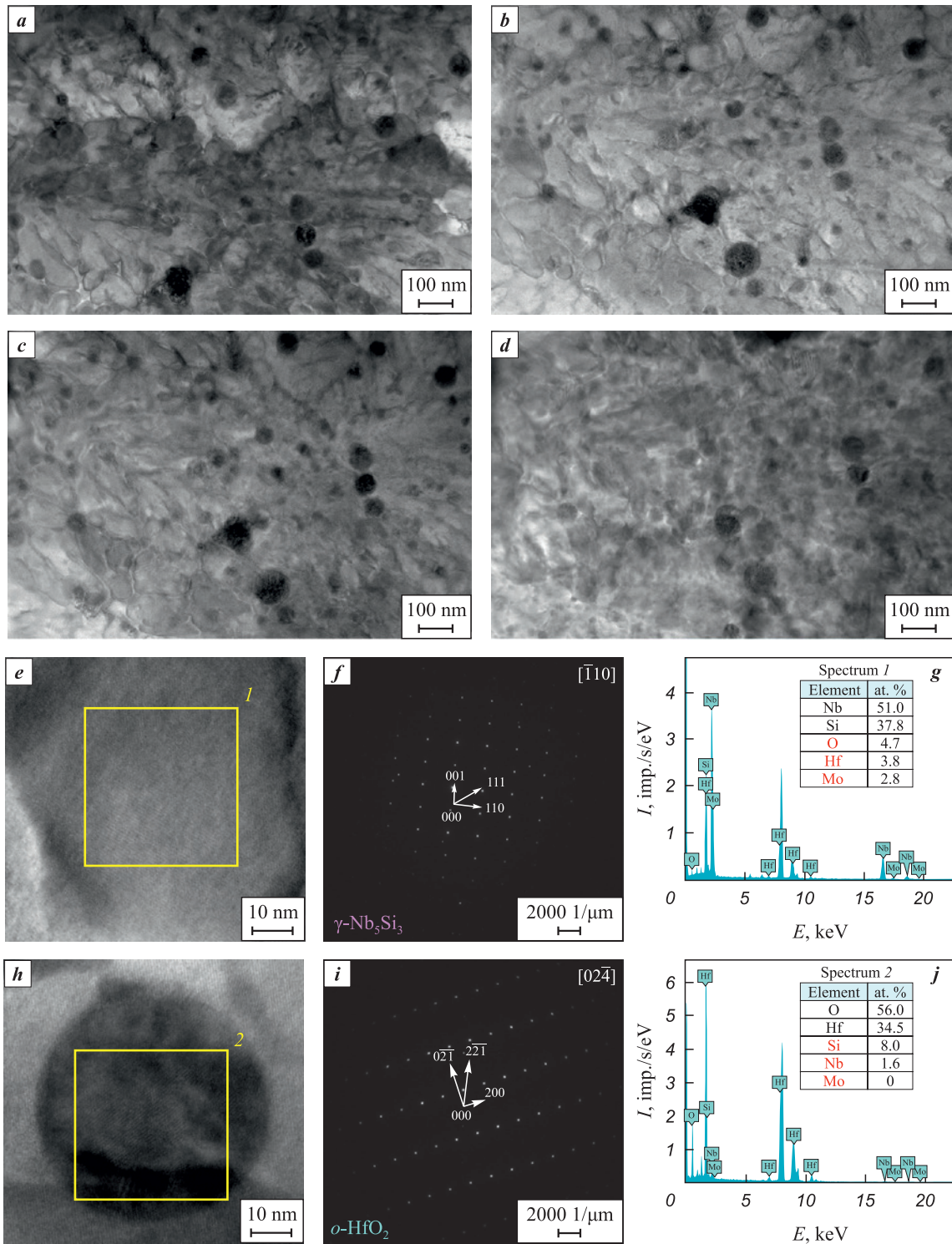


**Fig. 5.** Inner layer microstructures of ESD-coating before annealing (a), during *in situ* heating to 400 °C (b), 800 °C (c), and after cooling from 900 °C (d); silicide phase grain (e), its electron diffraction pattern (f) and EDS data (g); oxide particle (h), its electron diffraction pattern (i), and EDS data (j)

**Рис. 5.** Микроструктуры внутреннего слоя ЭИО-покрытия до отжига (a), при *in situ* нагреве до 400 °C (b), 800 °C (c), а также после охлаждения с 900 °C (d); зерно силицидной фазы (e), его электронограмма (f) и данные РСМА (g); оксидная частица (h), ее электронограмма (i) и данные РСМА (j)

Table 3 presents the hardness (*H*) and elastic modulus (*E*) values for the coatings and the substrate. The hardness of the as-deposited ESD coating is uni-

form across the thickness and amounts to 18.3 GPa. After annealing, the inner layer retains a hardness of *H* = 19.4 GPa, indicating the absence of structural

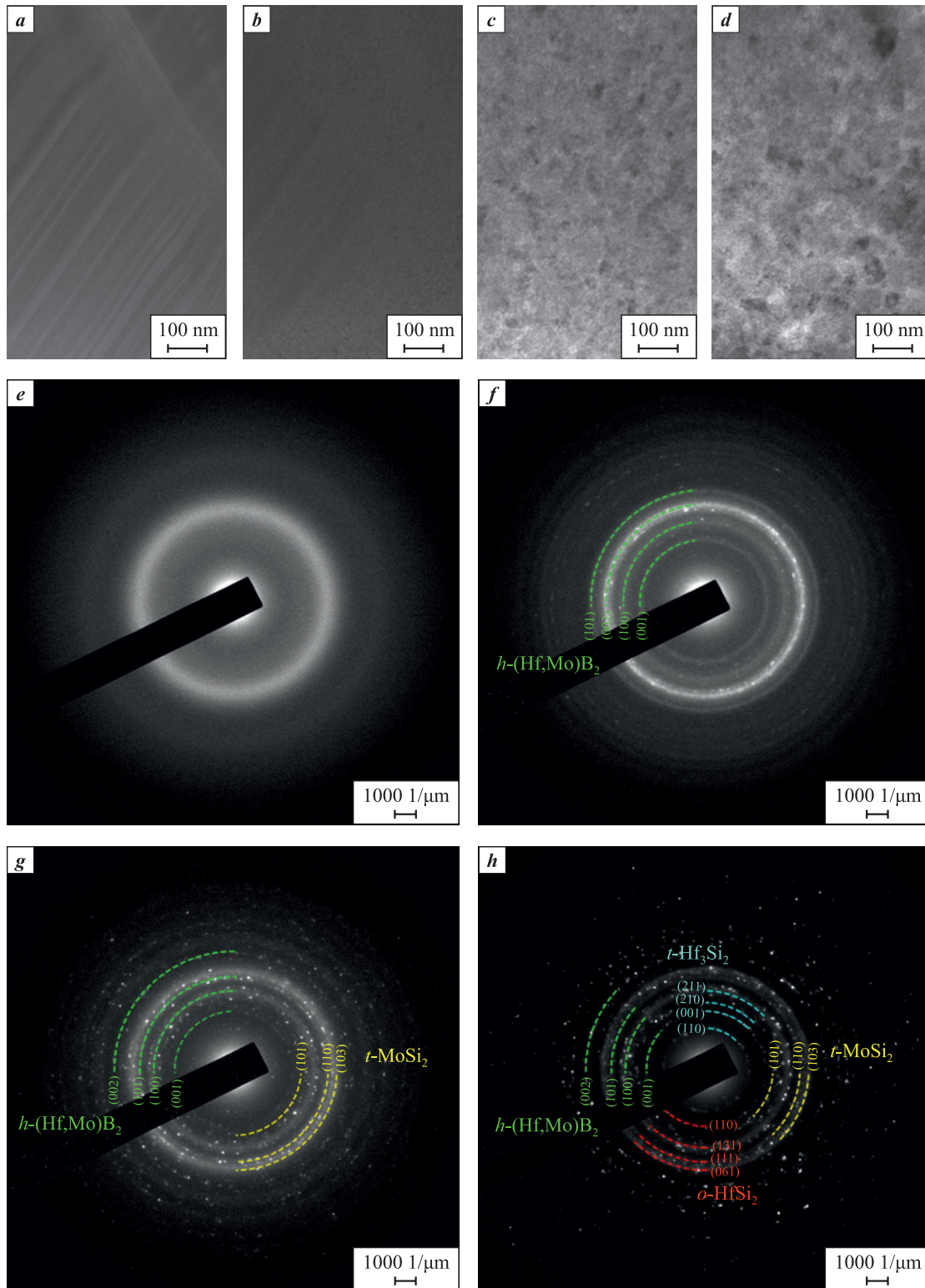


**Fig. 6.** Microstructures (*a–d*) and electron diffraction patterns (*e–h*) of the HiPIMS coating during *in situ* heating to 600 °C (*a, e*), 700 °C (*b, f*), and 800 °C (*c, g*), and after cooling from 900 °C (*d, h*)

**Рис. 6.** Микроструктуры (*a–d*) и электронограммы (*e–h*) ВИМР-покрытия при *in situ* нагреве до 600 °C (*a, e*), 700 °C (*b, f*), 800 °C (*c, g*), а также после охлаждения с 900 °C (*d, h*)

transformations in the  $\text{Nb}_5\text{Si}_3$ -based layer. A slight decrease in the elastic modulus may be attributed to an increased Nb content due to diffusion from the sub-

strate into the  $\text{NbSi}_2$ -based layer. The hardness value of 23.3 GPa in the outer layer is attributed to the inherently higher hardness of the  $\text{NbSi}_2$  phase compared

to  $\text{Nb}_5\text{Si}_3$ , the absence of free niobium in this region, and alloying with niobium boride additions  $(\text{Hf},\text{Mo})\text{B}_2$  and  $\text{Nb}_2\text{B}_3$ . For the HiPIMS coating, the hardness is  $H = 12.5$  GPa, which corresponds to reported values for magnetron-deposited Hf–Si–Mo–B coatings [31]. After vacuum annealing and stress relaxation, the hardness decreases to 9.3 GPa. The increase in substrate hardness from 1.8 to 2.5 GPa following annealing is attributed to silicon diffusion into the interfacial region.

## Conclusions

1. A 15  $\mu\text{m}$ -thick two-layer coating was fabricated on a Nb-1 substrate by sequential application of electrospark deposition (ESD) and high-power impulse magnetron sputtering (HiPIMS) using  $\text{HfSi}_2$ – $\text{HfB}_2$ – $\text{MoSi}_2$  SHS-ceramic electrodes/targets. The ESD layer,  $\sim 10$ – $12$   $\mu\text{m}$  thick, consists of  $\sim 65$  wt. % phases formed as a result of interfacial reactions between the electrode and the substrate, primarily  $\text{NbSi}_2$  and  $\text{Nb}_5\text{Si}_3$  ( $H = 18.3$  GPa,  $E = 285$  GPa). A compositional gradient was observed across the ESD coating, with the Nb content increasing from 18 to 85 at. % and the Si concentration decreasing from 54 to 8 at. % from the surface toward the substrate. The HiPIMS coating has a homogeneous amorphous structure,  $\sim 5$   $\mu\text{m}$  thick, with  $H = 12.5$  GPa and  $E = 216$  GPa.

2. During heating, an interlayer  $\sim 2$   $\mu\text{m}$  thick based on  $\text{NbSi}_2$  forms at the interface between the ESD and HiPIMS layers ( $H = 23.3$  GPa,  $E = 292$  GPa). The inner ESD layer consists of dendritic grains of the metastable  $\gamma$ - $\text{Nb}_5\text{Si}_3$  phase solidified perpendicular to the substrate surface ( $H = 19.4$  GPa,  $E = 256$  GPa). Crystallization of the HiPIMS layer begins at 700 °C with the formation of  $(\text{Hf},\text{Mo})\text{B}_2$ . Upon further heating to 800 °C,  $\text{MoSi}_2$  appears, and at 900 °C,  $\text{HfSi}_2$  and  $\text{Hf}_3\text{Si}_2$  phases are detected. After vacuum annealing, mechanical properties decrease slightly ( $H = 9.4$  GPa,  $E = 207$  GPa), which may be attributed to stress relaxation. Since the silicon content remains unchanged, the HiPIMS layer does not contribute to the formation of the  $\text{NbSi}_2$ -based interlayer. Thus, heat treatment results in the formation of a multi-layer coating with enhanced mechanical properties.

## References / Список литературы

- Kashin D.S., Stekhov P.A. Development of heat-resistant coatings for parts made of heat-resistant alloys based on niobium. *Trudy VIAM*. 2017;49(1):1–10. (In Russ.). <https://doi.org/10.18577/2307-6046-2015-0-6-1-1>  
Кашин Д.С., Стехов П.А. Разработка жаростойких покрытий для деталей из жаропрочных сплавов на основе ниобия. *Труды ВИАМ*. 2017;49(1):1–10. <https://doi.org/10.18577/2307-6046-2015-0-6-1-1>
- Babak V.P., Lyashenko B.A., Shchepetov V.V., Kharchenko S.D. Heat protective coatings on niobium alloys. *Mechanics and Advanced Technologies*. 2020;90(3):88–98. <https://doi.org/10.20535/2521-1943.2020.0.219550>
- Fu T., Chen L., Zhang Y., Shen F., Zhu J. Microstructure and oxidation resistant of Si– $\text{NbSi}_2$  coating on Nb substrate at 800 °C and 1000 °C. *Ceramics International*. 2023;49(13):21222–21233. <https://doi.org/10.1016/j.ceramint.2023.03.252>
- Choi Y.-J., Yoon J.-K., Kim G.-H., Yoon W.-Y., Doh J.-M., Hong K.-T. High temperature isothermal oxidation behavior of  $\text{NbSi}_2$  coating at 1000–1450 °C. *Corrosion Science*. 2017;129:102–114. <https://doi.org/10.1016/j.corsci.2017.10.002>
- Yoon J.-K., Kim G.-H. Accelerated oxidation behavior of  $\text{NbSi}_2$  coating grown on Nb substrate at 600–900 °C. *Corrosion Science*. 2018;141:97–108. <https://doi.org/10.1016/j.corsci.2018.07.001>
- Sun L., Fu Q.-G., Fang X.-Q., Sun J. A  $\text{MoSi}_2$ -based composite coating by supersonic atmospheric plasma spraying to protect Nb alloy against oxidation at 1500 °C. *Surface and Coatings Technology*. 2018;352:182–190. <https://doi.org/10.1016/j.surfcoat.2018.07.091>
- Yan J., Liu L., Mao Z., Xu H., Wang Y. Effect of spraying powders size on the microstructure, bonding strength, and microhardness of  $\text{MoSi}_2$  coating prepared by air plasma spraying. *Journal of Thermal Spray Technology*. 2014;23:934–939. <https://www.doi.org/10.1007/s11666-014-0120-3>
- Yan J.-H., Wang Y., Liu L.-F., Wang Y. Oxidation and interdiffusion behavior of niobium substrate coated  $\text{MoSi}_2$  coating prepared by spark plasma sintering. *Applied Surface Science*. 2014;320:791–797. <https://www.doi.org/10.1016/j.apsusc.2014.09.018>
- Xiao L., Zhou X., Wang Y., Pu R., Zhao G., Shen Z., Huang Y., Liu S., Cai Z., Zhao X. Formation and oxidation behavior of Ce-modified  $\text{MoSi}_2$ – $\text{NbSi}_2$  coating on niobium alloy. *Corrosion Science*. 2020;173:108751. <https://doi.org/10.1016/j.corsci.2020.108751>
- Bukhanovskii V.V., Borisenko V.A., Kharchenko V.K., Mamuzic I. High-temperature strength of niobium alloy 5VMTs with a silicide-ceramic coating. Part 1. Short-term strength characteristics. *Strength of Materials*. 2004;36(2):159–202. <https://doi.org/10.1023/B:STOM.0000028311.58809.f9>
- Fernandes P.B., Coelho G.C., Ferreira F., Nunes C.A., Sundman B. Thermodynamic modeling of the Nb–Si system. *Intermetallics*. 2002;10(10):993–999. [https://doi.org/10.1016/S0966-9795\(02\)00125-5](https://doi.org/10.1016/S0966-9795(02)00125-5)
- Shen F., Fu T., Zhang Y., Gao Q., Chen L. Synthesis of Si– $\text{NbSi}_2$  coatings on Nb substrate by hot dip silicon-plating method under the various deposition temperatures. *Applied Physics A*. 2022;128:984. <https://doi.org/10.1007/s00339-022-06129-0>
- Qiao Y., Chen T., Guo X. Diffusion barrier effect of  $\text{Al}_2\text{O}_3$  layer at the interface between Mo–Si–B coating and Nb–Si based alloy. *Corrosion Communications*. 2021;4:45–56. <https://doi.org/10.1016/j.corcom.2021.10.003>
- Yue G., Guo X., Qiao Y. Study on the diffusion barrier effect of  $\text{WSi}_2$  layer at the  $\text{MoSi}_2$ /Nb–Ti–Si based alloy interface. *Corrosion Science*. 2020;163:108299. <https://doi.org/10.1016/j.corsci.2019.108299>
- Kurokawa K., Ochiai G., Takahashi H., Ohta S., Takahashi H. Effects of sputter-deposited materials (W, Ti

- and SiC) on interfacial reaction between  $\text{MoSi}_2$  and Nb. *Vacuum*. 2000;59(1):284–291.  
[https://doi.org/10.1016/S0042-207X\(00\)00281-5](https://doi.org/10.1016/S0042-207X(00)00281-5)
16. Zhang Y., Fu T., Yu L., Cui K., Wang J., Shen F., Zhang X., Zhou K. Anti-corrosion coatings for protecting Nb-based alloys exposed to oxidation environments: A review. *Metals and Materials International*. 2023;29(1):1–17.  
<https://doi.org/10.1007/s12540-022-01222-8>
  17. Zhang X., Fu T., Cui K., Zhang Y., Shen F., Wang J., Yu L., Mao H. The protection, challenge, and prospect of anti-oxidation coating on the surface of niobium alloy. *Coatings*. 2021;11(7):742.  
<https://doi.org/10.3390/coatings11070742>
  18. Zhang K., Lei S., Yang R., Zhang Y., Chen S., Zhang X., Li W. Formation and oxidation behavior of  $\text{SiO}_2/\text{NbSi}_2$  multilayer coating fabricated by one-step method. *Surface and Coatings Technology*. 2023;452:129117.  
<https://doi.org/10.1016/j.surfcoat.2022.129117>
  19. Su L., Lu-Steffes O., Zhang H., Perepezko J.H. An ultra-high temperature Mo–Si–B based coating for oxidation-protection of NbSS/ $\text{Nb}_3\text{Si}_3$  composites. *Applied Surface Science*. 2015;337:38–44.  
<http://doi.org/10.1016/j.apsusc.2015.02.061>
  20. Burk S., Gorr B., Krüger M., Heilmaier M., Christ H.-J. Oxidation behavior of Mo–Si–B–(X) alloys: Macro- and microalloying (X = Cr, Zr,  $\text{La}_2\text{O}_3$ ). *JOM: The Journal of the Minerals, Metals and Materials Society*. 2011; 63(12):32–36. <https://doi.org/10.1007/s11837-011-0203-2>
  21. Zhang P., Li Y., Chen Z., Shen C., Feng P. Preparation and moderate temperature oxidation behavior of Ti- and Al-doped  $\text{NbSi}_2\text{–Si}_3\text{N}_4$  composite coatings on Nb alloy. *Surface and Coatings Technology*. 2019;379:125005.  
<https://doi.org/10.1016/j.surfcoat.2019.125005>
  22. Xiao L., Zhou X., Wang Y., Pu R., Zhao G., Shen Z., Huang Y., Liu S., Cai Z., Zhao X. Formation and oxidation behavior of Ce-modified  $\text{MoSi}_2\text{–NbSi}_2$  coating on niobium alloy. *Corrosion Science*. 2020;173:108751.  
<https://doi.org/10.1016/j.corsci.2020.108751>
  23. Zamulaeva E.I., Zinovieva M.V., Kiryukhantsev-Korneev Ph.V., Petrzhik M.I., Kaplanskii Yu.Yu., Klechkovskaya V.V., Sviridova T.A., Shvyndina N.V., Levashov E.A. Protective coatings deposited onto LPBF-manufactured nickel superalloy by pulsed electrospark deposition using  $\text{MoSi}_2\text{–MoB–HfB}_2$  and  $\text{MoSi}_2\text{–MoB–ZrB}_2$  electrodes. *Surface and Coatings Technology*. 2021;427:127806.  
<https://doi.org/10.1016/j.surfcoat.2021.127806>
  24. Kiryukhantsev-Korneev P.V., Sytchenko A.D., Gorshkov V.A., Loginov P.A., Sheveyko A.N., Nozhkina A.V., Levashov E.A. Complex study of protective  $\text{Cr}_3\text{C}_2\text{–NiAl}$  coatings deposited by vacuum electro-spark alloying, pulsed cathodic arc evaporation, magnetron sputtering, and hybrid technology. *Ceramics International*. 2022;48(8):10921–10931.  
<https://doi.org/10.1016/j.ceramint.2021.12.311>
  25. Kiryukhantsev-Korneev Ph.V., Kudryashov A.E., Sheveyko A.N., Orekhov A.S., Levashov E.A. Improving the oxidation resistance of Inconel 718 high-temperature nickel alloy using combined surface engineering technology. *Letters on Materials*. 2020;10(4):371–376. (In Russ.).  
<https://doi.org/10.22226/2410-3535-2020-4-371-376>
  - Кiryukhantsev-Korneev Ф.В., Кудряшов А.Е., Шейко А.Н., Орехов А.С., Левашов Е.А. Повышение окислительной стойкости жаропрочного никелевого сплава ЭП-718 ИД с помощью комбинированной технологии инженерии поверхности. *Письма о материалах*. 2020;10(4):371–376.  
<https://doi.org/10.22226/2410-3535-2020-4-371-376>
  26. Погожев Ю.С., Лемешева М.В., Потанин А.Ю., Рупасов С.И., Вершинников В.И., Левашов Е.А. Гетерофазная керамика в системе Hf–Si–Mo–B, полученная сочетанием методов СВС и горячего прессования. *Известия вузов. Цветная металлургия*. 2019;(3):36–46  
<https://doi.org/10.17073/0021-3438-2019-3-36-46>
  - Pogozhev Yu.S., Lemesheva M.V., Potanin A.Yu., Rupasov S.I., Vershinnikov V.I., Levashov E.A. Heterophase ceramics in the Hf–Si–Mo–B system fabricated by the combination of SHS and hot pressing methods. *Russian Journal of Non-Ferrous Metals*. 2019;(4):380–389.  
<https://doi.org/10.3103/S1067821219040102>
  27. Zamulaeva E.I., Kudryashov A.E., Kiryukhantsev-Korneev Ph.V., Bashkirov E.A., Mukanov S.K., Pogozhev Yu.S., Levashov E.A. Protective heterophase coatings produced by electrospark deposition and high-power impulse magnetron sputtering. *Surface Engineering and Applied Electrochemistry*. 2024;60(4):607–617.  
<https://doi.org/10.3103/S1068375524700182>
  - Замулаева Е.И., Кудряшов А.Е., Кирюханцев-Корнеев Ф.В., Башкиров Е.А., Муканов С.К., Погожев Ю.С., Левашов Е.А. Получение защитных гетерофазных покрытий методами импульсной электроискровой и ионно-плазменной обработки. *Электронная обработка материалов*. 2024;60(2):19–30.  
<https://doi.org/10.52577/eom.2024.60.2.19>
  28. Petrzhik M.I., Levashov E.A. Modern methods for investigating functional surfaces of advanced materials by mechanical contact testing. *Crystallography Reports*. 2007;52(6):966–974.  
<https://doi.org/10.1134/S1063774507060065>
  - Петржи́к М.И., Левашов Е.А. Современные методы изучения функциональных поверхностей перспективных материалов в условиях механического контакта. *Кристаллография*. 2007;52(6):1002–1010.
  29. Guo Y., Jia L., Lu W., Zhang H. Morphological heredity of intermetallic  $\text{Nb}_5\text{Si}_3$  dendrites in hypereutectic Nb–Si based alloys via non-equilibrium solidification. *Chinese Journal of Mechanical Engineering*. 2022;35:84.  
<https://doi.org/10.1186/s10033-022-00764-7>
  30. McCaughey C., Tsakirooulos P. Type of primary  $\text{Nb}_5\text{Si}_3$  and precipitation of  $\text{Nb}_{ss}$  in  $\text{Nb}_5\text{Si}_3$  in a Nb–8.3Ti–21.1Si–5.4Mo–4W–0.7Hf (at. %) near eutectic Nb-silicide-based alloy. *Materials*. 2018;11(6):967.  
<https://doi.org/10.3390/ma11060967>
  31. Kiryukhantsev-Korneev Ph.V., Sytchenko A.D., Potanin A.Yu., Vorotilo S.A., Levashov E.A. Mechanical properties and oxidation resistance of Mo–Si–B and Mo–Hf–Si–B coatings obtained by magnetron sputtering in DC and pulsed DC modes. *Surface and Coatings Technology*. 2020; 403:126373.  
<https://doi.org/10.1016/j.surfcoat.2020.126373>

**Information about the Authors**

**Evgenia I. Zamulaeva** – Cand. Sci. (Eng.), Research Scientist, Laboratory “*In situ* diagnostics of structural transformations” of Scientific-Educational Center of Self-Propagating High-Temperature Synthesis (SHS-Center) of MISIS–ISMAN, National University of Science and Technology “MISIS” (NUST MISIS)

 **ORCID:** 0000-0002-1486-4075

 **E-mail:** zamulaeva@gmail.com

**Pavel A. Loginov** – Cand. Sci. (Eng.), Assistant Prof., Senior Researcher, Laboratory “*In situ* diagnostics of structural transformations” of SHS-Center of MISIS–ISMAN, NUST MISIS

 **ORCID:** 0000-0003-2505-2918

 **E-mail:** loginov.pa@misis.ru

**Philipp V. Kiryukhantsev-Korneev** – Dr. Sci. (Eng.), Professor of the Department of powder metallurgy and functional coatings (PM&FC) of NUST MISIS, Head of the Laboratory “*In situ* diagnostics of structural transformations” of SHS-Center of MISIS–ISMAN

 **ORCID:** 0000-0003-1635-4746

 **E-mail:** kiruhancev-korneev@yandex.ru

**Nataliya V. Shvindina** – Scientific Project Engineer, SHS-Center of MISIS–ISMAN, NUST MISIS

 **ORCID:** 0000-0002-4662-544X

 **E-mail:** natali19-03@list.ru

**Mikhail I. Petrzhik** – Dr. Sci. (Eng.), Professor of the Department of PM&FC of NUST MISIS, Leading Researcher of SHS-Center of MISIS–ISMAN

 **ORCID:** 0000-0002-1736-8050

 **E-mail:** petrzhik.mi@misis.ru

**Evgeny A. Levashov** – Dr. Sci. (Eng.), Prof., Corresponding Member of the Russian Academy of Sciences, Head of SHS-Center of MISIS–ISMAN, Head of the Department of PM&FC of NUST MISIS

 **ORCID:** 0000-0002-0623-0013

 **E-mail:** levashov@shs.misis.ru

**Сведения об авторах**

**Евгения Игоревна Замулаева** – к.т.н., науч. сотрудник лаборатории «*In situ* диагностика структурных превращений» Научно-учебного центра (НУЦ) СВС МИСИС–ИСМАН, Национальный исследовательский технологический университет «МИСИС» (НИТУ МИСИС)

 **ORCID:** 0000-0002-1486-4075

 **E-mail:** zamulaeva@gmail.com

**Павел Александрович Логинов** – к.т.н., доцент, ст. науч. сотрудник, лаборатория «*In situ* диагностика структурных превращений», НУЦ СВС МИСИС–ИСМАН, НИТУ МИСИС

 **ORCID:** 0000-0003-2505-2918

 **E-mail:** loginov.pa@misis.ru

**Филипп Владимирович Кирюханцев-Корнеев** – д.т.н., профессор кафедры порошковой металлургии и функциональных покрытий (ПМиФП) НИТУ МИСИС, зав. лабораторией «*In situ* диагностика структурных превращений» НУЦ СВС МИСИС–ИСМАН

 **ORCID:** 0000-0003-1635-4746

 **E-mail:** kiruhancev-korneev@yandex.ru

**Наталия Владимировна Швындина** – инженер научного проекта, НУЦ СВС МИСИС–ИСМАН, НИТУ МИСИС

 **ORCID:** 0000-0002-4662-544X

 **E-mail:** natali19-03@list.ru

**Михаил Иванович Петржик** – д.т.н., профессор кафедры ПМиФП НИТУ МИСИС, вед. науч. сотрудник НУЦ СВС МИСИС–ИСМАН

 **ORCID:** 0000-0002-1736-8050

 **E-mail:** petrzhik.mi@misis.ru

**Евгений Александрович Левашов** – д.т.н., чл.-корр. РАН, проф., директор НУЦ СВС МИСИС–ИСМАН, зав. кафедрой ПМиФП НИТУ МИСИС

 **ORCID:** 0000-0002-0623-0013

 **E-mail:** levashov@shs.misis.ru

**Contribution of the Authors**

**E. I. Zamulaeva** – developed the main concept, defined the aim and objectives of the study, deposited the ESD coatings, and prepared the manuscript.

**P. A. Loginov** – performed TEM analysis and interpreted the experimental data.

**Ph. V. Kiryukhantsev-Korneev** – deposited the HiPIMS coatings and carried out GDOES analysis

**N. V. Shvindina** – conducted SEM studies and participated in the discussion of the results.

**M. I. Petrzhik** – performed mechanical testing and contributed to experimental planning.

**E. A. Levashov** – reviewed and edited the manuscript and contributed to formulating the conclusions.

**Вклад авторов**

**Е. И. Замулаева** – формирование основной концепции, постановка цели и задачи исследования, осаждение ЭИО-покрытий, подготовка текста статьи.

**П. А. Логинов** – проведение ПЭМ, анализ экспериментальных данных.

**Ф. В. Кирюханцев-Корнеев** – осаждение ВИМР-покрытий, проведение ОЭСТР.

**Н. В. Швындина** – проведение экспериментов по СЭМ, участие в обсуждении результатов.

**М. И. Петржик** – проведение механических испытаний, планирование экспериментов.

**Е. А. Левашов** – рецензирование и редактирование текста, формулировка выводов.

Received 14.04.2025

Revised 15.04.2025

Accepted 16.04.2025

Статья поступила 14.04.2025 г.

Доработана 15.04.2025 г.

Принята к публикации 16.04.2025 г.



UDC 621.793.18

<https://doi.org/10.17073/1997-308X-2025-3-60-73>

Research article  
Научная статья



# Structure and properties of antifriction Ti–Cr–Ni–Cu–Sn–P–C–N coatings deposited by magnetron sputtering of composite SHS targets

Ph. V. Kiryukhantsev-Korneev<sup>✉</sup>, A. D. Chertova<sup>✉</sup>,  
Yu. S. Pogozev, E. A. Levashov

National University of Science and Technology “MISIS”  
1 Bld, 4 Leninskiy Prosp, Moscow 119049, Russia

✉ [kiruhancev-korneev@yandex.ru](mailto:kiruhancev-korneev@yandex.ru); [alina-sytchenko@yandex.ru](mailto:alina-sytchenko@yandex.ru)

**Abstract.** This article focuses on the production of wear-resistant antifriction coatings by magnetron sputtering using composite SHS-fabricated cathode targets of TiCrNiC and TiCrNiC–CuSnP in Ar and Ar + 15 % N<sub>2</sub> atmospheres. Special attention is given to the phase composition and structure of the targets, produced via the self-propagating high-temperature synthesis (SHS) method. Structural characterization of the targets and coatings was carried out using X-ray diffraction (XRD), scanning electron microscopy (SEM), energy-dispersive spectroscopy (EDS), and glow discharge optical emission spectroscopy (GDOES). The mechanical and tribological properties of the coatings were evaluated using nanoindentation, scratch testing, and pin-on-disk sliding wear tests. The resulting coatings exhibited dense, defect-free microstructures with a uniform elemental distribution through the thickness. The coating matrix was primarily composed of FCC phases *c*-TiC(N) and *c*-(Ni,Cr). The addition of copper to the coating led to the formation of an additional amorphous Cu-based phase. The coatings demonstrated hardness in the range of 18–21 GPa and an elastic modulus of 220–235 GPa. High critical loads for adhesive failure were observed, reaching up to 60 N. The non-reactive Ti–Cr–Ni–C coatings exhibited the lowest friction coefficients (0.17–0.18), while other compositions showed values ranging from 0.22 to 0.25, in contrast to 0.63–0.71 for uncoated steel substrates. The specific wear rate varied between  $1.1 \cdot 10^{-6}$  and  $5.0 \cdot 10^{-6}$  mm<sup>3</sup>/(N·m) depending on the counterbody material and coating composition, which is nearly two orders of magnitude lower than that of the substrate material ( $(1.2 \div 2.7) \cdot 10^{-4}$  mm<sup>3</sup>/(N·m)).

**Keywords:** titanium carbide, magnetron sputtering, composite SHS targets, antifriction coatings, friction coefficient, wear resistance

**Acknowledgements:** This work was financially supported by the Ministry of Science and Higher Education of the Russian Federation under State Assignment No. FSME-2025-0003.

The authors are grateful to M.I. Petrzhik and M.Ya. Bychkova for their assistance with the mechanical and tribological testing of the coatings.

**For citation:** Kiryukhantsev-Korneev Ph.V., Chertova A.D., Pogozev Yu.S., Levashov E.A. Structure and properties of antifriction Ti–Cr–Ni–Cu–Sn–P–C–N coatings deposited by magnetron sputtering of composite SHS targets. *Powder Metallurgy and Functional Coatings*. 2025;19(3):60–73. <https://doi.org/10.17073/1997-308X-2025-3-60-73>

# Структура и свойства антифрикционных покрытий в системе Ti–Cr–Ni–Cu–Sn–P–C–N, полученных методом магнетронного распыления композиционных СВС-мишеней

Ф. В. Кирюханцев-Корнеев <sup>✉</sup>, А. Д. Чертова <sup>✉</sup>,

Ю. С. Погожев, Е. А. Левашов

Национальный исследовательский технологический университет «МИСИС»  
Россия, 119049, г. Москва, Ленинский пр-т, 4, стр. 1

✉ kiruhancev-korneev@yandex.ru; alina-sytchenko@yandex.ru

**Аннотация.** Статья посвящена получению антифрикционных износостойких покрытий методом магнетронного распыления с использованием композиционных катодов-мишеней TiCrNiC и TiCrNiC–CuSnP в среде Ar и Ar + 15 % N<sub>2</sub>. Отдельное внимание уделено изучению фазового состава и структуры мишеней, изготовленных с применением метода самораспространяющегося высокотемпературного синтеза (СВС). Структурные исследования мишеней и покрытий выполнены методами рентгенофазового анализа, растровой электронной микроскопии, энергодисперсионной спектроскопии и оптической эмиссионной спектроскопии тлеющего разряда. Механические и трибологические свойства покрытий измерены с использованием методов наноиндентирования, скратч-тестирования и измерительного скольжения. Установлено, что полученные покрытия обладали плотной малодефектной структурой с равномерным распределением элементов по толщине. Основу покрытий составляли ГЦК-фазы *c*-TiC(N) и *c*-(Ni,Cr). При введении в состав покрытий меди формировалась дополнительная аморфная фаза на ее основе. Покрытия обладали твердостью в диапазоне 18–21 ГПа и модулем упругости на уровне 220–235 ГПа, а также характеризовались высокой критической нагрузкой адгезионного разрушения до 60 Н. Минимальный коэффициент трения 0,17–0,18 демонстрировали нереакционные покрытия Ti–Cr–Ni–C, для остальных составов его значения находились в интервале от 0,22 до 0,25, в то время как у стальных подложек без покрытия этот показатель составлял 0,63–0,71. Величина приведенного износа, в зависимости от материала используемых контртел и составов покрытий, изменялась от  $1,1 \cdot 10^{-6}$  до  $5,0 \cdot 10^{-6}$  мм<sup>3</sup>/(Н·м), что почти на два порядка ниже, чем у материала подложки:  $(1,2 \div 2,7) \cdot 10^{-4}$  мм<sup>3</sup>/(Н·м).

**Ключевые слова:** карбид титана, магнетронное распыление, композиционные СВС-мишени, антифрикционные покрытия, коэффициент трения и износостойкость

**Благодарности:** Работа выполнена при финансовой поддержке Министерства науки и высшего образования РФ в рамках государственного задания (проект № FSME-2025-0003).

Авторы признательны М.И. Петрику и М.Я. Бычковой за помощь в проведении механических и трибологических испытаний покрытий.

**Для цитирования:** Кирюханцев-Корнеев Ф.В., Чертова А.Д., Погожев Ю.С., Левашов Е.А. Структура и свойства антифрикционных покрытий в системе Ti–Cr–Ni–Cu–Sn–P–C–N, полученных методом магнетронного распыления композиционных СВС-мишеней. *Известия вузов. Порошковая металлургия и функциональные покрытия*. 2025;19(3):60–73.

<https://doi.org/10.17073/1997-308X-2025-3-60-73>

## Introduction

As the potential of consolidated materials has been largely exhausted, the development of new high-performance engineering systems is no longer possible without surface modification technologies and the use of functional coatings. Today, considerable attention is focused on the design of coatings for protecting critical components operating in aggressive liquid and gaseous environments and under various wear conditions. Among the most promising are titanium carbide and carbonitride-based coatings, which exhibit high hardness, wear and corrosion resistance, and pronounced antifricion properties [1–3].

By adjusting the stoichiometry of TiCN coatings, it is possible to tailor their mechanical and tribological performance by controlling the structural type, internal stresses, and the concentration of free carbon, which acts as a solid lubricant in the tribological contact zone [4; 5]. At a C/N ratio close to 1, record hardness values of up to 45 GPa have been reported, attributed to significant compressive stresses (–6 GPa) arising from distortions in the FCC lattice structure [6]. In contrast, coatings with an elevated carbon content (C/N = 5.6) achieved a friction coefficient of ~0.1 [5]. In these coatings, carbon atoms formed amorphous intergranular layers along TiCN crystallite boundaries, resulting in a nanocomposite structure described

as  $nc$ -TiCN/ $a$ -C, where  $nc$  denotes nanocrystallites and  $a$  the amorphous phase.

The performance of TiCN coatings can be further enhanced by the addition of metallic elements [7–12]. For instance, aluminum improves both wear and oxidation resistance [7; 8], while nickel and chromium exhibit similar effects [9; 10]. These improvements are attributed to the formation of dense oxide films on the coating surface during heating in air, which inhibit oxygen penetration into the bulk material.

In recent years, copper-based coatings have attracted growing interest [13–15] due to copper’s relatively low friction coefficient and high thermal conductivity, which is crucial for efficient heat dissipation from the contact zone. Copper can be introduced either in its pure form or as part of brass or bronze alloys, offering excellent antifriction performance at relatively low cost [16]. Notably, the incorporation of ductile metals into ceramic matrices underpins the concept of nanocomposite superhard coatings (hardness >40 GPa), as proposed by the author in [17]. This concept involves the formation of  $nc$ -MeN/metal structures (where Me = Ti, Cr, Zr, etc., and metal = Cu, Ni, Fe, etc.), with the MeN phase consisting of nanocrystallites and the metallic phase being  $X$ -ray amorphous. Furthermore, all grains are expected to exhibit a preferred orientation [17; 18]. Subsequent research extended this concept to carbide-based systems such as Ti–Cu–C [19], and nanocomposite  $nc$ -TiCN/ $a$ -Cu coatings with a hardness of 37 GPa were reported in [20].

Various methods can be used to deposit titanium carbide and carbonitride coatings, including those alloyed with transition metals. These methods include plasma spraying [21], electric arc cladding [22], laser cladding [23], electro-spark deposition [11; 24; 25], chemical vapor deposition [26], vacuum cathodic arc evaporation [27], and pulsed laser deposition [28]. Among these, magnetron sputtering stands out as a highly promising technique, allowing the deposition of wear-resistant and antifriction coatings across a broad compositional range. The method yields coatings with low impurity levels, minimal defects, and smooth surfaces that require no post-processing [1; 12; 29–31]. The capabilities of magnetron sputtering are further enhanced when multicomponent ceramic targets produced via self-propagating high-temperature synthesis (SHS) are used [32; 33]. This approach ensures that the atomic flux from the cathode to the substrate contains all necessary metallic and non-metallic elements, providing high compositional homogeneity across the coating thickness. A promising material for fabricating SHS-based sputtering targets is the STIM-3B alloy (Ti–Cr–C–Ni system), whose combustion and structure formation mechanisms have been studied in

detail [34]. Tin–phosphor bronze powder can also be used as an alloying addition in target preparation.

The aim of this study was to develop tribological coatings of Ti–Cr–Ni–C–(N) and Ti–Cr–Ni–Cu–Sn–P–C–(N) compositions by magnetron sputtering using multicomponent SHS targets in Ar and Ar–N<sub>2</sub> atmospheres. Particular emphasis was placed on the synthesis of targets with tailored compositions.

## Materials and methods

The starting materials used for fabricating the cathode targets were titanium powder (Ti) grade PTS (<60 μm), chromium powder (Cr) grade PX-1S (<63 μm), nickel powder (Ni) grade PNK-OT2 (<71 μm), technical carbon black (C) grade P804-T with a specific surface area of 15 m<sup>2</sup>/g, graphite powder (C<sub>gr</sub>) grade MG-1, and tin-phosphor bronze alloy powder (BrOF grade; composition: Cu–7.8 wt. % Sn–0.48 wt. % P; particle size 100–200 μm). The compositions of the reactive mixtures for SHS-based target synthesis were calculated assuming complete chemical transformation according to the following equation

$$[70.775 \% (\text{Ti} + \text{C}) - 19.475 \% (3\text{Cr} + 2\text{C}) - 5 \text{ wt. \% C}_{\text{gr}} - 4.75 \text{ wt. \% Ni}] + X \% \text{ Bronze},$$

where  $X$  is the bronze content in the charge, set to 0 or 20 wt. %. The compositions of the powder mixtures are summarized in Table 1.

Before mixing, all starting powders were dried at 100 °C for 24 h. Mixing was performed in a 3 L rotary ball mill for 8 h using cemented carbide grinding balls at a powder-to-ball mass ratio of 1:8.

The adiabatic combustion temperature ( $T_c^{\text{ad}}$ ), as well as the equilibrium phase composition and the physical state of the SHS products at  $T_c^{\text{ad}}$ , were calculated

Table 1. Experimental compositions of initial powder mixtures

Таблица 1. Экспериментальные составы исходных порошковых смесей

Element	$X = 0$		$X = 20$	
	wt. %	at. %	wt. %	at. %
Ti	48.44	28.14	38.75	25.52
C	20.02	46.37	16.02	42.05
C <sub>gr</sub>	5.00	11.58	4.00	10.50
Cr	21.79	11.66	17.43	10.57
Ni	4.75	2.25	3.80	2.04
Bronze	–		20.00	9.32

using the THERMO software package [35]. Composite cathode targets of TiCrNiC and TiCrNiC–CuSnP with dimensions diameter 120 mm × 10 mm were produced using pressure-assisted self-propagating high-temperature synthesis SHS, as described in [33].

The powder mixtures were pre-compacted to 60 % of theoretical density in a steel cylindrical mold at 70 atm. The green compacts were further dried in a vacuum oven at 100 °C for 4 h to remove residual moisture and adsorbed gases. The key parameters for SHS under pressure were as follows: applied pressure – 200 atm; ignition delay – 1 s; dwell time under pressure – 5 s. The synthesis was carried out in a sand mold using a DA-1532B hydraulic press. The resulting billets were then ground and shaped to the required dimensions using EDM cutting.

The phase composition of the synthesized samples was analyzed using a DRON 4-07 X-ray diffractometer (Russia) with monochromatic  $\text{CuK}_\alpha$  radiation. Scans were collected pointwise over a  $2\theta$  range of 10–110°, with a step size of 0.1° and exposure time of 3 s per step. The microstructure was examined using a scanning electron microscope (SEM) S-3400N (Hitachi, Japan) equipped with a NORAN 7 EDS system (Thermo Scientific, USA), operated at accelerating voltages of 5–20 kV.

Coating deposition was performed using a UVN-2M vacuum unit equipped with gas inlets, a substrate positioning system, a slit-type ion source, and two magnetrons powered by Advanced Energy DC Pinnacle Plus units (USA), as described in [36]. Substrates included diameter 30 mm disks of SCM440 steel (equivalent to 40KhFA steel) for mechanical and tribological testing, and VK6M cemented carbide for compositional and adhesion strength analysis. The substrates were polished using a Struers RotoPol-21 system (Denmark). Surface cleaning was performed in an ultrasonic disperser using sequential treatments with gasoline, solvent, and isopropanol. Additionally, model substrates of monocrystalline silicon KÉF-4.5 (100) (Elma, Russia), sized 15×15 mm, were coated for structural analysis. Both base and model substrates were coated under identical conditions. Prior to deposition, substrates were cleaned using ion etching (0.03 Pa, 2 kV, 60 mA,  $\text{Ar}^+$  ions). During coating deposition, the magnetron current was 1.5 A, the voltage 500 V, the power supply frequency 50 kHz, the bias voltage –50 V, the working pressure 0.2 Pa, and the process duration was 10 min. The nitrogen content in the  $\text{Ar} + \text{N}_2$  gas mixture (gas purity 99.999 %) was varied between 0 and 15 %.

The compact ceramics and coatings were examined by scanning electron microscopy (SEM) and

energy-dispersive spectroscopy (EDS) using an S-3400 microscope (Hitachi, Japan) equipped with a Noran 7 spectrometer (Thermo Scientific, USA). X-ray diffraction (XRD) analysis of the ceramic specimens was performed using a DRON 4-07 diffractometer (Russia), while coatings were analyzed using a D8 Advance diffractometer (Bruker, Germany). Diffraction data were collected using monochromatized  $\text{CuK}_\alpha$  radiation with a step size of 0.1° and an exposure time of 10 s per step; the total scan duration was 1 h. Phase identification was carried out using the EVA software package and the PDF2 international database. The elemental composition of the coatings and their depth distribution profiles were determined using glow discharge optical emission spectroscopy (GDOES) on a Profiler-2 spectrometer (Horiba Jobin Yvon, France) [37].

Hardness ( $H$ ) and elastic modulus ( $E$ ) of the coatings were determined by nanoindentation using a Nano-Hardness Tester (CSM Instruments, Switzerland) with a Berkovich indenter, at loads of 4–8 mN, loading rates of 8–16 mN/min, and a dwell time of 5 s. Calculations were based on the Oliver–Pharr method. Scratch testing was conducted in accordance with ASTM C1624-05 using a Revetest system (CSM Instruments, Switzerland) equipped with a Rockwell C-type diamond conical indenter (tip radius 200  $\mu\text{m}$ ). The maximum load was 60 N, loading rate 59 N/min, scratch length 5 mm, and optical magnification 200 $\times$  and 800 $\times$ . The minimum critical failure loads corresponding to the onset of cracking ( $L_{c1}$ ), the first spallation event ( $L_{c2}$ ), and indenter contact with the substrate ( $L_{c3}$ ) were identified.

The coefficient of friction ( $f$ ) was measured using a Tribometer (CSM Instruments, Switzerland) following the ASTM G99-95 standard in a pin-on-disk configuration. Test parameters: normal load – 5 N; linear velocity – 10 cm/s; wear track radius – 8–10 mm; total sliding distance – 1100 m (30 m for 40KhFA steel substrate). Counterbodies were 6 mm radius pins made of SKH51 (analogous to R6M5) or SKD11 (analogous to Kh12MF) tool steels. Wear tracks and counterbody surfaces were examined using a WYKO NT1100 optical profilometer (Veeco, USA) and an MBS-9 optical microscope (Lytkarino Optical Glass Factory, JSC, Russia), respectively.

## Results and discussion

### Composition and structure of SHS targets

Table 2 presents the calculated adiabatic combustion temperature ( $T_c^{\text{ad}}$ ) and the equilibrium composition of combustion products at room-temperature initial

conditions. It can be seen that an increase in the bronze content of the charge (parameter  $X$ ) leads to a decrease in combustion temperature. This is evidently due to the reduced heat contribution from the TiC formation reaction and additional thermal losses associated with heating and melting the bronze.

The calculated  $T_c^{ad}$  values for the system under study indicate that the process should occur in a self-sustained combustion mode. The adiabatic combustion temperature exceeds the melting points of titanium (1941 K), nickel (1728 K), and bronze (1358 K), which implies that carbon will dissolve in the resulting melt within the combustion front. As the melt becomes saturated with carbon, crystals of titanium and chromium carbides will begin to form, along with the crystallization of nickel and bronze, with possible mutual solubility between them.

The results of XRD analysis for the synthesized compact materials are shown in Fig. 1 and Table 3. The samples contain titanium carbide with a lattice parameter significantly lower than the reference value for standard TiC powder (0.4315 nm) [38], which is attributed to the dissolution of chromium carbide into the TiC lattice. The phase composition also includes chromium carbide  $Cr_3C_2$  and nickel (Ni) with dissolved Cr and Ti, as evidenced by peak shifts in the diffraction patterns. Unreacted graphite is also present – unlike carbon black, it does not fully dissolve in the melt over the course of the process due to slower dissolution kinetics. The excess carbon in the deposited coatings is expected to act as a solid lubricant, reducing the coefficient of friction. The presence of bronze in the  $X = 20$  sample is confirmed by the appearance of Cu reflections in the diffraction pattern (Fig. 1, *b*). The absence of distinct Ni peaks is likely due to its dissolution in the bronze melt during the SHS process.

The SEM images of the cross-sections of synthesized ceramics with compositions  $X = 0$  and  $X = 20$  are shown in Fig. 2.

**Table 2. Calculated adiabatic combustion temperature and equilibrium composition of combustion products assuming room-temperature initial components**

**Таблица 2. Расчетные адиабатическая температура горения и равновесный состав продуктов горения при комнатной начальной температуре исходных компонентов**

Mixture composition	$T_c^{ad}$ , K	Combustion product composition, wt. %				
		TiC	$Cr_3C_2$	Ni	C	Bronze
$X = 0$	2452	67.24	18.50	4.75	9.51	–
$X = 20$	2103	49.08	20.37	3.85	6.70	20.00

The microstructure of the  $X = 0$  sample included TiC with dissolved Cr, chromium carbide  $Cr_3C_2$ , nickel (Ni), and graphite. In the  $X = 20$  sample, additional copper-rich layers were observed, with nickel dissolved in them without the formation of a distinct Ni

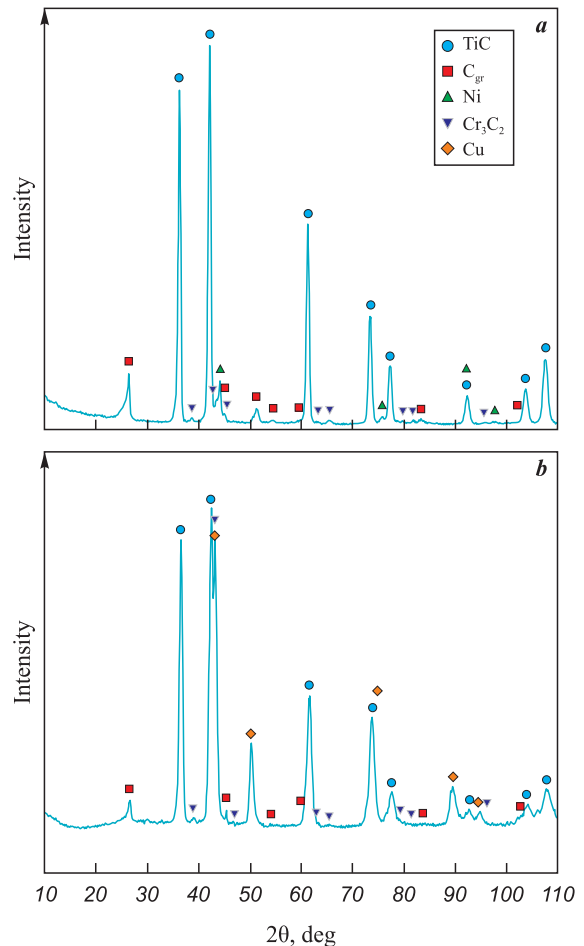


**Fig. 1. XRD patterns of compact ceramics with  $X = 0$  (a) and  $X = 20$  (b) compositions**

**Рис. 1. Дифрактограммы компактной керамики составов  $X = 0$  (a) и  $X = 20$  (b)**

**Table 3. Phase composition of compact ceramics of  $X = 0$  and  $X = 20$  compositions**

**Таблица 3. Фазовый состав компактной керамики составов  $X = 0$  и  $X = 20$**

Phase	Structure type	$X = 0$		$X = 20$	
		Content, wt. %	Lattice parameter $a$ , nm	Content, wt. %	Lattice parameter $a$ , nm
TiC	<i>cF8/2</i>	79	0.4271	68	0.4269
$C_{gr}$	<i>hP4/1</i>	14	–	7	–
Ni	<i>cF4/1</i>	3	0.3547	–	
$Cr_3C_2$	<i>oC20/7</i>	4	–	1	–
Cu	<i>cF4/1</i>	–		24	0.3632

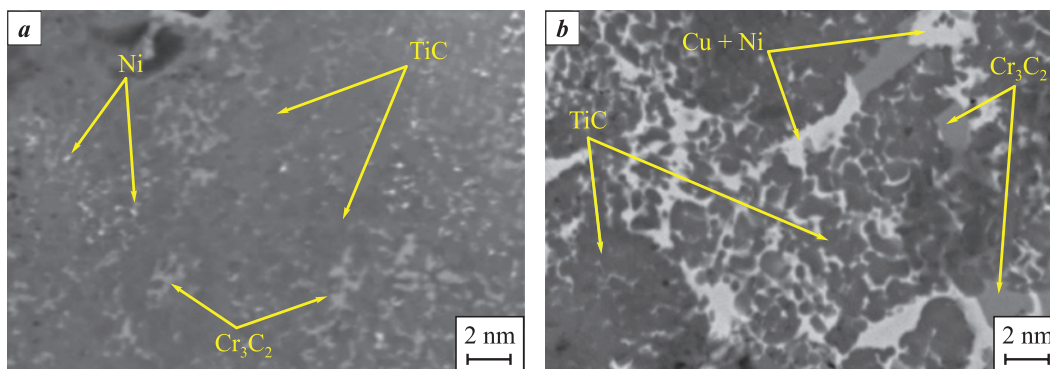


Fig. 2. Microstructure of synthesized ceramics with compositions  $X = 0$  (a) and  $X = 20$  (b)

Рис. 2. Микроструктура синтезированной керамики  $X = 0$  (a) и  $X = 20$  (b)

phase. The average grain size of the primary carbide phase was approximately 3  $\mu\text{m}$ .

### Composition, structure, and properties of the coatings

Coating 1 consisted of (at. %): 22.2 Ti, 65.3 C, 10.2 Cr, and 2.3 Ni. Introducing nitrogen into the gas atmosphere (coating 2) resulted in a nitrogen concentration increase from 0 to 26.3 at. %, accompanied by a reduction in carbon content to 45.7 at. % (Table 4). The concentrations of the remaining elements decreased by approximately 15–20 %. Coatings 3 and 4, which were alloyed with bronze, contained, in addition to the main elements, the following (at. %): 12.0 Cu, 0.4 Sn, and 0.3 P (coating 3); and 9.6 Cu, 0.4 Sn, and 0.1 P (coating 4).

It is important to note that energy-dispersive X-ray spectroscopy (EDS), while widely used for elemental analysis, is highly sensitive to surface topography and may produce inaccurate results for light elements such as C, N, and O. To obtain more reliable data, glow discharge optical emission spectroscopy (GDOES) was employed. This method allows accurate determination of both metallic and non-metallic elements [37].

The GDOES analysis demonstrated that all elements are uniformly distributed across the coating thickness (Fig. 3).

A slight decrease in signal intensity was observed at the surface of the coatings, which may be attributed to surface contamination, the presence of adsorbed gases, and the formation of a natural oxide film. The gradual rise in substrate signal is due to increased surface roughness resulting from ion etching carried out prior to deposition. According to the GDOES results, the elemental composition of the coatings was as follows (at. %): 31.4 Ti, 52.1 C, 3.5 Ni, 13.0 Cr (coating 1); 23.0 Ti, 37.0 C, 2.5 Ni, 9.0 Cr, 28.5 N (coating 2); 27.5 Ti, 46.5 C, 3.8 Ni, 10.5 Cr, 11.7 Cu (coating 3); 22.8 Ti, 33.7 C, 2.7 Ni, 8.0 Cr, 9.4 Cu, 23.4 N (coating 4).

The atomic Ti/C ratio in the SHS targets was 0.48, while in the resulting coatings it increased to 0.59–0.68. This reduction in the carbon atom concentration in the coating, compared to that in the target is likely due to the higher scattering cross-section of carbon atoms compared to heavier titanium atoms in the plasma during deposition [39]. As shown below, the GDOES results are consistent with the XRD data.

The coating thicknesses determined from the GDOES profiles, along with the calculated deposition rates, are summarized in Table 4. For coatings 1 and 2 – deposited from SHS targets without bronze – the thickness and deposition rate were similar, measuring 2.0  $\mu\text{m}$  and 91 nm/min, respectively. The use of bronze-containing targets resulted in a 10–15 %

Table 4. Elemental composition, thickness, and deposition rate of the coatings

Таблица 4. Элементный состав, толщина и скорость роста покрытий

Coating	Target	Gas atmosphere	Concentration, at. %								Thickness, $\mu\text{m}$	Deposition rate, nm/min
			Ti	C	Cr	Ni	Cu	Sn	P	N		
1	X = 0	Ar	22.2	65.3	10.2	2.3	0	0	0	0	2.0	91
2		Ar + N <sub>2</sub>	17.8	45.7	8.3	1.9	0	0	0	26.3	2.0	91
3	X = 20	Ar	20.9	54.0	9.1	3.3	12.0	0.4	0.3	0	2.2	100
4		Ar + N <sub>2</sub>	16.7	44.4	7.2	2.0	9.6	0.4	0.1	19.6	2.3	105

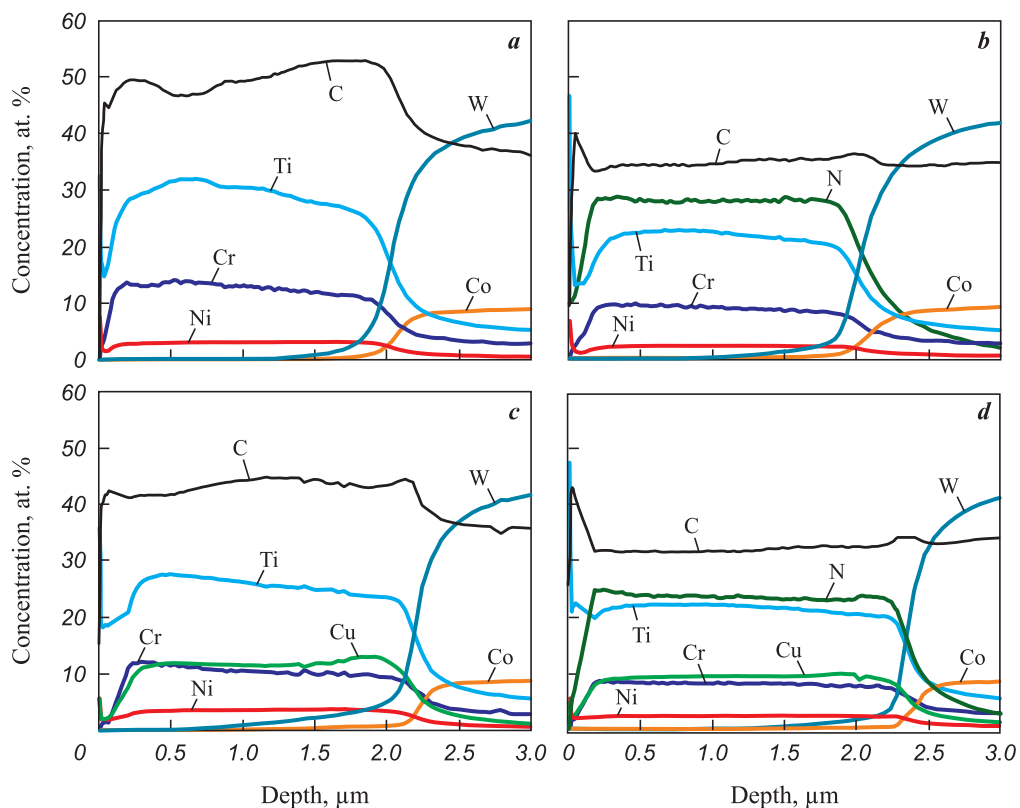


Fig. 3. GDOES depth distribution profiles of coatings 1 (a), 2 (b), 3 (c), and 4 (d)

Рис. 3. ОЭСТР-профили покрытий 1 (a), 2 (b), 3 (c) и 4 (d)

increase in both coating thickness and deposition rate. This effect can be attributed to the higher electrical conductivity ( $5.8 \cdot 10^7$  S/m) [40] and sputtering yield (3–6 atoms/ion) [41] of copper compared to titanium carbide ( $3.0 \cdot 10^7$  S/m and 0.5–1.0 atoms/ion) [42; 43]. It is worth noting that the reduction in deposition rate typically observed in reactive sputtering [44; 45] during transitions from conditions 1 → 2 and 3 → 4 was not observed in this study.

Typical SEM images of coating fracture surfaces are shown in Fig. 4, a. All coatings exhibited a dense, defect-free structure with no pronounced columnar features typically observed in TiC-based ion-plasma coatings [46; 47]. It is important to note that the presence of columnar grains in the structure generally has a detrimental effect on the mechanical and tribological properties of coatings [48].

The diffraction patterns of the coatings are shown in Fig. 4, b. The main structural component of all coatings was the face-centered cubic (FCC) *c*-TiC phase (ICDD 31-1400). The crystallite size of this phase, calculated using the Scherrer equation for the most intense (200) reflection, was 36, 34, 32, and 29 nm for coatings 1 through 4, respectively. The lattice parameter (*a*) of the *c*-TiC phase ranged from 0.433 to 0.434 nm, which is consistent with the standard

powder reference. Reflections at  $2\theta = 44.2^\circ$  and  $51.5^\circ$  correspond to a solid solution of nickel and chromium, *c*-(Ni,Cr) (ICDD 77-7616). For coatings 1 and 2, the crystallite size of this phase was similar, falling within the range of 22–23 nm. The addition of bronze to both non-reactive and reactive coatings led to a reduction in the crystallite size of the *c*-(Ni,Cr) (111) phase to 15 nm in coating 3 and 8 nm in coating 4. In coatings 3 and 4, which were alloyed with bronze, an additional peak was detected at approximately  $2\theta \sim 43^\circ$ , close to the position characteristic of copper (*c*-Cu, ICDD 04-0836). The pronounced peak broadening and the absence of other copper reflections suggest that copper is predominantly present in an amorphous state, forming intergranular layers that separate the crystallites of the primary phase and hinder their coalescence during growth [17–19].

Scratch testing results are presented in Fig. 5, and the critical load values  $L_{c1}$  and  $L_{c2}$  are summarized in Table 5.

Coating 1 demonstrated the highest critical loads, with  $L_{c1} = 26.5$  N and  $L_{c2} > 60$  N. For coating 2, the onset of cracking and the first spallation event – accompanied by fluctuations in acoustic emission and the coefficient of friction – occurred at a load of 15.7 N. Coating 3 exhibited the lowest crack resistance, with

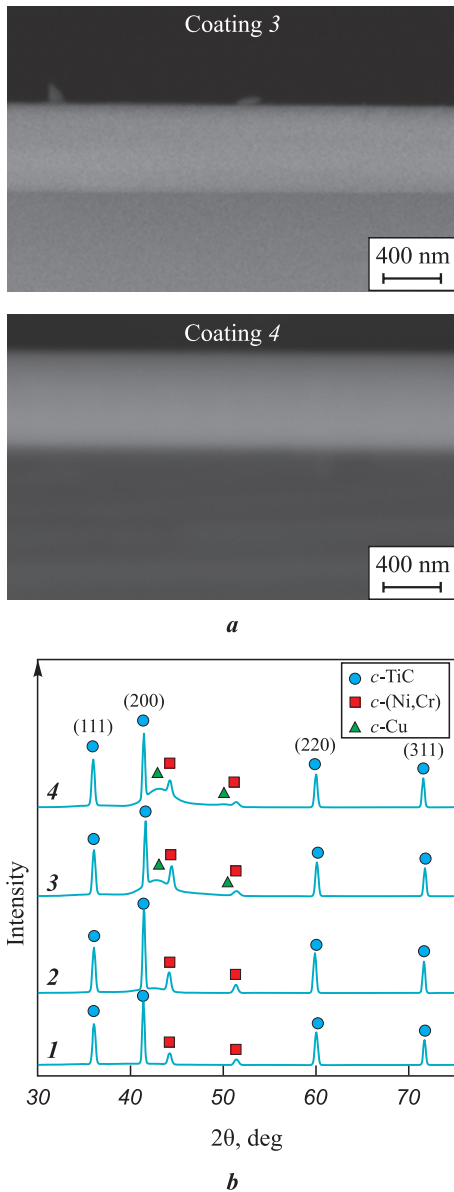


Fig. 4. SEM images of cross-sectional fracture surfaces of coatings 3 and 4 (a), and XRD patterns of coatings 1–4 (b)

Рис. 4. СЭМ-изображения поперечных изломов покрытий 3 и 4 (a) и рентгенограммы покрытий 1–4 (b)

$L_{c1} = 2.6$  N, although no spallation was observed over the entire load range. Coating 4 showed  $L_{c1} = 19.9$  N and  $L_{c2} > 21$  N. For all coatings, no indenter contact with the substrate was observed, indicating that the  $L_{c3}$  value exceeded 60 N. Overall, coating 1 exhibited the best performance in terms of crack resistance and adhesion strength.

Nanoindentation tests revealed that the coatings had hardness values in the range of  $H = 18\div 21$  GPa and elastic moduli of  $E = 220\div 235$  GPa. The  $H/E$  ratio, which reflects the coating's resistance to elastic strain to failure, and the  $H^3/E^2$  ratio, indicative of resistance to plastic deformation, were calculated

to assess potential tribological behavior [49; 50]. Coating 2 showed the highest values of  $H/E = 0.090$  and  $H^3/E^2 = 0.174$  GPa. Coatings 1, 3, and 4 displayed similar  $H/E$  values of 0.082–0.083 and  $H^3/E^2$  values of 0.122–0.132 GPa. The relatively moderate hard-

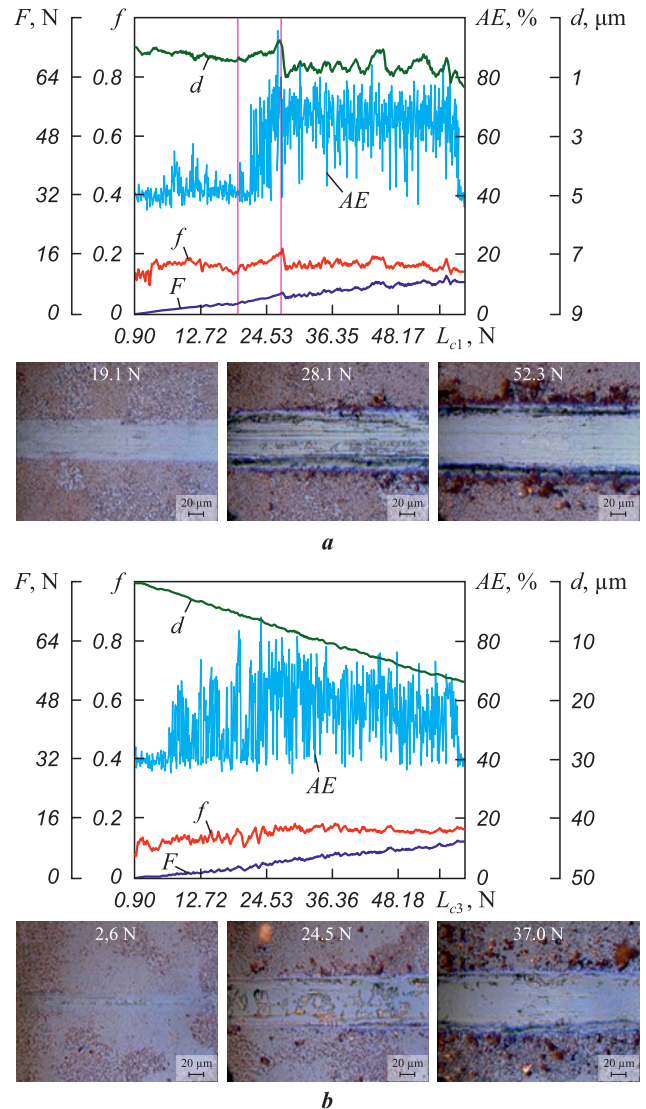


Fig. 5. Scratch testing results for coatings 1 (a) and 3 (b)

Рис. 5. Результаты скрач-тестирования покрытий 1 (a) и 3 (b)

Table 5. Mechanical properties of coatings  
Таблица 5. Механические характеристики покрытий

Coating	$L_{c1}$ , N	$L_{c2}$ , N	H, GPa	E, GPa	H/E	$H^3/E^2$ , GPa
1	26.5	>60.0	18	221	0.083	0.127
2	15.7	15.7	21	234	0.090	0.174
3	2.6	>60.0	19	235	0.082	0.132
4	19.9	>21.0	18	220	0.082	0.122

ness of the coatings may be attributed to the presence of an excess carbon-rich phase [4]. This is supported by atomic ratios of  $(Ti + Cr)/C = 0.82\text{--}0.85$  for coatings 1 and 3 and  $(Ti + Cr)/(C + N) = 0.49\text{--}0.54$  for coatings 2 and 4.

Tribological tests showed that the uncoated steel substrate exhibited the highest average coefficients of friction,  $f_{avg} = 0.63$  and  $0.71$ , in contact with SKH51 and SKD11 steel counter bodies, respectively (Fig. 6, Table. 6). Coating 1 had the lowest friction coefficient,  $f = 0.17 \div 0.18$ , likely due to its high carbon concentration (approximately 50 at. %). Coatings 2, 3, and 4 showed friction coefficients in the range of 0.22–0.25 with both counter body types. It is noteworthy that nitrogen alloying of coating 1 resulted in a 20 % increase in the coefficient of friction.

An increase in the friction coefficient following nitrogen incorporation into TiC-based coatings was

previously reported in [51] and was attributed to structural modification and a decrease in carbon content. Copper addition, in turn, led to a 40 % and 10 % increase in the friction coefficient of Ti–Cr–Ni–C and Ti–Cr–Ni–C–N coatings, respectively. A similar rise in the friction coefficient upon copper incorporation was observed earlier for TiCN and TiAlSiN coatings [52; 53]. The authors of those studies attributed this effect to the adverse impact of the brittle  $Cu_2O$  phase that forms during sliding.

Fig. 7 shows two-dimensional wear track profiles and micrographs of the counter body surfaces after tribological tests of the coatings and substrate. The wear depth of the substrate exceeded that of the coatings by factors of 1.5–7.0 and 2.0–10.0 when using SKH51 and SKD11 counter bodies, respectively.

Wear track analysis revealed that the 40KhFA steel substrate exhibited a specific wear rate

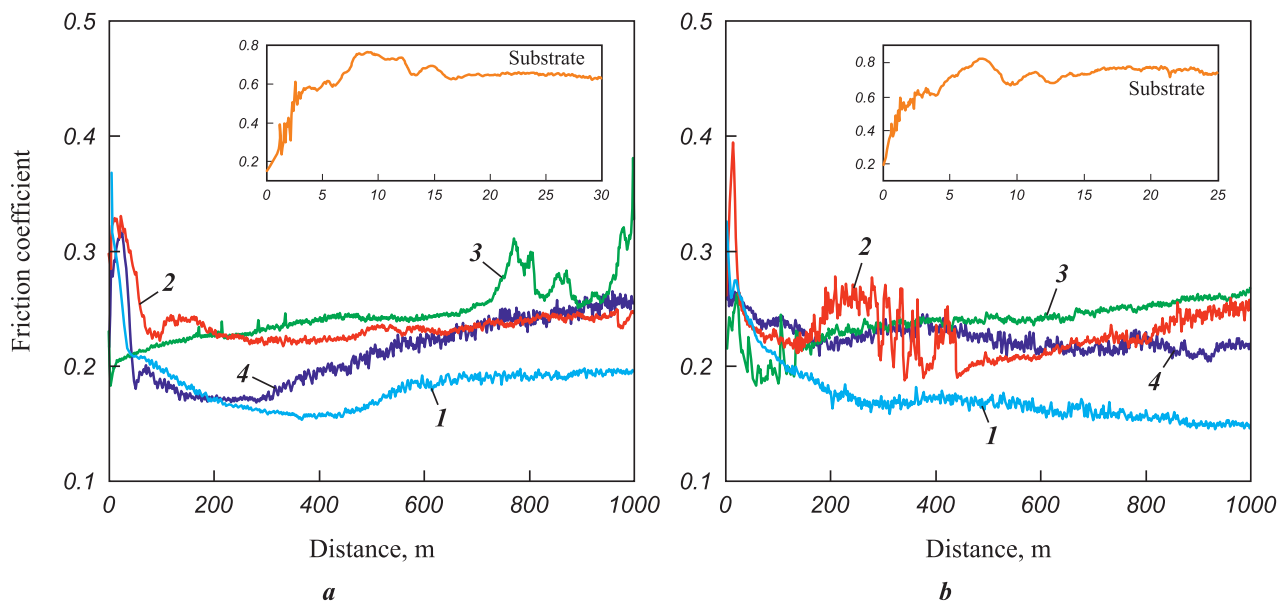


Fig. 6. Friction coefficient as a function of sliding distance in tests against SKH51 (a) and SKD11 (b) counter bodies

Рис. 6. Зависимости коэффициента трения от дистанции при испытаниях в паре с контртелами Р6М5 (а) и Х12МФ (б)

Table 6. Friction coefficient and specific wear rate for uncoated substrate and coatings

Таблица 6. Коэффициент трения и приведенный износ для непокрытой подложки и покрытий

Coating	SKH51 counter body			SKD11 counter body		
	$f$	$V_{coat}, mm^3/(N \cdot m)$	$V_{ball}, mm^3/(N \cdot m)$	$f$	$V_{coat}, mm^3/(N \cdot m)$	$V_{ball}, mm^3/(N \cdot m)$
1	0.18	$1.4 \cdot 10^{-6}$	$5.4 \cdot 10^{-8}$	0.17	$1.2 \cdot 10^{-6}$	$2.4 \cdot 10^{-7}$
2	0.22	$1.3 \cdot 10^{-6}$	$7.3 \cdot 10^{-8}$	0.22	$1.1 \cdot 10^{-6}$	$2.9 \cdot 10^{-7}$
3	0.25	$5.0 \cdot 10^{-6}$	$3.0 \cdot 10^{-7}$	0.24	$3.6 \cdot 10^{-6}$	$6.9 \cdot 10^{-7}$
4	0.24	$2.3 \cdot 10^{-6}$	$1.1 \cdot 10^{-7}$	0.23	$3.7 \cdot 10^{-6}$	$2.2 \cdot 10^{-7}$
Substrate	0.63	$1.2 \cdot 10^{-4}$	$5.7 \cdot 10^{-6}$	0.71	$2.7 \cdot 10^{-4}$	$1.2 \cdot 10^{-5}$

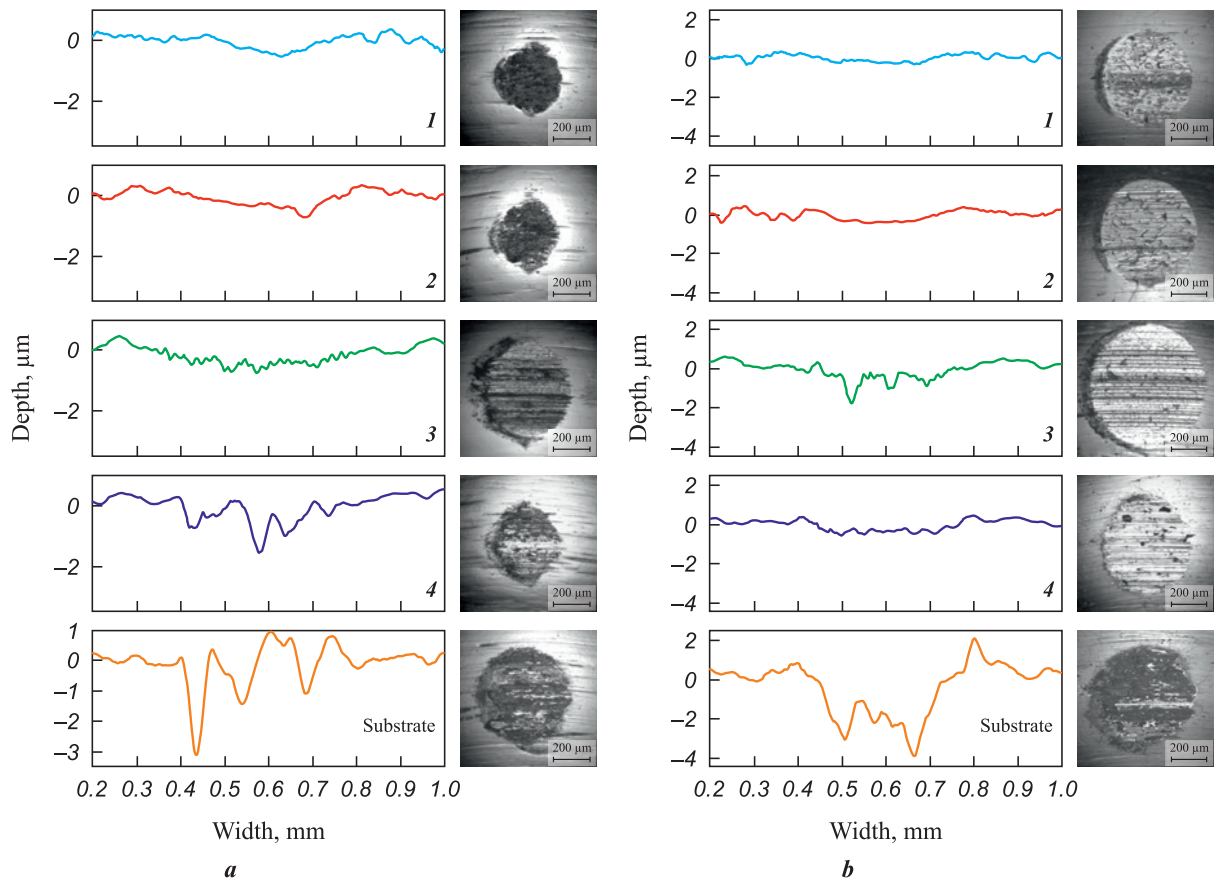


Fig. 7. Wear track profiles and micrographs counter body wear zones from tests using SKH51 (a) and SKD11 (b) balls

Рис. 7. Профили дорожек износа и микрофотографии зон износа контртел при испытаниях шариками Р6М5 (a) и Х12МФ (b)

of  $1.2 \cdot 10^{-4} \text{ mm}^3/(\text{N} \cdot \text{m})$  (SKH51 counter body) and  $2.7 \cdot 10^{-4} \text{ mm}^3/(\text{N} \cdot \text{m})$  (SKD11 counter body) (Table 6).

Coatings 1 and 2 exhibited the lowest specific wear rates, with  $V_{\text{coat}} = (1.3 \div 1.4) \cdot 10^{-6} \text{ mm}^3/(\text{N} \cdot \text{m})$  and  $(1.1 \div 1.2) \cdot 10^{-6} \text{ mm}^3/(\text{N} \cdot \text{m})$  in tribological pairs with SKH51 and SKD11, respectively. Coatings 3 and 4 showed higher wear rates when paired with SKH51 counterbodies –  $V_{\text{coat}} = 5.0 \cdot 10^{-6}$  and  $2.3 \cdot 10^{-6} \text{ mm}^3/(\text{N} \cdot \text{m})$  – and comparable  $V_{\text{coat}} = (3.6 \div 3.7) \cdot 10^{-6} \text{ mm}^3/(\text{N} \cdot \text{m})$  when tested against SKD11. The reduced wear resistance of the coatings upon bronze addition may be attributed to the fact that copper, the primary component, is a soft phase more prone to abrasion [54]. Microscopic analysis of wear scars on the counterbodies (Fig. 7) revealed that the greatest wear occurred during contact with the uncoated substrate (Table 6). The minimum counterbody wear ( $V_{\text{ball}}$ ) for the SKH51 ball was observed with coatings 1 and 2, while for the SKD11 ball it was recorded with coatings 1 and 4.

Thus, deposition of Ti–Cr–Ni–C–(N) and Ti–Cr–Ni–Cu–Sn–P–C–(N) coatings led to a 2.5–4.2-fold reduction in the friction coefficient of the steel sub-

strate and a two-order-of-magnitude decrease in specific wear. Notably, coating 1 demonstrated the most favorable combination of low friction coefficient and high wear resistance in tests with both SKH51 and SKD11 balls, while also exhibiting the highest crack resistance and adhesion strength.

## Conclusion

Ti–Cr–Ni–C–(N) and Ti–Cr–Ni–Cu–Sn–P–C–(N) coatings were deposited by magnetron sputtering in Ar and Ar–N<sub>2</sub> atmospheres using SHS-derived targets. The coatings exhibited dense, defect-free, and uniform microstructures. The primary structural components in all coatings were FCC phases *c*-TiC(N) and *c*-(Ni,Cr). For the Ti–Cr–Ni–C and Ti–Cr–Ni–C–N coatings, the crystallite sizes of the *c*-TiC(N) and *c*-(Ni,Cr) phases were similar, ranging from 34–36 nm and 22–23 nm, respectively. The introduction of bronze resulted in the formation of an amorphous Cu-based phase and a reduction in the crystallite size of *c*-TiC by 12–15 % and *c*-(Ni,Cr) by 32–64 %. All coatings demonstrated hardness values in the range of 18–21 GPa and elastic moduli

between 220 and 235 GPa. The Ti–Cr–Ni–C coating exhibited the best combination of crack resistance, adhesion strength, lowest coefficient of friction (0.17–0.18), and high wear resistance ( $1.4 \cdot 10^{-6}$  and  $1.2 \cdot 10^{-6}$  mm<sup>3</sup>/(N·m) when paired with SKH51 and SKD11 counterbodies, respectively). Deposition of Ti–Cr–Ni–Cu–Sn–P–C–N coatings contributed to a 2.5–4.2-fold reduction in the substrate's coefficient of friction and a two-order-of-magnitude decrease in specific wear.

## References / Список литературы

- Larhlimi H., Ghailane A., Makha M., Alami J. Magnetron sputtered titanium carbide-based coatings: A review of science and technology. *Vacuum*. 2022;197:110853. <https://doi.org/10.1016/j.vacuum.2021.110853>
- He J., He Z., Qin Y., Zhao H., Bi Y. A review of TiCN coating prepared by reaction plasma spraying. *Journal of Thermal Spray Technology*. 2022;31(8):2280–2299. <https://doi.org/10.1007/s11666-022-01454-5>
- Aramian A., Sadeghian Z., Narimani M., Razavi N., Ber-to F. A review on the microstructure and properties of TiC and Ti(C,N) based cermets. *International Journal of Refractory Metals and Hard Materials*. 2023;115:106320. <https://doi.org/10.1016/j.ijrmhm.2023.106320>
- Martínez-Martínez D., López-Cartes C., Justo A., Fernández A., Sánchez-López J.C. Self-lubricating Ti–C–N nanocomposite coatings prepared by double magnetron sputtering. *Solid State Sciences*. 2009;11(2):660–670. <https://doi.org/10.1016/j.solidstatesciences.2008.09.004>
- Chen Q., Liang D., Zhang E., Yang L., Zhou Q., Huang B., Han S. Influence of C<sub>2</sub>H<sub>2</sub>/N<sub>2</sub> flow ratio on the microstructure, mechanical properties, and electrochemical behavior of TiCN composite coatings. *Vacuum*. 2023;216:112349. <https://doi.org/10.1016/j.vacuum.2023.112349>
- Karlsson L., Hultman L., Johansson M.P., Sundgren J.-E., Ljungcrantz H. Growth, microstructure, and mechanical properties of arc evaporated TiC<sub>x</sub>N<sub>1-x</sub> (0 ≤ x ≤ 1) films. *Surface and Coatings Technology*. 2000;126(1):1–14. [https://doi.org/10.1016/S0257-8972\(00\)00518-1](https://doi.org/10.1016/S0257-8972(00)00518-1)
- Podhurska V., Kuprin O., Prikhna T., Ostash O., Pohl D., Karpets M., Sverdun V., Serbeniuk T., Chepil R., Potapov P., Ponomarov S. Development of oxidation-resistant and electrically conductive coating of Ti–Al–C system for the lightweight interconnects of solid oxide fuel cells. *Heliyon*. 2024;10(1):e23275. <https://doi.org/10.1016/j.heliyon.2023.e23275>
- Zhang X., Qiu Y., Tan Z., Lin J., Xu A., Zeng Y., Moore J.J., Jiang J. Effect of Al content on structure and properties of TiAlCN coatings prepared by magnetron sputtering. *Journal of Alloys and Compounds*. 2014;617:81–85. <https://doi.org/10.1016/j.jallcom.2014.08.009>
- Testa V., Morelli S., Bolelli G., Bosi F., Puddu P., Colella A., Manfredini T., Lusvardi L. Corrosion and wear performances of alternative TiC-based thermal spray coatings. *Surface and Coatings Technology*. 2022;438:128400. <https://doi.org/10.1016/j.surfcoat.2022.128400>
- Zhang S., Fu Y., Du H., Zeng X.T., Liu Y.C. Magnetron sputtering of nanocomposite (Ti,Cr)CN/DLC coatings. *Surface and Coatings Technology*. 2003;162(1):42–48. [https://doi.org/10.1016/S0257-8972\(02\)00561-3](https://doi.org/10.1016/S0257-8972(02)00561-3)
- Kiryukhantsev-Korneev Ph.V., Sheveyko A.N., Shvindina N.V., Levashov E.A., Shtansky D.V. Comparative study of Ti–C–Ni–Al, Ti–C–Ni–Fe, and Ti–C–Ni–Al/Ti–C–Ni–Fe coatings produced by magnetron sputtering, electro-spark deposition, and a combined two-step process. *Ceramics International*. 2018;44(6):7637–7646. <https://doi.org/10.1016/j.ceramint.2018.01.091>
- Bondarev A.V., Kiryukhantsev-Korneev Ph.V., Levashov E.A., Shtansky D.V. Tribological behavior and self-healing functionality of TiNbCN–Ag coatings in wide temperature range. *Applied Surface Science*. 2017;396:110–120. <https://doi.org/10.1016/j.apsusc.2016.10.188>
- Ghorbani M., Mazaheri M., Afshar A. Wear and friction characteristics of electrodeposited graphite–bronze composite coatings. *Surface and Coatings Technology*. 2005;190(1):32–38. <https://doi.org/10.1016/j.surfcoat.2004.04.092>
- Ghorbani M., Mazaheri M., Khangholi K., Kharazi Y. Electrodeposition of graphite-brass composite coatings and characterization of the tribological properties. *Surface and Coatings Technology*. 2001;148(1):71–76. [https://doi.org/10.1016/S0257-8972\(01\)01322-6](https://doi.org/10.1016/S0257-8972(01)01322-6)
- Musil J., Louda M., Soukup Z., Kubásek M. Relationship between mechanical properties and coefficient of friction of sputtered a-C/Cu composite thin films. *Diamond and Related Materials*. 2008;17(11):1905–1911. <https://doi.org/10.1016/j.diamond.2008.04.009>
- Shao F., Zhao H., Ni J., Zhuang Y., Sheng J., Yang J., Zhong X., Tao S. Corrosion behavior and mechanical properties of plasma sprayed Al<sub>2</sub>O<sub>3</sub>-aluminum bronze and Ca<sub>2</sub>SiO<sub>4</sub>-aluminum bronze coatings. *Materials Chemistry and Physics*. 2024;311:128579. <https://doi.org/10.1016/j.matchemphys.2023.128579>
- Musil J. Hard and superhard nanocomposite coatings. *Surface and Coatings Technology*. 2000;125(1–3):322–330. [https://doi.org/10.1016/S0257-8972\(99\)00586-1](https://doi.org/10.1016/S0257-8972(99)00586-1)
- Musil J., Kadlec S., Vyskočil J., Valvoda V. New results in d.c. reactive magnetron deposition of TiN<sub>x</sub> films. *Thin Solid Films*. 1988;167(1–2):107–120. [https://doi.org/10.1016/0040-6090\(88\)90487-7](https://doi.org/10.1016/0040-6090(88)90487-7)
- Soldán J., Musil J. Structure and mechanical properties of DC magnetron sputtered TiC/Cu film. *Vacuum*. 2006;81(4):531–538. <https://doi.org/10.1016/j.vacuum.2006.07.013>
- Sun H., Billard A., Luo H., Zheng W.-T., Zheng X.-L., Dai M.-J., Lin S.-S., Shi Q., Sanchette F. Influence of carbon content on the mechanical properties of TiCN–Cu nanocomposite coatings prepared by multi-arc ion plating. *Vacuum*. 2021;187:110139. <https://doi.org/10.1016/j.vacuum.2021.110139>
- Ghahabi E., Shajari Y., Razavi M., Mobasherpour I., Tayebi Fard S.A. Effect of iron content on the wear behavior and adhesion strength of TiC–Fe nanocomposite coatings on low carbon steel produced by air plasma spray. *Ceramics International*. 2020;46(3):2670–2676. <https://doi.org/10.1016/j.ceramint.2019.09.255>
- Das A.K., Kumar R. Investigation on wear behaviour of TiC/Co/Y<sub>2</sub>O<sub>3</sub> metal matrix composite coating developed on AZ91D Mg alloy by plasma transferred arc clad-

- ding process. *Materials Letters*. 2024;355:135457. <https://doi.org/10.1016/j.matlet.2023.135457>
23. Sun L., Wang X., Cao Y., Wang Y., Ma Q., Wu H., Hua K., Wang H. High-temperature fretting wear behavior and microstructure stability of a laser-cladding Ti–Al–C–N composite coating mediated by variable cycle conditions. *Tribology International*. 2025;201:110224. <https://doi.org/10.1016/j.triboint.2024.110224>
  24. Gvetadze R., Arutyunov S., Kryuchkov S., Antipov M., Bazhin, P., Mustafaev M., Deshev A., Tsarev V., Andreev M., Katkov I., Agasieva S., Avdeeva V. Cermet coatings obtained by electric spark alloying to increase service life of dental instruments. *Ceramics International*. 2024;50(24, Part A):52613–52621. <https://doi.org/10.1016/j.ceramint.2024.10.112>
  25. Kuptsov K.A., Sheveyko A.N., Sidorenko D.A., Shtansky D.V. Electro-spark deposition in vacuum using graphite electrode at different electrode polarities: Peculiarities of microstructure, electrochemical and tribological properties. *Applied Surface Science*. 2021;566:150722. <https://doi.org/10.1016/j.apsusc.2021.150722>
  26. Gassner M., Schalk N., Tkadletz M., Czettel C., Mitterer C. Thermal crack network on CVD TiCN/ $\alpha$ -Al<sub>2</sub>O<sub>3</sub> coated cemented carbide cutting tools. *International Journal of Refractory Metals and Hard Materials*. 2019;81:1–6. <https://doi.org/10.1016/j.ijrmhm.2019.02.006>
  27. Kiryukhantsev-Korneev P., Sytchenko A., Sheveyko A., Moskovskikh D., Vorotylo S. Two-layer nanocomposite TiC-based coatings produced by a combination of pulsed cathodic arc evaporation and vacuum electro-spark alloying. *Materials*. 2020;13(3):547. <https://doi.org/10.3390/ma13030547>
  28. Sajjadi S.A., Saba F., Ghadirzadeh A., Di Fonzo F. Synthesis of TiC coating on Ti substrate using pulsed laser deposition and mechanical milling techniques along with statistical modeling of the process by response surface methodology. *Powder Technology*. 2017;305:704–713. <https://doi.org/10.1016/j.powtec.2016.10.054>
  29. Kelly P.J., Arnell R.D. Magnetron sputtering: A review of recent developments and applications. *Vacuum*. 2000;56(3):159–172. [https://doi.org/10.1016/S0042-207X\(99\)00189-X](https://doi.org/10.1016/S0042-207X(99)00189-X)
  30. Shtansky D.V., Gloushankova N.A., Sheveiko A.N., Kiryukhantsev-Korneev Ph.V., Bashkova I.A., Mavrin B.N., Ignatov S.G., Filippovich S.Yu., Rojas C. Si-doped multifunctional bioactive nanostructured films. *Surface and Coatings Technology*. 2010;205(3):728–739. <https://doi.org/10.1016/j.surfcoat.2010.07.063>
  31. Shtansky D.V., Kiryukhantsev-Korneev Ph.V., Sheveyko A.N., Kutyrev A.E., Levashov E.A. Hard tribological Ti–Cr–B–N coatings with enhanced thermal stability, corrosion- and oxidation resistance. *Surface and Coatings Technology*. 2007;202(4–7):861–865. <https://doi.org/10.1016/j.surfcoat.2007.05.064>
  32. Kiryukhantsev-Korneev Ph.V., Chertova A.D., Chudarin F.I., Patsera E.I., Levashov E.A. The structure and properties of high-entropy (MoTaNbZrHf)–Si–B coatings deposited by DCMS and HIPIMS methods using the multilayer target. *Surface and Coatings Technology*. 2024;484:130797. <https://doi.org/10.1016/j.surfcoat.2024.130797>
  33. Levashov E.A., Mukasyan A.S., Rogachev A.S., Shtansky D.V. Self-propagating high-temperature synthesis: An overview of recent developments. *International Materials Reviews*. 2017;62(4):203–239. <https://doi.org/10.1080/09506608.2016.1243291>
  34. Levashov E.A., Malochkin O.V., Kudryashov A.E., Glukhov S.A., Sviridova T.A., Gammel F., Zukhentrunck R. On features of the effect of nanocrystalline powders on burning processes and forming composition, structure, and properties of STIM-3B alloy. *Izvestiya. Non-Ferrous Metallurgy*. 2001;(1):53–59. (In Russ.).  
Левашов Е.А., Малочкин О.В., Кудряшов А.Е., Глухов С.А., Свиридова Т.А., Гаммел Ф., Зухентрунк Р. Об особенностях влияния нанокристаллических порошков на процессы горения и формирование состава, структуры и свойств сплава СТИМ-3Б. *Известия вузов. Цветная металлургия*. 2001;(1):53–59.
  35. Shiryayev A.A. Thermodynamics of SHS: Modern approach. *International Journal of Self-Propagating High-Temperature Synthesis*. 1995;4(4):351–362.
  36. Kiryukhantsev-Korneev Ph.V., Sytchenko A.D., Sviridova T.A., Sidorenko D.A., Andreev N.V., Klechkovskaya V.V., Polčak J., Levashov E.A. Effects of doping with Zr and Hf on the structure and properties of Mo–Si–B coatings obtained by magnetron sputtering of composite targets. *Surface and Coatings Technology*. 2022;442:128141. <https://doi.org/10.1016/j.surfcoat.2022.128141>
  37. Kiryukhantsev-Korneev F.V. Possibilities of glow discharge optical emission spectroscopy in the investigation of coatings. *Russian Journal of Non-Ferrous Metals*. 2014; 55:494–504. <https://doi.org/10.3103/S1067821214050126>  
Кирюханцев-Корнеев Ф.В. Возможности метода оптической эмиссионной спектроскопии тлеющего разряда GDOES при исследовании покрытий. *Известия вузов. Порошковая металлургия и функциональные покрытия*. 2013;(2):60–70. <https://doi.org/10.17073/1997-308X-2013-2-60-70>
  38. Zueva L.V., Gusev A.I. Effect of nonstoichiometry and ordering on the period of the basis structure of cubic titanium carbide. *Physics of the Solid State*. 1999;41(7):1032–1038. <https://doi.org/10.1134/1.1130931>  
Зуева Л.В., Гусев А.И. Влияние нестехиометрии и упорядочения на период базисной структуры кубического карбида титана. *Физика твердого тела*. 1999;41(7):1134–1141.
  39. Brydson R., Hondow N. Electron energy loss spectroscopy and energy dispersive X-ray analysis. In: *Aberation-corrected analytical transmission electron microscopy*. Eds. S. Brooks, R. Brydson. Wiley, 2011. P. 163–210. <https://doi.org/10.1002/9781119978848.ch7>
  40. Davis J.R. Copper and copper alloys. ASM International, 2001. 652 p.
  41. Semenov A.P., Semenova I.A., Tsyrenov D.B.-D., Nikolaev E.O. Physical sputtering of a copper anode of a planar magnetron by a beam of accelerated argon ions with an energy of 1–10 keV. *Instruments and Experimental Techniques*. 2021;(64):539–541. <https://doi.org/10.1134/S0020441221040242>  
Семенов А.П., Семенова И.А., Цыренов Д.Б.-Д., Николаев Э.О. Физическое распыление медного анода пла-

- нарного магнетрона пучком ускоренных ионов аргона энергией 1–10 кэВ. *Приборы и техника эксперимента*. 2021;(4):44–46.  
<https://doi.org/10.31857/S0032816221040261>
42. Mhadhbi M., Driss M. Titanium carbide: synthesis, properties and applications. *Journal of Brilliant Engineering*. 2021;2:1–11.  
<https://doi.org/10.36937/ben.2021.002.001>
  43. Kovtun Yu.V., Kuprin A.S., Podhurska V.Ya. Sputtering yields of TiC and MAX phase Ti<sub>2</sub>AlC using Ne, Ar, Xe ions. *Nuclear Instruments and Methods in Physics Research. Section B: Beam Interactions with Materials and Atoms*. 2024;554:165433.  
<https://doi.org/10.1016/j.nimb.2024.165433>
  44. Kiryukhantsev-Korneev Ph.V., Sytchenko A.D., Kozlova N.S., Zabelina E.V., Sidorenko D.A., Levashov E.A., Feng P. Effect of nitrogen on the structure and properties of Zr–Si–B–N coatings deposited by magnetron sputtering. *Surface and Coatings Technology*. 2023;474:130042.  
<https://doi.org/10.1016/j.surfcoat.2023.130042>
  45. Hahn R., Tymoszuk A., Wojcik T., Kimbauer A., Kozák T., Čapek J., Sauer M., Foelske A., Hunold O., Polcik P., Mayrhofer P.H., Riedl H. Phase formation and mechanical properties of reactively and non-reactively sputtered Ti–B–N hard coatings. *Surface and Coatings Technology*. 2021;420:127327.  
<https://doi.org/10.1016/j.surfcoat.2021.127327>
  46. Lauridsen J., Nedfors N., Jansson U., Jensen J., Eklund P., Hultman L. Ti–B–C nanocomposite coatings deposited by magnetron sputtering. *Applied Surface Science*. 2012; 258(24):9907–9912.  
<https://doi.org/10.1016/j.apsusc.2012.06.049>
  47. Larhlmi H., Ghailane A., Makha M., Alami J. Magnetron sputtered titanium carbide-based coatings: A review of science and technology. *Vacuum*. 2022;197:110853.  
<https://doi.org/10.1016/j.vacuum.2021.110853>
  48. Sytchenko A.D., Kozlova N.S., Zabelina E.V., Loginov P.A., Levashov E.A., Kiryukhantsev-Korneev Ph.V. The effect of the Ar/N<sub>2</sub> gas ratio on the structure and properties of Ta–Si–N coatings produced by magnetron sputtering of a TaSi<sub>2</sub> target. *Surface and Interfaces*. 2023;37:102654.  
<https://doi.org/10.1016/j.surf.2023.102654>
  49. Beake B.D. The influence of the H/E ratio on wear resistance of coating systems – insights from small-scale testing. *Surface and Coatings Technology*. 2022;442:128272.  
<https://doi.org/10.1016/j.surfcoat.2022.128272>
  50. Leyland A., Matthews A. On the significance of the H/E ratio in wear control: A nanocomposite coating approach to optimised tribological behaviour. *Wear*. 2000;246:1–11.  
[https://doi.org/10.1016/S0043-1648\(00\)00488-9](https://doi.org/10.1016/S0043-1648(00)00488-9)
  51. Musil J., Hromadka M., Novak P. Effect of nitrogen on tribological properties of amorphous carbon films alloyed with titanium. *Surface and Coatings Technology*. 2011;205(S2):S84–S88.  
<https://doi.org/10.1016/j.surfcoat.2010.12.048>
  52. Zhao H., Guo F., Zhu L., He J., Yin F. The effect of Cu addition on the crystallization behavior and tribological properties of reactive plasma sprayed TiCN–Cu coatings. *Ceramics International*. 2020;46(6):8344–8351.  
<https://doi.org/10.1016/j.ceramint.2019.12.066>
  53. Heo S.B., Kim W.-R., Kim J.H., Choe S., Kim D.W., Lim J.-H., Park I.-W. Effects of copper content on the microstructural, mechanical and tribological properties of TiAlSiN–Cu superhard nanocomposite coatings. *Coatings*. 2022;12(12):1995.  
<https://doi.org/10.3390/coatings12121995>
  54. Li F., Dai W., Wu Z., Xu Y., Wang J., Wang Q. Effect of Cu content on the mechanical and tribological properties of MoN–Cu coatings deposited by HiPIMS. *Surface and Coatings Technology*. 2025;497:131769.  
<https://doi.org/10.1016/j.surfcoat.2025.131769>

### Information about the Authors



### Сведения об авторах

**Philipp V. Kiryukhantsev-Korneev** – Dr. Sci. (Eng.), Professor of the Department of Powder Metallurgy and Functional Coatings (PM&F) of National University of Science and Technology “MISIS” (NUST MISIS), Head of the Laboratory “In situ Diagnostics of Structural Transformations” of Scientific-Educational Center of Self-Propagating High-Temperature Synthesis MISIS-ISMAN (SHS-Center)

 **ORCID:** 0000-0003-1635-4746

 **E-mail:** kiruhancev-korneev@yandex.ru

**Alina D. Chertova** – Cand. Sci. (Eng.), Research Scientist of SHS-Center MISIS-ISMAN

 **ORCID:** 0000-0002-8668-5877

 **E-mail:** alina-sytchenko@yandex.ru

**Yuri S. Pogozhev** – Cand. Sci. (Eng.), Senior Research Scientist of SHS-Center MISIS-ISMAN

 **ORCID:** 0000-0001-6733-7212

 **E-mail:** yspogozhev@mail.ru

**Evgeniy A. Levashov** – Dr. Sci. (Eng.), Prof., Corresponding Member of the RAS, Head of the Department of PM&F of NUST MISIS, Director of SHS-Center MISIS-ISMAN

 **ORCID:** 0000-0002-0623-0013

 **E-mail:** levashov@shs.misis.ru

**Филипп Владимирович Кирюханцев-Корнеев** – д.т.н., профессор кафедры порошковой металлургии и функциональных покрытий (ПМиФП) Национального исследовательского технологического университета «МИСИС» (НИТУ МИСИС), зав. лабораторией «In situ диагностика структурных превращений» Научно-учебного центра (НУЦ) СВС МИСИС-ИСМАН

 **ORCID:** 0000-0003-1635-4746

 **E-mail:** kiruhancev-korneev@yandex.ru

**Алина Дмитриевна Чертова** – к.т.н, науч. сотрудник НУЦ СВС МИСИС-ИСМАН

 **ORCID:** 0000-0002-8668-5877

 **E-mail:** alina-sytchenko@yandex.ru

**Юрий Сергеевич Погужев** – к.т.н, ст. науч. сотрудник НУЦ СВС МИСИС-ИСМАН

 **ORCID:** 0000-0001-6733-7212

 **E-mail:** yspogozhev@mail.ru

**Евгений Александрович Левашов** – д.т.н., проф., чл.-корр. РАН, зав. кафедрой ПМиФП, НИТУ МИСИС, директор НУЦ СВС МИСИС-ИСМАН

 **ORCID:** 0000-0002-0623-0013

 **E-mail:** levashov@shs.misis.ru

**Contribution of the Authors****Вклад авторов**

**Ph. V. Kiryukhantsev-Korneev** – performed magnetron sputtering deposition of the coatings, prepared the manuscript, and discussed the results.

**A. D. Chertova** – conducted structural analysis and tribological tests, analyzed the data, and contributed to manuscript writing.

**Yu. S. Pogožhev** – consolidated and analyzed the structure of the cathode targets.

**E. A. Levashov** – defined the research objectives, supervised the study, revised the manuscript, and formulated the conclusions.

**Ф. В. Кирюханцев-Корнеев** – нанесение покрытий методом магнетронного распыления, подготовка текста статьи, обсуждение результатов.

**А. Д. Чертова** – проведение структурных исследований и трибологических испытаний, анализ результатов исследований, подготовка текста статьи.

**Ю. С. Погожев** – консолидация и проведение структурных исследований катодов-мишеней.

**Е. А. Левашов** – постановка цели, общее руководство, корректировка текста статьи, формулировка выводов.

Received 31.03.2025

Revised 01.04.2025

Accepted 04.04.2025

Статья поступила 31.03.2025 г.

Доработана 01.04.2025 г.

Принята к публикации 04.04.2025 г.



**Зарегистрирован Федеральной службой по надзору  
в сфере связи, информационных технологий  
и массовых коммуникаций.**

**Свидетельство о регистрации ПИ № ФС77-79230**

**Журнал распространяется агентством «Урал-Пресс»  
Подписной индекс: 80752 (печатная версия)  
05108 (электронная версия)**

